UCGE Reports
Number 20210

Department of Geomatics Engineering

Data Assimilation for 4-D Wet Refractivity Modelling in a Regional GPS Network

(URL: http://www.geomatics.ucalgary.ca/links/GradTheses.html)

by

Victoria Anne Hoyle

January 2005

UNIVERSITY OF CALGARY

Data Assimilation for 4-D Wet Refractivity Modelling in a Regional GPS Network

by

Victoria Anne Hoyle

A THESIS

SUBMITTED TO THE FACULTY OF GRADUATE STUDIES

IN PARTIAL FULFILMENT OF THE REQUIREMENTS FOR THE

DEGREE OF MASTER OF SCIENCE

DEPARTMENT OF GEOMATICS ENGINEERING

CALGARY, ALBERTA

JANUARY, 2005

ABSTRACT

One source of error for GPS signals received on the Earth is due to the delay caused by propagation through the troposphere. If a receiver's coordinates are known and surface pressure measurements are available, the positioning problem can be inverted such that the wet delay in the signal can be used to derive water vapour content in the atmosphere through a tomographic, 4-D model.

Local radiosonde observations, monthly-averaged climate data and GPS occultation-derived wet refractivity measurements were assimilated into a tomography model which originally used ground-based GPS data over southern Alberta. Improvements were made to the estimation of vertical profiles of water vapour, and improvements in the integrated domain were on the order of ~0.5 cm for the assimilation of radiosonde data. The best results were obtained by assimilating radiosonde observations. Occultation measurement assimilation resulted in improvements in the integrated domain of up to 0.5 cm.

ACKNOWLEDGMENTS

I wish to express my deep gratitude to my supervisor Dr. Susan Skone, for her support and advice during my time as her student. Thank you for being a good mentor and role model. What you have taught me about professionalism, hard work and integrity through your own example has been just as valuable as any technical knowledge that I have gained during this degree. I have always felt a great sense of pride when I tell people I'm your student. Thank you in particular for the time you put into revising this thesis.

I would like to thank my parents Alice and Derek Hoyle for their love and support for the past 28 years. This could not have been possible without you. Thank you for giving me the freedom and backing during my upbringing to let me think anything is possible.

Thank you Dr. Gérard Lachapelle, for giving me the opportunity to be your research assistant; you taught me that pushing perceived boundaries makes way for great achievements. Thank you also to Dr. Elizabeth Cannon for her support throughout my time at the University of Calgary.

Special thanks to Craig Smith, Geoff Strong and Terry Krauss for their tireless efforts to make me more meteorologically savvy. I greatly appreciate all the e-mails you gave me when I had a question, or needed data. Also thanked are Seth Gutman, Teresa Van Hove, John Braun and Jens Wickert for their advice in processing and the time they spent assisting me.

My colleagues of the past, thank you so much for your advice, and encouragement: Rakesh Nayak, Glenn MacGougan, Paulo Alves, Kyle O'Keefe, Luiz Fortes and Mark Petovello are of particular note. To the Skone-group students that I have worked with of past and present: Mahmoud El-Gizawy, Sudhir Shrestha, Yongjin Moon, Ruben Yousuf and Lance de Groot, thank you for making work a great place to come to everyday.

To my long-time friends Carol Paskall, Jane Cameron, Kristi Epp, Tara Pohl and Erin Royal, thank you for having the patience to be a friend to a professional student all these years.

Special thanks are given to Natalya Nicholson as a colleague and friend. To find someone whom you work well with is lucky, but to find someone with whom you also share a close bond of friendship with is a rare treasure.

A large debt of gratitude is owed to the International GPS Service for GPS data and orbits used while processing ground-based SAN data. The GFZ is noted for their refined processing of GPS occultation data. Weather Modification Inc. and The Alberta Severe Weather Management Society are thanked for the use of their radar data. MSC is also noted for the processing of radiosonde data and the GEM model data used in this work. Thank you to those graduate students who have helped in the upkeep of the SAN.

Thanks are given to Rinske Van Gosliga and Sudhir Shrestha for their assistance in Bernese processing.

I also wish to thank teachers who made a real difference during my education: Mr. Elliot, Mr. Rusinak, Mr. McNamee, Dr. Rogers and Dr. El-Sheimy. Thank you for the inspiration.

TABLE OF CONTENTS

LIST OF TABLES

LIST OF FIGURES

LIST OF SYMBOLS

φ	phase of EM signal at reception
λ	wavelength of EM signal
Φ	GPS carrier phase observable
N	ambiguity
Δ	difference of GPS observations between receivers
∇	difference of GPS observations between satellites
ρ *or* G	geometric range between satellite and receiver
$d\rho$	orbital errors in the GPS observation equation
d_{ion}	ionospheric delay in the GPS observation equation
d_{trop}	tropospheric (neutral atmospheric) delay in the GPS observation equation
$e_{\Delta\nabla mp}$	double difference multipath error
$e_{\Delta\nabla noise}$	double difference receiver noise error
f	frequency of an EM signal
n	index of refraction
N	refractivity
Δs	EM signal excess path length
S	curved ray path from satellite to receiver due to error source
N_T	total refractivity
ds	path of signal from satellite to receiver
N_H	hydrostatic refractivity

N_W	wet refractivity
P	pressure
T	temperature
e	partial pressure of water vapour
d_{tot}	total GPS tropospheric delay
$m_h(\varepsilon)$	hydrostatic mapping function
$m_w(\varepsilon)$	wet mapping function
d_{hz}	zenith hydrostatic delay
P_S	surface pressure
H_d^e	dry equivalent height – the height above a station at which the dry refractivity is zero
T_S	surface temperature
N_{WS}	surface wet refractivity
H_w^e	wet equivalent height – the height above a station at which the wet refractivity is zero
e_S	surface partial pressure of water vapour
$a_{0i}, \ldots, a_{5i}$	expansion coefficients for layer i in the tomography model
$\frac{1}{b}$	correlation time
$q(t)$	process noise
σ/σ^2	standard deviation/variance of a measurement
$\mathbf{x}$	vector of quantities to be estimated

Φ	transition matrix
K	Kalman filter gain matrix
H	design matrix
R	covariance information for observations
P	covariance information for estimated parameters
z	vector of observations
es	saturation pressure of water vapour
T_0	the adopted phase day of year 28

LIST OF ABBREVIATIONS

CHAMP	CHAllenging Minisatellite Payload
COSMIC	Constellation Observing System for Meteorology, Ionosphere and Climate
DA	Data Assimilation
DOP	Dilution of Precision
GEM model	Global Environmental Multi-scale model
GFZ	GeoForschungsZentrum in Potsdam, Germany
GNSS	Global Navigation Satellite Systems
GPS	Global Positioning System
IF	Ionosphere-Free
LEO	Low Earth Orbiter
masl	metres above sea level
MET3A	Paroscientific Meteorological Measurement System
MP	Microwave Profiler
MSC	Meteorological Service of Canada
MWP	MicroWave Profiler
NRCan	Natural Resources Canada
N_W	Wet refractivity
NWP	Numerical Weather Prediction
PRN	PseudoRandom Noise
PSAS	Portland State Aerospace Society

PWV	Precipitable Water Vapour
RMS	Root Mean Squared
Rx/rx	Receiver
SAC-C	Satelite de Aplicanciones Cientificas C
SAN	Southern Alberta Network
SHD	Slant Hydrostatic Delay
Sv/sv	Space Vehicle or satellite
SWD	Slant Wet Delay
TEC	Total Electron Content (electrons / m^2)
UTC	Universal Time Coordinated
WMI	Weather Modification Incorporated
WVR	Water Vapour Radiometer
ZWD	Zenith Wet Delay

CHAPTER 1

INTRODUCTION

1.1 Background

The Global Positioning System (GPS) was originally conceived and implemented by the United States Department of Defense for military positioning and navigation purposes. The first satellite was launched in 1978 [*Parkinson and Spilker*, 1996] and by 1996 the system was at full operational capability [*Kaplan*, 1996]. In 2003 equipment sales for GPS were close to $3.5 billion worldwide, and it is expected that number will grow to $10 billion after 2010 [*Enge*, 2004]. GPS is a system of 27 satellites that orbit at approximately 20000 km above the surface of the Earth. The satellites are launched into six orbital planes, 60 degrees apart at an inclination of 55 degrees with respect to the equator. The constellation of GPS satellites provides all-weather, world-wide, and continuous measurements, providing line-of-sights to the satellites are available. These characteristics make GPS observations advantageous for positioning and navigation, and remote sensing applications.

As GPS signals traverse the atmosphere, one source of error is due to the signal's propagation through the troposphere. The bulk of GPS users are interested in positioning and navigation, and efforts continue to be taken to estimate the delay in the GPS signal due to the troposphere in order to provide more accurate positioning solutions (i.e. *Alves et al*. [2004]). However, the tropospheric error experienced by GPS started to be seen as a signal rather than a nuisance parameter beginning with a key paper by *Bevis et al*. [1992], due to the fact that part of the tropospheric error is caused by water vapour and it is retrievable from the total tropospheric error. With this work, GPS started to become a viable tool for remotely sensing atmospheric water vapour.

Weather and climate have become important topics in recent years, as more interest has been focused on examining the human impact on the Earth's energy balance. A recent report published by the United Nations' Intergovernmental Panel on Climate Change (IPCC) projects that there is a propensity for extreme weather in the future [*McCarthy*, 2001]. With weather systems becoming more severe, accurate weather prediction becomes a key tool in mitigating the loss of life. Along with weather, the apparent heating trend in the world's climate is a widely studied and fervently debated topic. An overall warming in the global climate has undeniable impacts on biodiversity, water resources, land use, and quality of life. Although many will argue whether global warming exists or not, one thing is clear: the human cost of global warming is so staggering that it would be foolish not to research more effective ways of monitoring changes in the atmosphere of the Earth.

Water is an important part of any weather or climate change study because it has a high latent heat, and thus by tracking water heat movement is tracked as well. The Earth's atmosphere is able to hold more water vapour with increasing temperature and as water vapour absorbs heat, rising temperature and water vapour together act as part of a climate warming feedback loop [*Aguado and Burt*, 2004]. Traditional methods of collecting data on atmospheric water vapour do not offer the spatial and temporal resolution necessary for in-depth studies of weather and climate [*Ware et al*., 2000]. In order to fully understand climate and weather patterns, more comprehensive data sets are needed. GPS is a contender for providing the water vapour knowledge that atmospheric scientists have been seeking due to the large number of measurements that can be made temporally and spatially in all weather conditions, and also due to the fact that GPS sensing of water vapour does not require continual calibration as some sensors do for measurement drifts or biases. Due to the coverage timeliness that GPS water vapour estimates offer, GPS could be used to determine the distribution of water vapour for a region of interest and thus help in the identification of potential severe weather activity [*Jerrett and Nash*, 2001].

Southern Alberta provides a challenging location for water vapour estimation and weather prediction (for the location of the Canadian province of Alberta, see Figure 1.1).

Figure 1.1. The province of Alberta relative to Canada and North America.

Alberta is around the N 50º-52º latitude range, and is not closely located to a major body of water such as an ocean or large lake. This causes the amount of water vapour present to be low, thereby making the tolerance for noise from the observing algorithm and/or instrument to be very strict.

A unique situation also exists in Alberta due to the proximity of the Rocky Mountains which lie along the south-western edge of the province. Warm dry winds, which are commonly called Chinook winds, flow towards the east from the mountains into southern Alberta. There is a great deal of crops and pasture land to the east of the foothills in Alberta which themselves create an air mass that is relatively colder and wetter than the air flowing from the mountains. The moisture in this air is mainly due to evapotranspiration which is a term that describes the release of water vapour into the air from the release of water through vegetation [*Aguado and Burt*, 2004]. The meeting of these two air masses creates the potential for strong storms in Alberta, especially during summer months when vegetation coverage is at a maximum; southern Alberta lies along the track where disturbances frequently travel from the Pacific over the mountains into the prairies [*Strong*, 2003].

Adding to the complication of weather prediction for the Alberta prairies is that there are no operational radiosonde soundings over the Alberta foothills [*Strong and Smith*, 2001].

Currently several groups of researchers derive zenith measurements of water vapour from ground-based GPS, for more accurate GPS positioning and weather forecasting. The National Oceanic and Atmospheric Administration (NOAA) Forecast Systems Laboratory began research in 1994 to determine the benefit of incorporating GPS zenith integrated measurements of water vapour over stations in the United States into weather forecasting models (for more details see *Wolfe and Gutman* [2000]). Recently, NOAA started to include these measurements into their forecast models. Also, work performed by *Reigber et al.* [2002] shows the benefit of using zenith GPS-derived water vapour measurements over a dense network of receivers in Germany for assimilation into forecasting models. In addition, the SuomiNet network of receivers provides real-time estimates of water vapour for a global network of receivers from zenith water vapour measurements, which are mostly concentrated in the United States (for more information, see *Ware et al.* [2000]). Usually an interpolation scheme is used to determine water vapour between receivers when zenith measurements are taken. Integrated measurements of water vapour have been taken with GPS during such extreme weather events as Typhoon Zeb that hit Taiwan in October 1998 [*Liou and Huang*, 2000], and SuomiNet tracked through Hurricane Ivan that hit the United States in 2004 [*Ware*, 2004].

Instead of using zenith measurements of water vapour, some research has focused on exploiting the slant nature of each receiver-satellite measurement for determining a three-dimensional field of water vapour. This kind of three-dimensional field retrieval from integrated measurements is called tomography, and has been utilized most notably in the field of medicine for imaging of the human body (e.g. MRI - magnetic resonance imaging). Once slant wet delay measurements were found to be obtainable along GPS lines-of-sight to satellites, the possibility of using these integrated measurements in a tomographic approach became evident [*Rocken et al.*, 1997]. GPS measurements are

particularly well suited to water vapour tomography since a user normally sees six to twelve satellites at any given time, and these observations traverse through the atmosphere in many different directions. For tomography purposes, the main observation of interest from GPS is the total slant wet delay (SWD) along lines-of-sight to each satellite. With SWDs as input observations, wet refractivity fields can be formed with resolution in the horizontal and vertical domains. GPS water vapour tomography work has been recently undertaken by several groups in order to utilize the spatial information provided by integrated GPS slant measurements [i.e. *Flores et al*., 2000; *Braun and Rocken*, 2003; *Skone and Shrestha*, 2003].

Starting in early 2003, a network of approximately 16 GPS receivers was deployed in southern Alberta by the Department of Geomatics Engineering from the University of Calgary. This network is called the Southern Alberta Network (SAN). The purpose of this network is to test and investigate improved GPS positioning techniques researched by the department, as well as the assessment of the feasibility of retrieving water vapour fields in the southern Alberta region with GPS. The station spacing was kept to ~50 km whenever possible to allow for optimal resolution of water vapour retrievals for both positioning and atmospheric science applications [*MacDonald et al*., 2002]. Campaigns have been run in the summer of 2003 and 2004 during weeks when intense storms in southern Alberta are most likely. These campaigns have been in collaboration with the Meteorological Service of Canada (MSC), and Weather Modification Inc. (WMI), who released radiosondes from various sites within the network. Radiosondes are generally taken to be truth measurements of water vapour in meteorological circles, and give additional vertical information that can be used to strengthen GPS solutions of water vapour, and can also be used for a truth comparison if deployed at locations within GPS-derived vapour fields. Radiosondes are expensive to deploy so are released sparsely in location and time, and the network of launch sites over the oceans is particularly sparse [*Jacob*, 2001].

Profiles of water vapour in a region can also be determined from measurements such as: GPS occultations, water vapour radiometer (WVR) measurements and microwave profiler (MWP) measurements. The Department of Geomatics Engineering owns a water WVR and MWP radiometer which it purchased from Radiometrics Corporation in Boulder, Colorado. Both instruments receive passive information from selected frequencies and use this information to retrieve water vapour measurements. With augmentations to the retrieval algorithm and the regular uploading of GPS satellite ephemerides to the instrument, measurements can be made along lines of sight to visible GPS satellites. These instruments can provide valuable additional information which can be assimilated into ground-based GPS-derived vapour fields. The MWP is particularly useful while operating in profile mode as it can give vertical constraints to the water vapour solution.

1.2 Objectives

Considering the growing number of water vapour profile measurements that will be available in the future, algorithms for including such measurements in ground-based GPS water vapour solutions should be investigated so that these additional measurements can be examined for their ability to strengthen solutions of such water vapour fields. In light of this, the research outlined in this document has objectives which are threefold:

1. Develop data assimilation schemes for several types of observations that can be included into existing tomography software in addition to ground-based GPS measurements.

2. Examine different data assimilation schemes for each measurement so as to determine the best way to include these measurements into the tomography model.

3. Evaluate the gain in accuracy for all data assimilation schemes in terms of the improvement each method offers to the vertical estimation of water vapour over the case with GPS measurements only in the tomographic approach.

1.3 Outline

Chapters 2 and 3 introduce the theoretical background behind the research performed for this thesis. Chapter 2 gives an overview of GPS theory, observables and error sources with emphasis given to the troposphere and its effects on GPS signals, as it is most relevant to this work. GPS occultations are also introduced in this chapter. Chapter 3 discusses the different ways in which the tropospheric delay on GPS signals can be modelled or estimated. Estimation of tropospheric delay with Bernese version 4.2 GPS processing software is discussed in Chapter 3, as well as tomographic estimation of water vapour in a Kalman filter approach. Measurements of the vertical distribution of atmospheric water vapour are also discussed which are later used as constraints in the tomography model. The main mathematics and algorithms of this research are given in Chapter 3.

Chapter 4 gives a description of the data sets utilized for this research. The Southern Alberta Network of GPS receivers are introduced as well as the A-GAME data collection campaign for the summer of 2003. Chapter 5 gives an overview of the data assimilation techniques utilized in this research. The mathematical changes to the existing tomographic adjustment are discussed for each data type assimilated. In Chapter 6, results are shown for a GPS data set including quiet and storm days. This data set is augmented with additional sources of vertical water vapour distribution measurements, namely radiosonde observations and GPS occultations. Single radiosonde observations and a climatological model derived from monthly radiosonde observations are derived for their use as observational constraints. Occultation measurements, along with Global Environmental Multi-scale (GEM) model data which was used in combination with the occultation data are both described as well. The truth data set consisting of radiosondes

which were not included as observations in the tomographic adjustment is discussed in this chapter. Results from the tomographic retrieval of water vapour using different vertical constraints, and comparisons of the accuracies gained from these different approaches are presented in Chapter 6.

Conclusions made from the results presented in Chapter 6 are discussed in Chapter 7, as well as recommendations for future work in this area.

CHAPTER 2

GPS THEORY

2.1 The Global Positioning System (GPS)

GPS satellites transmit radio frequency signals at 1575.42 (L1) and 1227.60 (L2) MHz, and users derive ranging information from these signals to triangulate an exact position on the surface of the Earth [*Parkinson and Spilker*, 1996]. L1 and L2 are modulated with a P (precise) code, and L1 is also modulated with a C/A (coarse acquisition) code; both carriers are also modulated with navigation messages [*Torge*, 1991] containing information about satellite clock, health and broadcast orbital parameters. There are two fundamental observables in GPS: pseudorange (P) and carrier phase (Φ). The pseudorange measurement is derived from the time difference from transmission to reception (dt) and the conversion of this time difference into a range between satellite and receiver. GPS satellites use a very precise time scale called GPS time. GPS time is the result of an adjustment made between all of the atomic clocks in the GPS satellites and some ground-based atomic clocks [*Kaplan*, 1996]. Once the adjustment is performed, GPS time is uploaded to the satellites by the control segment of GPS. GPS receivers however usually have internal clocks (oscillators) that are of poor quality. This significantly lowers the cost of receivers to users. For this reason four pseudoranges are actually needed to solve for a position: three to estimate the three-dimensional position and one to estimate the receiver's clock offset from GPS time.

The carrier phase measurement is a reconstruction of the range from the fractional part of the phase at reception (φ), added with an integer number of wavelengths (λ) solved for in the geometric range. The integer number of wavelengths is called the ambiguity (N), and must be solved for during the adjustment process, in order to exploit the precise nature of carrier phase observations. Rough code estimates of position can be used to narrow the

search space of possible ambiguities. Once ambiguities are solved, the carrier phase observable becomes more accurate than the pseudorange observable due to low noise.

Mitigation of error sources is imperative for accurate positioning. A common technique used is the double differencing of measurements between receivers and satellites, as given mathematically in Equation 2.1 and visually in Figure 2.1. This effectively eliminates the receiver and satellite clock errors and reduces orbital errors and other spatially correlated errors.

$$\Delta\nabla\Phi = (f_{2B} - f_{1B}) - (f_{2A} - f_{1A}) \tag{2.1}$$

where

f_{ij} is the carrier phase observable to the ith satellite at the jth receiver and

F is the double differenced carrier phase observation

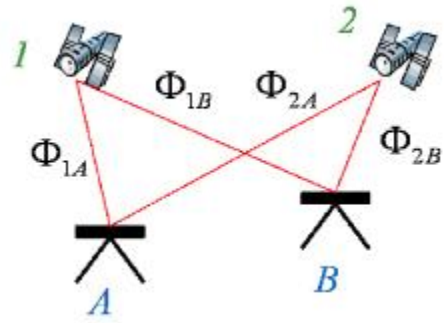

Figure 2.1. Double differencing GPS carrier phase observables.

The observation equation for double differenced carrier phase measurements is given as follows (after *Cannon* [2001]):

$$\Delta\nabla\Phi = \Delta\nabla r + \Delta\nabla dr + l\Delta\nabla N - \Delta\nabla d_{ion} + \Delta\nabla d_{trop} + e_{\Delta\nabla mp} + e_{\Delta\nabla noise} \quad (2.2)$$

Where

Δ	denotes the difference of observations between receivers
∇	denotes the difference of observations between satellites
ρ	is the geometric range
$d\rho$	represents orbital errors
λ	is the wavelength of the signal
N	is the integer ambiguity
d_{ion}	represents ionospheric delay
d_{trop}	represents tropospheric delay
$e_{\Delta\nabla mp}$	is the double differenced multipath, and
$e_{\Delta\nabla noise}$	is the double differenced receiver noise.

Satellite and receiver clock error terms that exist in the zero-difference carrier phase equation are cancelled out since similar satellites and receivers are being viewed as seen in Figure 2.1. The various error sources remaining in the double difference observation (assuming ambiguities are solved for correctly) and possibilities for their mitigation are discussed in Section 2.2.

2.2 GPS Error Sources

2.2.1 Orbit Errors

Orbital errors are caused by the inaccuracy with which a GPS satellite's position is known. This error is greatly reduced by double differencing although there can be some residual error when longer baselines are used. Inaccuracies in ephemeris occur because

all forces acting upon the satellites are not measured directly by observations made from the Earth [*Wells*, 1987], and thus cannot be predicted. Several different types of orbital products are available through the International GPS Service (IGS). The IGS is a support network for GNSS (Global Navigation Satellite Systems) which started routine activities in 1994 to provide ephemerides for precise geodetic applications [*Hofmann-Wellenhof et al.*, 1997]. Orbit products include the following:

- Broadcast – these orbits are uploaded to GPS satellites and transmitted as part of the navigation message, as well as being available from IGS. The advantage to these orbits is that they are available in real-time but there is a tradeoff in compromised accuracy since they are purely predicted; broadcast orbits are accurate to about 2 m [*IGS*, 2004].
- Ultra-rapid – are made available on FTP servers which hold IGS data at 0300, 0900, 1500, and 2100 UT each day, these orbits are given for 48 hours, with the first 24 hours being derived from observations with a three-hour latency and the second 24 hours being predicted. These orbits have three-hour latency but the predicted portion is available in real-time. The predicted and observed portions of this ephemeris give satellite coordinates which are accurate to ~10 cm and < 5 cm respectively [*IGS*, 2004].
- Rapid – rapid orbits are available approximately 17 hours after observations are made from GPS ground stations, and have an accuracy of <5 cm [*IGS*, 2004].
- Precise – precise orbits are available with about 13 days latency, and are determined from hundreds of ground tracking stations' measurements. The accuracy of precise orbits is <5 cm [*IGS*, 2004]. If the application permits, most processing is done with precise orbits due to the fact that it provides very complete ephemeris (if a certain satellite ephemeris is not available at the time the rapid orbit is available, an effort is made to make it available in the precise ephemeris) and there is enough time to correct blunders which may have made their way into other orbital products.

The magnitude of differential orbital errors is discussed in section 2.2.6.

2.2.2 Ionospheric Effects

To obtain perfect ranges from GPS, signals would have to travel at exactly the speed of light on their journey from satellite to receiver. In order for signals to travel at the speed of light along a path, the index of refraction along that path has to be equal to one (i.e. they have to travel in a vacuum). However in the ionosphere (the layer of the atmosphere from 50-1000 km above the Earth's surface [*Kaplan*, 1996]), free electrons cause changes in the index of refraction, which changes the propagation of the GPS signal. Free electrons are prominent in the ionosphere due to the sun's ultraviolet energy ionizing molecules in this region. Variations in the amount of free electrons in the ionosphere are a function of season, time of day, latitude, solar storm activity and sunspot cycle.

The ionosphere affects the group and phase of the GPS signals equally in magnitude but with the opposite sign, and the effect is dependent on the number of free electrons along the signal path and the frequency of the signal (i.e. this is a dispersive effect). For a single measurement, the delay on the phase and group of the GPS signal (denoted with subscripts *p* and *g*) is given in Equations 2.3 and 2.4 (after *Kaplan* [1996]).

$$d_{ion,p} = -\frac{40.3\,TEC}{f^2} \tag{2.3}$$

$$d_{ion,g} = \frac{40.3\,TEC}{f^2} \tag{2.4}$$

where *TEC* is the total electron content in electrons/m^2 along the signal path and f is the frequency of the signal.

If measurements are taken on both the L1 and L2 frequencies, an ionosphere-free (IF) double difference observable can be obtained by combining the observations:

$$\Delta\nabla\Phi_{IF} = \Delta\nabla\Phi_{L1} - \frac{f_{L2}}{f_{L1}}\Delta\nabla\Phi_{L2} \tag{2.5}$$

Using this observation during positioning removes the first-order effects of the ionosphere (99% of this error source), allowing for the removal of this error to the centimetre-level even with low elevation observations and high atmospheric electron content [*Brunner and Gu*, 1991].

2.2.3 Troposphere

The troposphere is the lowest layer of the atmosphere, with average pressure and temperature characteristics as shown in Figure 2.2. Pauses are presented at the general range of heights at which they are usually located at in this figure. The feature of the troposphere that makes it of interest is that most weather occurs here, and that humans have direct daily contact with it. The dynamics of the troposphere is of great interest to meteorologists who predict weather. Large-scale processes as well as small-scale processes must be modelled well in this layer to provide accurate short- and long-term forecasting. Some examples of processes that are modelled are: drag due to gravity waves, frictional processes, water vapour movement and winds. The process of numerical weather prediction (NWP) involves the arduous task of parameterizing all dynamics which will affect weather, and using this information to predict forward from an initial known state [*Andrews*, 2000].

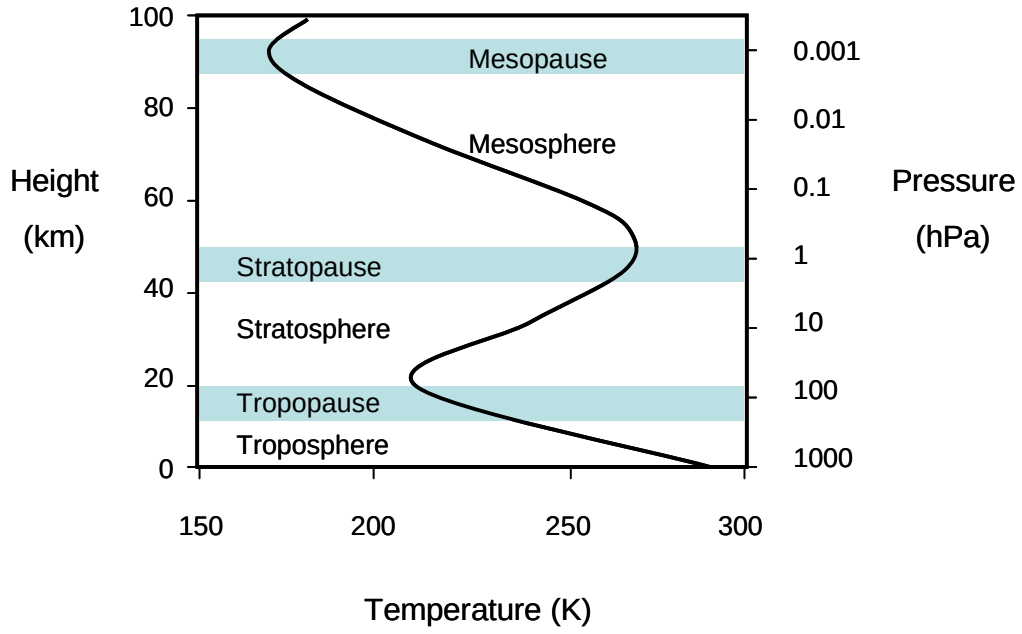

Figure 2.2. General vertical structure of the first 100 km of the atmosphere (after *Andrews* [2000]).

2.2.3.1 The Neutral Atmosphere's Effect on GPS Signals

The neutral atmosphere's effect on GPS signals comes from two layers: the stratosphere and troposphere. Because the main effect is due to the troposphere, effects from both tropospheric and stratospheric regions have been dubbed "tropospheric" by GPS researchers and geodesists [*Gregorius and Blewitt*, 1998]. The region of the neutral atmosphere which has an impact on GPS signals will thus herein be referred to as troposphere. When meteorologists speak of the troposphere, they refer to the area of the atmosphere where weather occurs, which is ~0-10 km above the surface of the Earth, but in general GPS researchers refer to the troposphere as 0-40 km above the Earth.

As with the ionosphere, the index of refraction (n) in the troposphere is not equal to one at a position p along a ray path. This causes a slowing and a bending in the GPS signal leading to an overall excess in path length (Δs)

$$\Delta s = \underbrace{\int_{path} [n(p)-1]dp}_{\text{slowing}} + \underbrace{[S-G]}_{\text{bending}} \tag{2.6}$$

where

S is the curved ray path and

G is the geometric path (after *Bevis et al.* [1992]).

Since the bending term is much smaller (less than or equal to one centimetre for elevation angles over 15° [*Bevis et al.*, 1992]) than the slowing term it is often ignored. The total effect is not dispersive at L-band frequencies, and cannot be removed by differencing measurements made on different GPS frequencies.

2.2.3.2 Tropospheric Range Error

In Equation 2.6, the index of refraction '*n*' was used. To make this number a magnitude that is easier to work with, it is common to use instead, refractivity (N), which is

$$N \equiv 10^6 (n-1) \tag{2.7}$$

Tropospheric range errors (Δs) are due to water vapour and other gases in the neutral atmosphere and can be related to the total refractivity (N_T) along a satellite to receiver path (ds):

$$\Delta s = \int_{sv}^{rx} \frac{N_T}{10^6} ds \tag{2.8}$$

N_T can be expressed in terms of hydrostatic (N_H) and wet (N_W) components, and can be described by the following equation [*Ware et al.*, 1997]:

$$N_T = \underbrace{77.6\frac{P}{T}}_{N_H} + \underbrace{3.73\times 10^5 \frac{e}{T^2}}_{N_W} \tag{2.9}$$

where

P is the total air pressure in mb

T is the temperature in degrees Kelvin and

e is the partial pressure of water vapour in mb

The total tropospheric range delay (Equation 2.8) can therefore be expressed as the sum of both wet and hydrostatic components:

$$\Delta s = SHD + SWD \tag{2.10}$$

where *SHD* and *SWD* refer to the slant hydrostatic and slant wet delays respectively along the signal path. The wet delay component is confined to the troposphere which is usually the lower 12 km of the atmosphere, with the largest concentration of delay-causing water being in the lowest 4 km [*Parkinson and Spilker*, 1996].

The wet delay is not trivial to estimate using theoretical/empirical models because the water vapour content of the atmosphere is highly variable and does not reliably fit to a pre-described model. Significant differences of water can be seen over tens of kilometres spatially and in the time span of a few hours [*Parkinson and Spilker*, 1996]. It is therefore of importance and interest to GPS users who wish to mitigate its effects for precise positioning.

2.2.3.3 Mitigation of Tropospheric Effects

Spatially correlated ionosphere and troposphere errors are both greatly reduced by double-differencing GPS measurements. If two receivers are close together it is more probable that they are making measurements through an atmosphere with the same physical characteristics and constituents, in which case similar errors will cancel out during the double differencing. When long baselines are used, spatial decorrelation of the atmosphere plays a factor. The effectiveness with which the double differenced measurement eliminates atmospheric errors changes as a function of the activity in the ionosphere and troposphere, which corresponds to factors such as storms, solar cycle, time of day, location on the Earth, weather and season. This is because for the double difference measurement to remove atmospheric errors, they need to be essentially the same magnitude for all measurements in the difference. Spatial decorrelations in the atmosphere across the double difference measurement cause the differencing of measurements to not mitigate atmospheric errors fully. This can be seen most notably with longer baselines, where the probability of spatial decorrelation of the atmosphere is higher. Modelling the effects of the troposphere empirically can help mitigate this error source, and this approach is discussed in Chapter 3. Estimates of tropospheric error can also be solved for as an additional unknown in an adjustment process using the same GPS data as used for positioning. This approach is discussed as well in Chapter 3.

2.2.4 Multipath

Multipath is the reception of a signal that has reflected off a surface before arriving at the antenna, resulting in a longer range than normal as shown simply in Figure 2.3. Multipath can cause the GPS signal phase and coded information (navigation data) to become distorted, and under severe multipath, receiver tracking loops can lose lock [*Kaplan,* 1996].

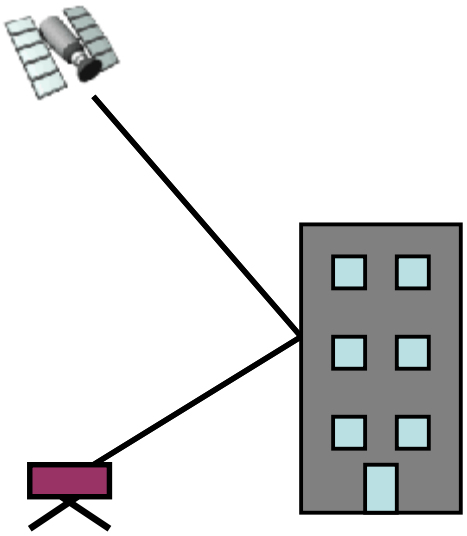

Figure 2.3. Simplistic view of multipath.

Multipath is repeatable for a static antenna with a constant environment, as the GPS constellation repeats itself every 24h solar time (or 23h56m sidereal time). The effects of multipath on positioning can be reduced if the location for receiver set-up can be chosen with few near-by obstacles. For many applications (especially kinematic positioning, indoor positioning and positioning in urban environments), the location of the receiver cannot be negotiated or obstacles around it cannot be moved and therefore multipath must be dealt with on the receiver design level, a notable example of which is NovAtel's Narrow Correlator technology (see *Van Dierendonck et al.* [1992] for details). In a static positioning environment, multipath can be eliminated from a position solution by averaging over its period. Antenna gain patterns can be designed to filter multipath or signals from low elevations and physical additions can be made to antennas such as choke rings in order to mitigate the effects of multipath [*Hofmann-Wellenhof*, 1997]. A typical magnitude of multipath for an antenna located above reflectors is in the range of 50 cm to 2 m [*Kaplan*, 1996]. Table 2.1 in Section 2.2.6 gives values for typical magnitudes of differential carrier phase multipath error.

2.2.5 Receiver Noise

Receiver noise is a random error that is created by the receiver during its calculation of pseudorange or carrier phase measurements from the reception of raw GPS signals. GPS receiver noise comes from natural sources such as: thermal noise in the electronics, antenna noise from picking up naturally produced electromagnetic radiation or the antenna's own electronic noise, systems noises in the cables and receiver and receiver tracking loop noise [*Langley*, 1997]. The receiver noise power needs to be exceeded by the GPS signal power received in order for a measurement to be made.

The magnitude of receiver noise is related to the type and quality of receiver being used, and cannot be removed from GPS measurements aside from modelling or by smoothing methods such as averaging over a number of samples. Magnitudes of differential carrier phase receiver noise are given in Table 2.1 along with a summary of all error sources discussed in this section.

Zero-baseline tests can be performed to estimate the magnitude of receiver noise whereby a signal from one antenna is split into two identical receivers and the measurements are double differenced. It should be noted however that this will provide an optimistic estimation since there is noise generated at the antenna, and these particular noise sources dominate the overall receiver noise [*Langley*, 1997].

2.2.6 Magnitudes of GPS Error Sources

To obtain the most accurate results possible, differential carrier phase positioning is most commonly utilized. Table 2.1 gives a summary of the expected error magnitudes when this type of processing is used (after *Lachapelle* [2002]). These are in addition to a 'zero' 3-5 mm phase noise error.

Table 2.1 Typical Differential Carrier Phase Error Budget

Error Source	Description	Residual Error
Orbit	Broadcast	<± 0.5 ppm
Orbit	Precise	<± 0.005 ppm
Troposphere	Hopfield Model Employed	± 0.2-0.4 ppm
Ionosphere	L1 only – no IF	± 0.2-20 ppm
Ionosphere	Dual Frequency	N/A
Multipath	Site specific	± 3-15 mm
Noise	Rx Dependant	± 0.2-2 mm

Positioning accuracies are determined by the mapping of these range accuracy measures into the position domain through a measure of satellite geometry called the Dilution of Precision (DOP). Equation 2.11 shows the form of how DOP relates to position error for single-point positioning.

$$\text{Position Error} = \text{DOP} \times \text{range measurement error} \tag{2.11}$$

For differential carrier phase positioning, a relative dilution of precision, or RDOP value can be derived for a period of processing time. This value can then be multiplied by the double-difference measurement error to obtain a relative position error for the solution.

CHAPTER 3

MODELLING AND ESTIMATION OF TROPOSPHERIC WATER VAPOUR

3.1 Troposphere Models

As was mentioned in Section 2.2.3.2, the total tropospheric delay can be broken down into hydrostatic and wet components. Models exist to estimate the tropospheric hydrostatic and wet delays. These models make assumptions about the general physical characteristics of the troposphere to derive equations that describe it, and may also use empirical data to augment these descriptions. The hydrostatic delay component is about 90% of the total tropospheric delay and is well described by models given surface meteorological information. The remaining ~10% is due to water vapour and is difficult to describe with modelling owing to its high spatial and temporal variability [*Hofmann-Wellenhof et al.*, 1996].

Once hydrostatic or wet delays are modelled in the zenith (d_{hz} and d_{wz} respectively), slant delays can be retrieved by mapping the delay down to the corresponding elevation angle by a mapping function. The mapping functions used can differ for the type of delay being mapped.

$$d_{tot} = d_{hz} m_h(e) + d_{wz} m_w(e) \tag{3.1}$$

where

d_{tot} is the total troposphere delay on a GPS measurement

$m_h(e)$ is a hydrostatic mapping function and

$m_w(e)$ is a wet mapping function.

Equation 3.1 directly relates to *Ds* (total delay), *SHD* (slant hydrostatic delay) and *SWD* (slant wet delay) given in the last chapter (Equation 2.10) as such:

$$\underbrace{d_{tot}}_{\Delta s} = \underbrace{d_{hz}\, m_h(e)}_{SHD} + \underbrace{d_{wz}\, m_w(e)}_{SWD} \tag{3.2}$$

Models and the mapping function used in this work are given in the following sections. More models are described in *Shrestha* [2003].

3.1.1 Hydrostatic Delay Model

Isolating the hydrostatic delay component of a total tropospheric delay can be done in the zenith with a hydrostatic model and accurate surface pressure measurements. While utilizing the Saastamoinen model [*Saastamoinen*, 1972] for this purpose it is generally accepted that the error associated with this delay model is at the millimetre-level [cf. *Bevis et al*., 1992]:

$$d_{hz} = \frac{0.22765 P_S}{(1 - 0.00266\cos(2j) - 0.00028h)} \tag{3.3}$$

where

d_{hz} is the zenith hydrostatic delay in cm

P_S is the surface pressure in mb

φ is the latitude and

h is the station height above sea level in kilometres [*Bar-Sever et al*., 1998].

The Saastamoinen model has the advantage of being simple to employ since the only information needed is surface pressure and location, and is the equation of choice for zenith hydrostatic modelling in this work.

To give an idea of the zenith magnitudes of hydrostatic delay for locations within southern Alberta, Saastamoinen's hydrostatic delay model was employed using surface pressure measurements found at six locations. The results are shown in Figure 3.2 for September 1, 2003, which saw no significant weather events. During this day, the stations with pressure data available were:

- BRKS – Brooks
- CREM – Cremona
- HANA – Hanna
- SUND – Sundre
- THIL – Three Hills
- VULC – Vulcan

For clarity, these stations and their coordinates in WGS-84 are shown in Figure 3.1.

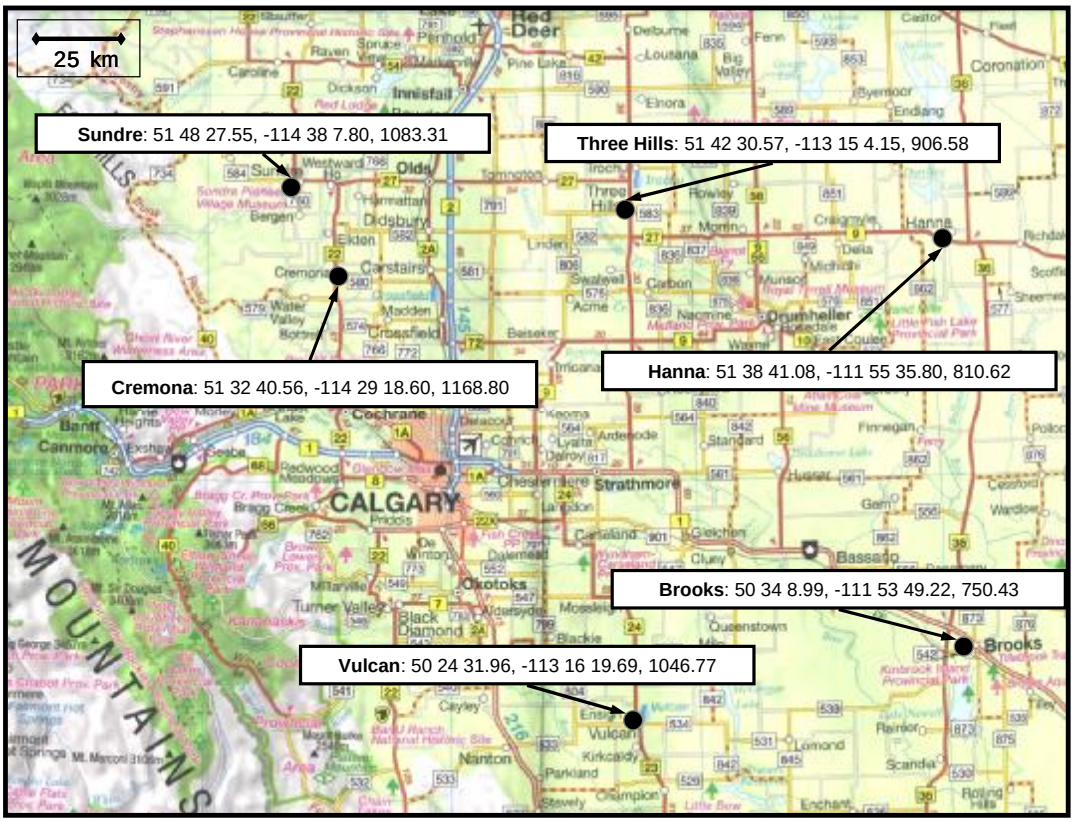

Figure 3.1. Locations of the six stations in southern Alberta used for zenith hydrostatic delay computation superimposed on a map. Latitude and longitude are given in dms, and height in metres, all in the WGS-84 ellipsoidal system.

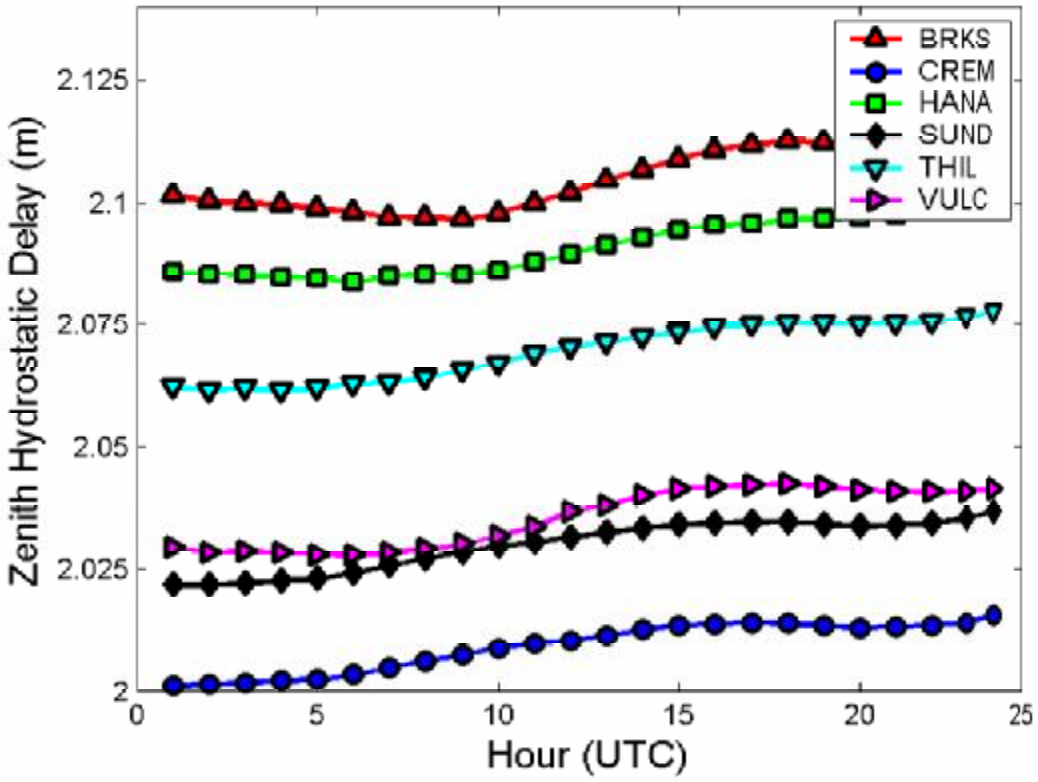

Figure 3.2. Zenith hydrostatic delay for September 1, 2003 at six locations in Southern Alberta.

The differences in the magnitudes of hydrostatic delay correlate to the height differences in the stations generally, with the highest stations, Cremona and Sundre having the lowest amount of atmosphere above them and consequently the lowest magnitude of hydrostatic delay. Brooks and Hanna being the lowest stations, have the most amount of atmosphere above them and therefore the most hydrostatic delay. In general it can be said that for stations in southern Alberta, they will experience zenith hydrostatic values of about 2 m.

Another hydrostatic delay model is the Hopfield model [*Hopfield*, 1969] of hydrostatic delay which assumes the dry refractivity can be expressed quartically [cf. *Mendes*, 1999]:

$$d_{hz} = 77.6\times10^{-6}\frac{P_S}{T_S}\frac{H_d^e}{5} \tag{3.4}$$

where

H_d^e is the dry equivalent height in metres (the height above the station at which the dry refractivity is zero) and

T_S is surface temperature.

The Hopfield model uses assumptions of a constant lapse rate in temperature and height parameters are derived from a least-squares fit to collected data [*Hopfield*, 1969].

3.1.2 Wet Delay Model

The wet delay model is less precise than the hydrostatic model, as water vapour is not highly correlated to surface meteorological measurements and can have great spatial and temporal variation. Assumptions made in many hydrostatic models such as hydrostatic equilibrium are not valid for wet delay models, making accurate model description difficult. Wet delay models are in general accurate to 2-4 cm [*Skone*, 2003].

Wet delay models are not employed in this work as wet delays are being estimated with GPS measurements; however the Hopfield zenith wet delay model [*Hopfield*, 1969] is given below as an example [cf. *Mendes*, 1999].

$$d_{wz} = 10^{-6} N_{WS} \frac{H_w^e}{5} \tag{3.5}$$

where H_w^e is the wet equivalent height (the height above the station at which the wet refractivity is zero) and e_S is the surface partial pressure of water vapour in mb. N_{WS} is the wet refractivity at the surface as developed by *Smith and Weintraub* [1953]:

$$N_{WS} = 3.73\times10^{5}\,\frac{e_S}{T_S^2} \tag{3.6}$$

3.1.3 Mapping Functions

In order to map a tropospheric delay from zenith down to its slant path for the respective elevation angle, mapping functions are employed. The simplest mapping function (*m(e)*) is entirely dependent on the elevation angle (*e*) of the observation

$$m(e) = \frac{1}{\sin(e)} \tag{3.7}$$

This is a good approximation for elevation angles above ~15º [*Skone*, 2003]. Specific mapping functions exist for each delay (i.e. total delay, wet or hydrostatic delay). The elevation angle cutoff being used also helps determine what mapping function is being used as some only apply to certain elevation angles. The Niell wet mapping function [*Niell*, 1996] is used in this work to map wet delays from the zenith as it is considered accurate to 3°:

$$m_{wet}(e) = \frac{\dfrac{1}{1+\dfrac{a_{wet}}{1+\dfrac{b_{wet}}{1+c_{wet}}}}}{\dfrac{1}{\sin(e)+\dfrac{a_{wet}}{\sin(e)+\dfrac{b_{wet}}{\sin(e)+c_{wet}}}}} \tag{3.8}$$

Coefficients a_{wet}, b_{wet} and c_{wet} are derived from the station's latitude and a look-up table as given in Appendix B and *e* is the elevation angle.

Magnitudes of zenith wet delays mapped with the Niell wet mapping function to their respective elevation angle are given in Figure 3.3 for September 1, 2003. These delays were found for the same six stations that were used to find the magnitude of zenith hydrostatic delays in Section 3.1.1: Brooks, Cremona, Hanna, Sundre, Three Hills and Vulcan. These stations are plotted on a map in Figure 3.1 for reference.

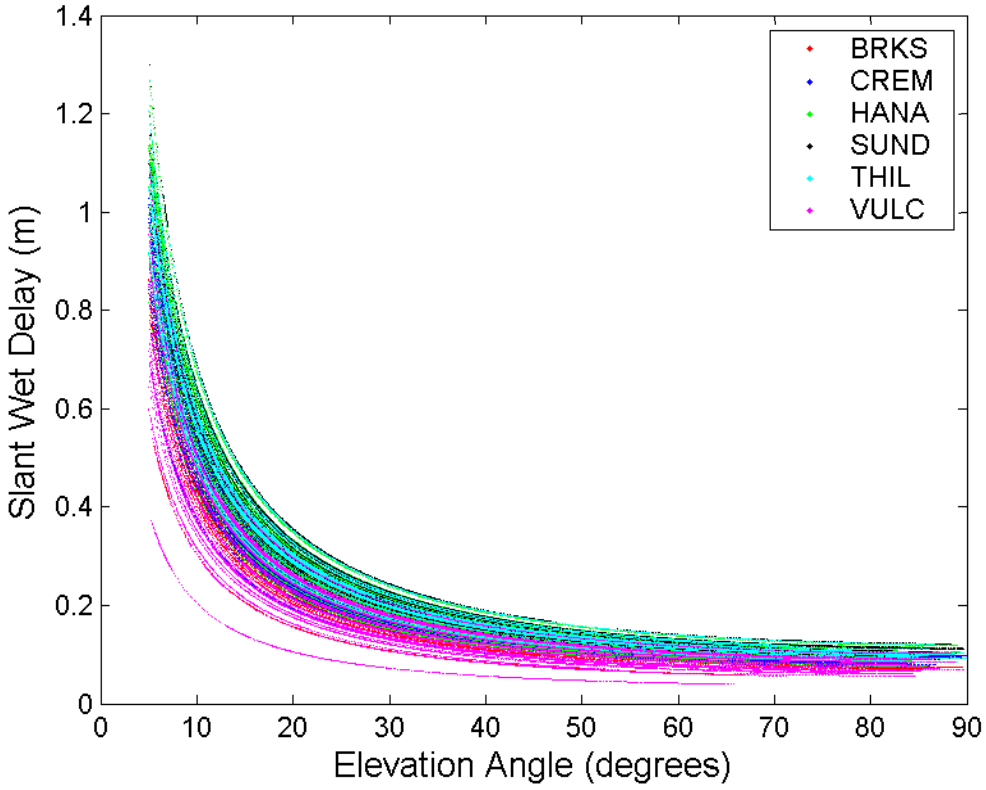

Figure 3.3. Slant wet delays for September 1, 2003 at six locations in Southern Alberta.

SWD from the different stations plotted in Figure 3.3 were very similar, so plotting the stations in different colours (as was done for hydrostatic delays in Figure 3.2) resulted in a plot with the last stations plotted overlapping the first ones. SWD to all satellites in view from each station are presented in Figure 3.3. From this it can be seen that SWD values for the southern Alberta region are anywhere from under 10 cm to 1.3 m on September 1, 2003, depending on the elevation angle to the satellite being viewed.

The Niell hydrostatic mapping function [*Niell*, 1996] is also given below.

$$m_{wet}(e) = \frac{1}{\sin(e) + \dfrac{a_{hydro}}{\sin(e) + \dfrac{b_{hydro}}{\sin(e) + c_{hydro}}}} + \left[\frac{1}{\sin(e) + \dfrac{a_{ht}}{\sin(e) + \dfrac{b_{ht}}{\sin(e) + c_{ht}}}} \right] \times \frac{H}{1000} \qquad (3.9)$$

The hydrostatic coefficients in this formula are found using an interpolation formula and table which is given in Appendix B, *H* is the station height above sea level and

$$a_{ht} = 2.53 \times 10^{-5}\, km$$
$$b_{ht} = 5.49 \times 10^{-3}\, km$$
$$c_{ht} = 1.14 \times 10^{-3}\, km$$

3.2 Wet Delay Estimation Using GPS

Because empirical and theoretical models poorly characterize wet delays, different methods of determining this error source exist. One approach is to estimate wet delays in an adjustment process using GPS observations. If the receiver's coordinates are known, the positioning problem can be inverted (coordinates held fixed) such that the tropospheric delay observed in the signal can be used along with surface meteorological data to derive the water vapour content in the atmosphere.

Networks of GPS reference stations exist worldwide for differential positioning purposes. Once all other sources of ranging error are mitigated successfully, calculations can be made to determine parameters describing the water vapour profile surrounding each

station [*Bevis et al.*, 1992]. This information in turn can be combined with information from other GPS reference stations to derive the three spatial dimensions plus temporal dependence of water vapour over a region of interest.

The inversion of the positioning problem to retrieve water vapour estimates can be thought of as the following simplification of a measurement made to one satellite (Figure 3.4). When a range measurement is made to a satellite there is a true geometric range between the satellite and the receiver, and there is the measured range which is longer than the true range due to error sources. If all other errors sources were successfully mitigated the total delay on the signal would be due to the neutral atmosphere only. Knowing the receiver and satellite coordinates allows for recovery of the total slant tropospheric delay. If the total tropospheric slant delays are assumed to be azimuthally symmetric (meaning no horizontal variation) they can be mapped up to the zenith with the use of a mapping function. This particularly strengthens the solution if slant delays are averaged over a time period since more observations (GPS slant observations) are used to solve for the unknowns (total zenith delay). Using the surface pressure to remove the hydrostatic component of the total zenith delay isolates the zenith wet delay (ZWD). A conversion factor called Π (nominally 0.15, [*Bevis et al.*, 1992]) can be applied to ZWDs to convert them to precipitable water vapour (PWV). PWV has more meaning to meteorologists because it represents how much liquid water would exist if all the vapour in the zenith direction above the receiver precipitated.

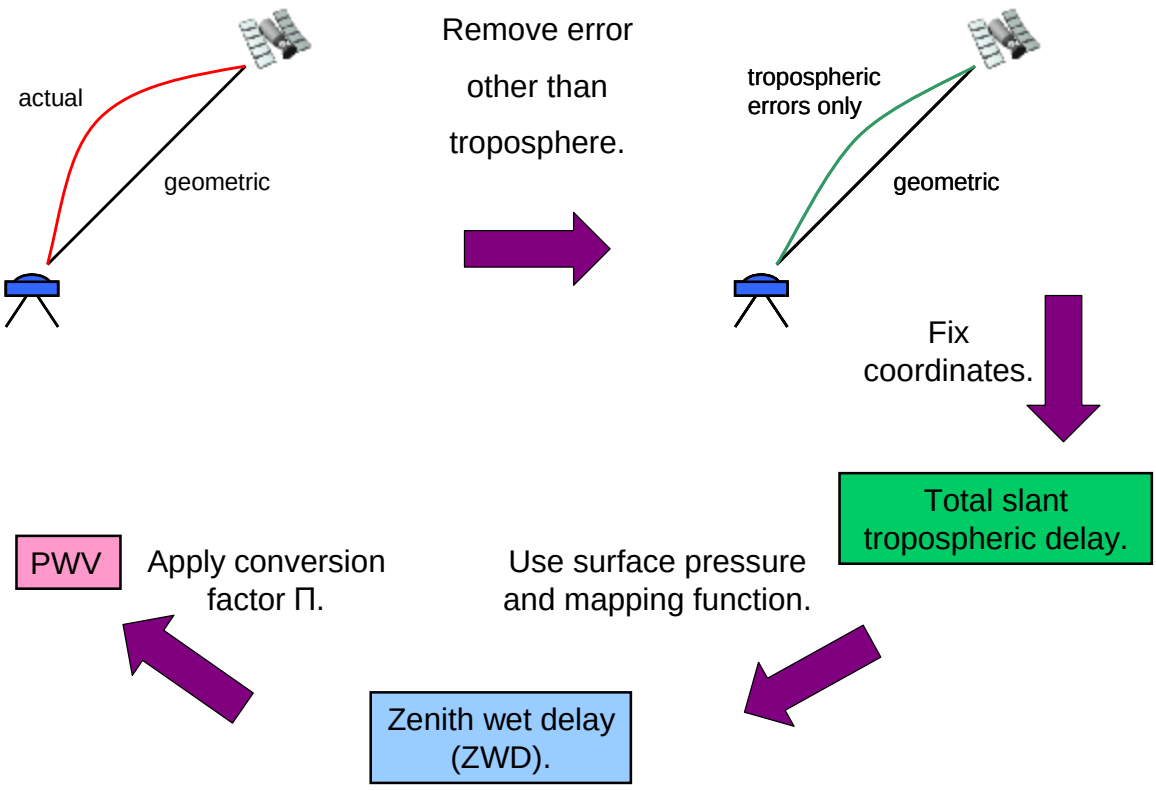

Figure 3.4. Overview of water vapour retrieval from a single GPS observation.

When zenith delays are solved for in a network approach with GPS, at least one baseline needs to be long enough so that the elevation angle to a satellite from one station will be different than for the other observing stations, otherwise absolute delays for each station cannot be solved for. This problem is described mathematically in Appendix A. If a long baseline cannot be utilized during processing, absolute delays can be retrieved across a network using additional measurements of water vapour such as those from a water vapour radiometer (WVR) which gives an absolute measurement of water vapour. In this way, relative measurements of wet tropospheric delay can be levered from the station with the absolute measurement.

3.3 Bernese Software Estimation of Atmospheric Water Vapour

Bernese Version 4.2 is a commercially available GPS processing software package developed by the Astronomical Institute at the University of Berne in Switzerland. Bernese can be used for geodetic GPS processing, and makes several different processing strategies available to the user [*Hugentobler et al.*, 2001]. Bernese was used during the generation of slant wet delays (SWD), which are the input observables in the tomographic estimation of the distribution of water vapour (see Section 3.4). An overview of Bernese estimation of water vapour is also given in *Shrestha* [2003].

3.3.1 Bernese Pre-Processing

Before the actual estimation steps, certain routines must run in order to clean the GPS data for optimal estimation. One of the first steps is to transfer all GPS input data into a proprietary Bernese format. 30 second GPS RINEX observation files and precise orbit files from the International GPS Service (IGS) are first converted to Bernese format before they can be used. If phase centre offset information for the receivers used is available, it may be input into a phase centre offset file to be used during processing.

The Bernese program CODSPP is then run on all observation files. This program computes receiver clock corrections for all stations, and estimates coordinates for all stations from the input pseudorange measurements. This is the only step in which code measurements are used. The receiver clock correction needs to be checked that it is known to 1μs, and the a posteriori RMS error from the position adjustment can be checked that it is not unreasonable. The ionosphere-free (IF) observable described in Section 2.2.2 is used for the adjustment performed in this step of processing.

SNGDIF is then used to form single difference measurements between receivers. These single difference measurements are later double differenced and used as observations for the estimation of tropospheric parameters. Different strategies can be employed to have Bernese create single differences which maximize the number of observations, or use the shortest baselines which is advantageous when error sources are being minimized for coordinate determination. The strategy employed for each day of troposphere processing was to run the SNGDIF program once in OBS-MAX mode to determine what baselines had the highest number of observations, and then to manually make some single difference measurements which would include the shorter baselines in the network, and use combinations of baselines which would optimize the number of observations, while using short and long baselines.

The program MAUPRP is then executed and its main purpose is to mark cycle slips and repair them. When tracking the carrier phase measurement (described in Chapter 2) the fraction of the wavelength at reception is measured (ex. 0 to 2π) by the receiver and this value changes in time. This is added to the integer number of wavelengths in between the satellite and receiver to reconstruct the range. When lock is lost and regained, a jump in the integer number of cycles occurs. MAUPRP finds cycle slips and will repair them if possible.

3.3.2 Bernese Estimation

The final program run in Bernese is GPSEST, and it performs the least-squares adjustment. This program is run three different times in order to obtain an IF-fixed solution [*Langen and Fortes*, 2002]:

1. GPSEST is run for the purpose of obtaining double difference IF solutions for coordinates with float carrier phase ambiguities.

2. Ambiguities are resolved for all baselines using GPSEST using L1 and L2 double difference observables. The coordinates found in the previous step are used.
3. GPSEST runs the ambiguities found from the last step with the IF double difference observable to form an IF-fixed solution and total tropospheric zenith delays are found.

During the solution for total zenith tropospheric delays, the entire delay at a particular site is solved for every hour (batch mode), and the dry Niell mapping function (see Section 3.1.3) is used to map the slant measurements to the zenith. (Note: The Bernese V 4.2 software refers to the hydrostatic Niell mapping function as 'dry' [*Hugentobler et al.*, 2001], so the same naming convention was maintained here.) Although the delay being mapped is the total delay, which is a combination of wet and dry components, the dry Niell mapping function is used because there is a limited choice of mapping functions available in Bernese and "dry Niell" is recommended for troposphere estimation by the software's developers [*Hugentobler et al.*, 2001]. The elevation mask angle used during processing is 5º, and the Niell mapping function is appropriate to use for all observation elevation angles above 3º. This is the recommended method from the developers of Bernese [*Fortes*, 2004; *Hugentobler*, 2001].

3.3.3 Slant Wet Delays

Once total zenith delays are solved for in Bernese, the hydrostatic zenith component is removed using the Saastamoinen hydrostatic model (see Section 3.1.1). The measurement is then mapped down to the appropriate elevation angle using the wet Niell mapping function using the following formula:

$$SWD = d_{wz} m_w(e) \tag{3.10}$$

It should be stated that Bernese also allows for the retrieval of gradients which can be used to account for azimuthal asymmetries which are not dealt with by the use of a mapping function alone. However, estimating these additional unknowns in the Bernese solution worsened the total zenith delay estimation and was therefore deemed a poor estimation. In this work, the wet Niell mapping function is used to convert from the zenith to slant, and azimuthal asymmetries are not taken into account.

3.4 Tomographic Estimation of Wet Refractivity

Tomography is the inversion technique used to derive the spatial distribution of a desired quantity from integrated measurements, and has been long used in the field of medicine for imaging of the human body (magnetic resonance imaging or MRI for example). If SWD observations from a network of GPS receivers derived from Bernese processing are used as input, wet refractivity fields (N_w in Equation 2.8) can be retrieved over the network using tomographic inversion, as demonstrated by researchers in the past [e.g. *Braun and Rocken*, 2003; *Shrestha*, 2003; *Flores et al*., 2000]. The three-dimensional N_w fields can then be used to predict tropospheric wet delays for a GPS user at any location within the GPS network.

3.4.1 Technique

For this work, a tomographic model first described by *Skone and Shrestha* [2003] is used. If it can be assumed that wet refractivity can be described as constants in vertical layers, and horizontal variations as expansions in latitude and longitude, the basic observation equation relating *SWD* to wet refractivity (N_W) as a function of geodetic latitude (j), longitude (l) and height (h) is given as follows:

$$SWD = 10^{-6} \int_{sv}^{rx} N_W(j, l, h)ds \tag{3.11}$$

Allowing for the estimation of second order expansion coefficients in latitude and longitude, and estimating the integral by a summation, the formula for *SWD* can be rewritten as

$$SWD = \sum_{i=1}^{n} (a_{0i} + a_{1i}\Delta j + a_{2i}\Delta j^{2} + a_{3i}\Delta l + a_{4i}\Delta l^{2} + a_{5i}\Delta j \Delta l)dh_i \tag{3.12}$$

where

$a_{0i}, \ldots, a_{5i}$ are the expansion coefficients for layer i (there are n layers in total)

dh_i is the path length through layer i

$Dj = j_i - j_o$

$Dl = l_i - l_o$ and

(j_o, l_o) is the expansion point (the centroid of the network)

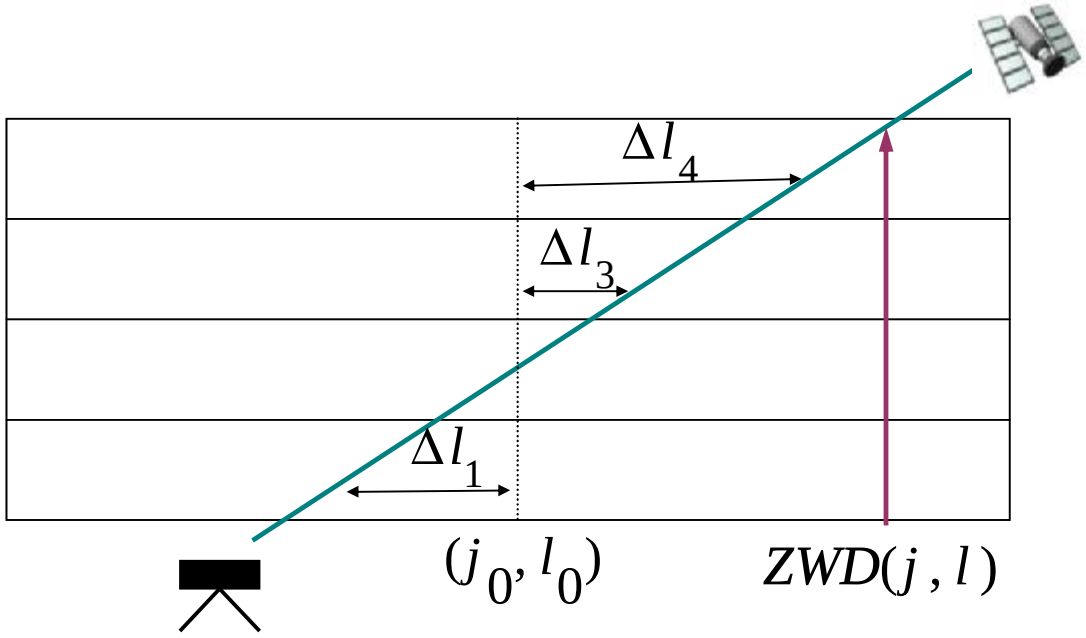

Figure 3.5. Example of tomography geometry with four layers and one SWD observation. The expansion point (j_o, l_o) is where the expansion coefficients a_{01}, … , a_{04} are derived for. ZWD can be recovered from this model for GPS users within the region by integrating as shown.

The geometry of the tomographic approach used is shown in Figure 3.5. Zenith wet delays (ZWD) can be recovered from this model for any location within it by integrating through the model vertically. Equation 3.13 is a slightly modified form of Equation 3.12 and can be used to integrate through the part of the model that lies directly above a particular location to derive ZWD.

$$ZWD = \sum_{i=1}^{n} (a_{0i} + a_{1i}\Delta j + a_{2i}\Delta j^{2} + a_{3i}\Delta l + a_{4i}\Delta l^{2} + a_{5i}\Delta j \Delta l)dh_i \qquad (3.13)$$

where

$Dj = j_i - j_o$ with j_i being the latitude at the location where ZWD is being derived

$Dl = l_i - l_o$ l_i being the longitude at the location where ZWD is being derived and

Previous work with the tomographic model utilized in this work by ***Shrestha*** [2003] showed that by using layers with a thickness of 1 km, inversions could be resolved in the profiles retrieved for wet refractivity. This vertical resolution is therefore deemed to be satisfactory for the work undertaken here, and a layer thickness of 906.25 m is used, with eight layers. The lowest station used in the adjustment is 750 m, although most stations are 1000 m or greater in height. The model space used in the estimation started at 750 m. Tomographic model layer heights are shown in Table 3.1.

Table 3.1 The Eight Layers Used in the Tomography Model and Layer Bottom and Top Heights in Metres

Layer	Bottom Height	Top Height
1	750.00	1656.25
2	1656.25	2562.50
3	2562.50	3468.75
4	3468.75	4375.00
5	4375.00	5281.25
6	5281.25	6187.50
7	6187.50	7093.75
8	7093.75	8000.00

Kalman filter estimation is utilized for the tomographic solution with details given below.

3.4.2 Kalman Filter Estimation

All unknowns (coefficients $a_{0i}, \ldots, a_{5i}$ as described in Equation 3.12) are derived as stochastic parameters using a first-order Gauss-Markov process to describe time-varying correlations in wet refractivity. This type of process was chosen as it was successfully utilized in previous work with the same tomographic model [*Shrestha*, 2003]. Model coefficients vary with time by the system model given in Equation 3.13.

$$a_{ij}(t_{k+1}) = e^{-b(\Delta t)} a_{ij}(t_k) + w \tag{3.14}$$

where

$\frac{1}{b}$ is the correlation time, which is assumed to be 30 minutes and

$\Delta t = t_{k+1} - t_k$

Estimated parameters at one time are only partially correlated with those derived at later epochs; the normalized autocorrelation function is $e^{-b(\Delta t)}$. The uncorrelated part of the prediction (the process noise) is a white noise sequence given by

$$q(t) = s^2[1 - e^{-2b(\Delta t)}] \tag{3.15}$$

with s^2 given for different expansion values as

$a_0: \quad s^2 = 10\ (mm/km)^2$

$a_1, a_2: \quad s^2 = 2\ (mm/km)^2/\deg^2$

$a_3, a_4, a_5: \quad s^2 = 0.5\ (mm/km)^2/\deg^4$

These values were chosen by *Shrestha* [2003] in his work with this model, and were also used for this work.

Standard Kalman filter equations were used and are listed below (after *Gelb* [1974]).

- Prediction from time t_k to t_{k+1}

$$\mathbf{x}^-(t_{k+1}) = \mathbf{\Phi}(t_k, t_{k+1})\mathbf{x}^+(t_k) + \mathbf{w} \tag{3.16}$$

$$\mathbf{P}^-(t_{k+1}) = \mathbf{\Phi}(t_k, t_{k+1})\mathbf{P}^+(t_k)\mathbf{\Phi}(t_k, t_{k+1})^T + \mathbf{Q}(t_k) \tag{3.17}$$

- Update at time t_{k+1}

$$\mathbf{x}^+(t_{k+1}) = \mathbf{x}^-(t_{k+1}) + \mathbf{K}[\mathbf{z}(t_{k+1}) - \mathbf{H}(t_{k+1})\mathbf{x}^-(t_{k+1})] \tag{3.18}$$

$$\mathbf{P}^+(t_{k+1}) = [\mathbf{I} - \mathbf{K}\mathbf{H}(t_{k+1})]\mathbf{P}^-(t_{k+1}) \tag{3.19}$$

where the gain matrix **K** is given by

$$\mathbf{K} = \mathbf{P}^{-}(t_{k+1})\mathbf{H}^{T}(t_{k+1})[\mathbf{H}(t_{k+1})\mathbf{P}^{-}(t_{k+1})\mathbf{H}^{T}(t_{k+1}) + \mathbf{R}(t_{k+1})]^{-1} \tag{3.20}$$

and

x is a vector of the quantities to be estimated (coefficients $a_{0i}, \ldots, a_{5i}$ in this case)

F is the transition matrix

H is the design matrix

R is a matrix of covariance information for the observations **z** and

P is a matrix of covariance information for the estimated parameters **x**

Single GPS SWD observations are given the variance of

$$s^{2} = (1.6\,cm^{2}) / \sin(e) \tag{3.21}$$

as based on the work of *Shrestha* [2003] in which he compares SWD observations made from Bernese processing with GPS observations to those from a water vapour radiometer located on the same roof as the GPS antenna at the University of Calgary.

The observation matrix will be a vector of observational inputs which could be slant wet delays or direct observations of wet refractivity for a given layer.

$$\mathbf{z} = \begin{bmatrix} l_1 \\ \mathbb{M} \\ l_n \end{bmatrix} \tag{3.22}$$

where *n* is the number of observations at this epoch. The observation covariance matrix **R** is then formulated as

$$\mathbf{R} = \begin{bmatrix} s_1^2 & & \\ & \mathbf{O} & \\ & & s_n^2 \end{bmatrix} \tag{3.23}$$

where s is the standard deviation associated with a particular observation and the off-diagonal elements of this matrix are zeros. The estimated or unknown parameters in the adjustment are coefficients given in Equation 3.12. If there are n vertical layers used in the model, there will be n unknowns estimated that represent each layer's expansion point wet refractivity ($a_{01}, \ldots, a_{0n}$) as well as five gradients which represent the horizontal expansion in latitude and longitude. These five gradients were kept the same for all layers in this work, although if desired they could be derived separately for each layer to reflect different levels of horizontal variation in the different layers. This approach was chosen because SWD are being estimated with azimuthal symmetry (as per Section 3.3.3), the horizontal variations will be very similar for all the layers being estimated. It should be noted that having azimuthal symmetry does not equate to keeping the gradient parameters constant throughout the layers, but does point to some degree of averaging over horizontal variations. If j gradient terms are being estimated, the vector of unknowns for the adjustment is

$$\mathbf{x} = \begin{bmatrix} x_1 \\ \vdots \\ x_i \\ x_{i+1} \\ \vdots \\ x_{i+j} \end{bmatrix} \tag{3.24}$$

The general construction of the design matrix for any given epoch is as such [*El-Sheimy*, 2004].

$$\mathbf{H} = \begin{bmatrix} \frac{\partial x_1}{\partial l_1} & \frac{\partial x_2}{\partial l_1} & \mathbf{L} & \frac{\partial x_j}{\partial l_1} \\ \mathbb{M} & \mathbf{O} & & \\ \frac{\partial x_1}{\partial l_n} & \frac{\partial x_2}{\partial l_n} & \mathbf{L} & \frac{\partial x_j}{\partial l_n} \end{bmatrix} \tag{3.25}$$

where j is the number of unknowns at this epoch, which is determined by the number of layers and coefficients being estimated as per Equation 3.12.

3.4.3 Limitations

When retrieving water vapour fields from ground-based GPS networks, the geometry of the observing stations can present a challenge, in that the topography of the local area puts constraints on the locations where receivers can be placed. Unless there is sufficient vertical separation of GPS receivers, the vertical distribution of water vapour is not well observed and thus not well estimated.

A sample wet refractivity profile, derived using the tomography approach for a network of GPS receivers covering a 200 km by 200 km area, shows poor vertical resolution in Figure 3.6. Negative refractivity values at lower altitudes are clearly wrong. In this case, a difference of only 400 m exists between highest and lowest stations in the network, indicating a relatively flat topography. While a ground-based GPS network provides good horizontal resolution of wet refractivity fields, additional sources of vertical profile information (as available from radiosondes, climate models, or radio occultations) may strengthen the vertical resolution and improve overall accuracies.

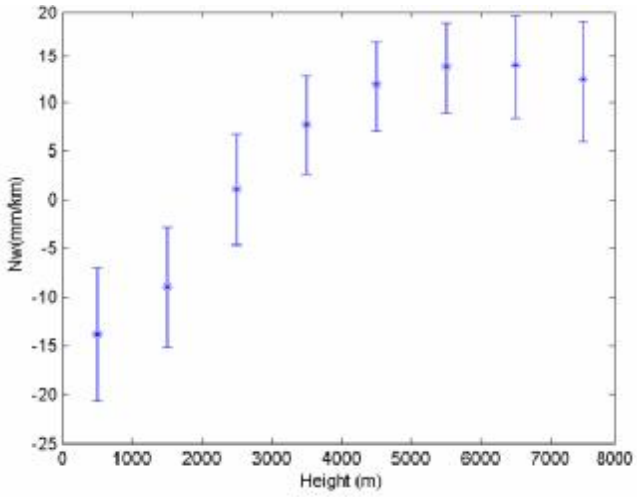

Figure 3.6. A poorly defined profile of wet refractivity from tomographic retrieval over a GPS network with 400 m overall vertical separation between stations.

3.5 Additional Sources of Vertical Water Vapour Distribution

Since the vertical geometry of the observing stations in some GPS networks is not adequate for good vertical resolution of water vapour distribution during tomographic retrieval, additional measurements could be assimilated into the tomographic model that would help strengthen the vertical resolution. The measurements listed in the sections below are described in detail in Chapter 4.

3.5.1 Radiosondes

In meteorology, radiosondes or weather balloons are used as an accurate measure of atmospheric conditions. A popular radiosonde instrument in use by Canadian meteorologists is the Vaisala RS80. Below 15 km, the Vaisala RS80 has been tested to measure temperature accurately to ± 0.5K [*Nash*, 2004a], and relative humidity to within ± 5% [*Nash*, 2004b]. The Vaisala webpage quotes accuracies for the RS80 as 0.2 K and <3% relative humidity [*Vaisala*, 2004].

Due to cost, radiosonde launch sites are sparsely located across Canada. In the province of Alberta there is only one regular radiosonde launch site at Stony Plain which is located by the province's capital of Edmonton, ~300 km north of Calgary (for the location of the province of Alberta relative to North America, see Figure 1.2). Radiosondes are typically released once every 12 hours for weather prediction, which is the norm for the National Weather Service in the United States as well [*Niell et al.*, 2001]. The assimilation of such measurements into ground-based GPS tomography could strengthen the vertical wet refractivity retrieval, although the drawback to using such measurements is that they are temporally and spatially sparse.

3.5.2 Climate Information

Measurements from Stony Plain may not be representative of local weather conditions for a tomographic model produced from GPS data in the Calgary area (~300 km away). It is possible, however, to derive general climate information from monthly averages of all radiosonde measurements taken at Stony Plain, Alberta - which if constrained properly can give some additional information for a tomographic adjustment performed for a network some distance away. This information could be used to model vertical wet refractivity profiles for assimilation into the tomographic wet refractivity retrieval algorithm using GPS network data.

The variability over one month makes for an increase in the uncertainty of wet refractivity for the climatological model when compared to the single radiosonde observations. Assimilating the monthly average profile into a ground-based tomography approach should essentially constrain wet refractivity values for the upper layers of the model since the lower layers are highly variable over one month and will have large variances associated with them.

3.5.3 Radio Occultations

Profiles of atmospheric parameters can be found from the occultation of low Earth orbiting satellites. This technique has been used successfully in the past to derive atmospheric structures of other planets in our solar system. For example, *Fjeldbo et al*. [1971] outline how the Mariner V satellite was used to derive profiles of Venus' atmospheric refractivity, molecular number density, temperature, pressure and radio-frequency absorption. Such radio occultation experiments in the past have been only used for a limited amount of time [*Aparicio*, 2004] in order to determine the general structure of other planet's atmospheres. For Earth, satellites called Low Earth Orbiters (LEOs) are launched into orbit at altitudes 600-800 km (significantly lower than the GPS satellites) with a GPS receiver payload. These satellites then receive signals from GPS satellites as they set or rise from behind the Earth, as viewed from the area of interest (Figure 3.7).

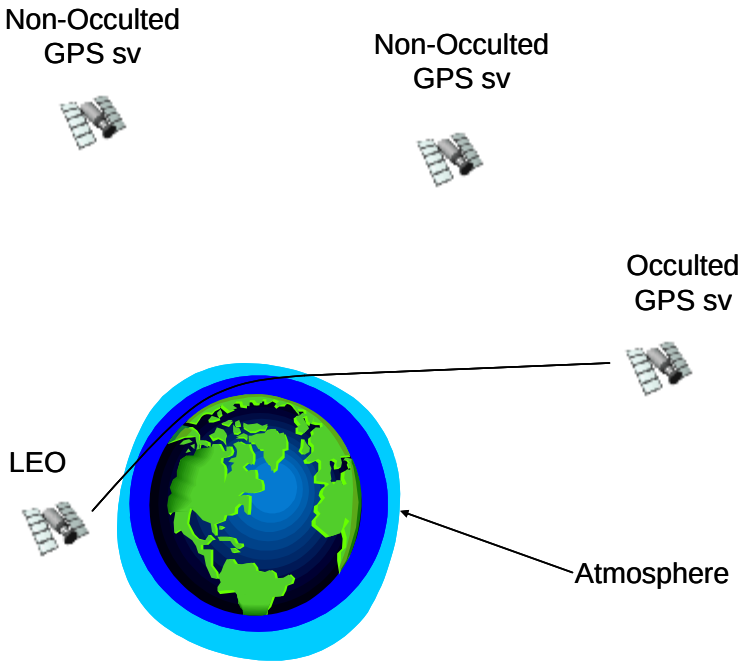

Figure 3.7. Overview of GPS occultations (after *Businger* [1996]).

Using assumptions of the atmospheric parameter relations, and Doppler measurements from the LEO, calculations can be made to derive profiles for parameters such as pressure, temperature and water vapour.

During an occultation (which can occur during LEO rising or setting) the signal from LEO to GPS satellite goes through successive layers of the atmosphere. GPS clock and receiver clock errors must be removed from observations for this technique to be successful, and this can be achieved by single or double differencing GPS occultation measurements with those made from GPS stations on the Earth [*Rocken et al.*, 2000].

The main observable in occultations is the Doppler or phase rate caused by the refractivity of the atmosphere. A Doppler shift is induced in a GPS RF signal when [*Cannon*, 2001]:

- There is relative motion between the receiver and transmitter. This can be due to real motion or perceived motion due to satellite or receiver clock drift.
- The atmosphere (ionosphere or troposphere) shifts the frequency of the travelling signal due to refractivity.
- Multipath shifts the frequency of the travelling signal.

In order to use the Doppler shift to retrieve refractivity, other sources of Doppler need to be removed or mitigated from the solution. If precise orbits for LEO and GPS satellite are found, then the Doppler due to this effect can be determined and removed from the total observed Doppler shift. There is little that can be done once a space vehicle is launched to reduce multipath due to the structural environment of the receiver or transmitter. Launching a piece of equipment into space is an expensive endeavour and thus the equipment launched is usually fitted for several different scientific purposes.

Currently, there are a number of low-Earth orbiting satellites with a GPS payload (e.g. CHAllenging Minisatellite Payload – CHAMP, Satelite de Aplicanciones Cientificas C – SAC-C) and there are plans in place for a six-satellite system in the near future, such as the Constellation Observing System for Meteorology, Ionosphere and Climate (COSMIC), which is planned to be launched in 2005. First results from the CHAMP mission have indicated that vertical profiles of humidity agree well with European Centre for Medium-Range Weather Forecast (ECMWF) and National Centers for Environmental Prediction (NCEP) specific humidity data [*Wickert et al.*, 2001a] to about 1.5 kilometres above the surface of the Earth, where atmospheric water vapour and multipath degrade the solution [*Gregorius and Blewitt*, 1998].

Occultation measurements of relative humidity have advantages over measurements made by ground-based GPS receivers. Firstly, occultations are measurements that can be made at locations where it would be very difficult to physically place a receiver such as over oceans and inhospitable environments (e.g. the Antarctic). Occultations also provide measurements made from a totally different geometry than there is available from the surface of the Earth, providing a high vertical resolution in resulting profiles. However, occultations also have some disadvantages.

In order to become a valid source of information for weather and climate studies, measurements should be available for an area of interest with a high density in space and time. The existing single-satellite missions for GPS occultations do not provide a constant source of data for users; occultations from CHAMP number approximately 200-300 per day, and they are sparsely located around the globe [*Wickert*, 2001b]. Future missions planned for low Earth orbiting satellites with a GPS payload will increase the feasibility of the use of occultation data for meteorological and climate studies, as thousands of occultations will be observed per day [*Wickert*, 2001b].

During any time in an occultation, the signal path travels through several hundred kilometres of the atmosphere (see Figure 3.7) and is therefore more of an average representation of the atmosphere at the occultation tangent point (the location on the Earth of the signal's closest approach where the occultation measurement is taken as valid) than a measurement for a specific location. This can be disadvantageous when looking to recover refractivity features over a local region, and must be taken into account when this type of measurement is assimilated into a regional atmospheric model.

CHAPTER 4

DATA SET AND PROCESSING DESCRIPTION

4.1 The Southern Alberta Network

The Southern Alberta Network (SAN) consists of 14 GPS receivers across southern Alberta, as deployed in 2003 by the Geomatics Engineering Department at the University of Calgary (Figure 4.1). Station coordinates found for the SAN for 2003 are given in Table 4.1 (although a GPS station at Didsbury was established in 2003, it was never used for GPS processing and therefore coordinates are unknown or "N/A"). The spacing between SAN stations was designed to be approximately 50 km in order to give optimal results for mesoscale numerical weather prediction, and at the same time allowing for precise positioning applications.

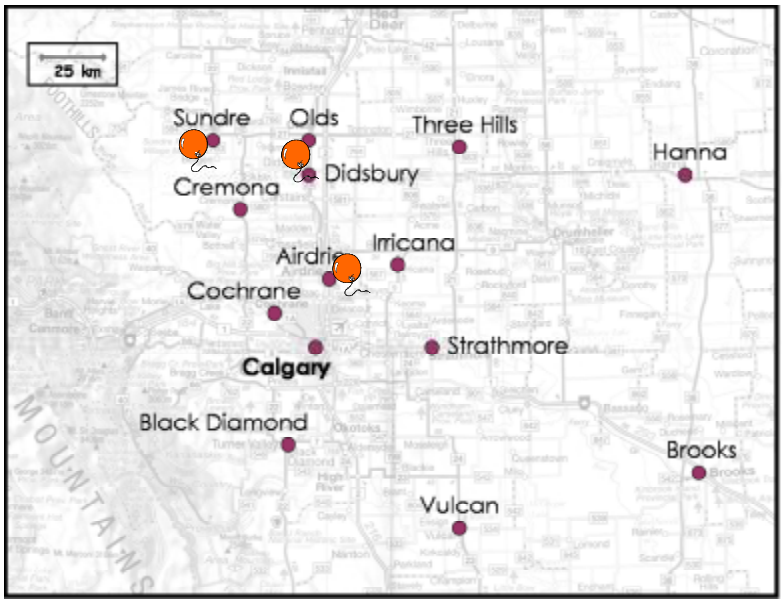

Figure 4.1. The Southern Alberta Network during A-GAME 2003. GPS stations shown in purple dots, locations of radiosonde launches shown as orange balloons.

Table 4.1 Coordinates for SAN Stations in WGS-84

Station	Latitude N (d m s)	Longitude (d m s)	Height (m)
Airdrie	51 16 57.83	-114 00 15.12	1081.44
Black Diamond	50 40 41.67	-114 14 6.78	1191.39
Brooks	50 34 8.99	-111 53 49.22	750.43
Calgary	51 04 45.84	-114 07 57.72	1116.80
Cochrane	51 11 22.56	-114 28 9.48	1142.30
Cremona	51 32 40.56	-114 29 18.60	1168.80
Didsbury	N/A	N/A	N/A
Hanna	51 38 41.08	-111 55 35.80	810.62
Irricana	51 19 21.51	-113 36 33.18	920.94
Olds	51 47 31.61	-114 05 35.76	1031.80
Strathmore	51 03 39.24	-113 23 14.28	975.40
Sundre	51 48 27.55	-114 38 7.80	1083.31
Three Hills	51 42 30.57	-113 15 4.15	906.58
Vulcan	50 24 31.96	-113 16 19.69	1046.77

Each station in the SAN consists of a NovAtel MPC GPS receiver and NovAtel 600 antenna, and all stations used for this study have a Paroscientific MET3A meteorological instrument as well. The MPC GPS receiver not only houses a Euro4 card for GPS measurements, but also a hard disk for data storage, ethernet connections and a web server for communications. The MPC is pictured in Figure 4.2.

Figure 4.2. The NovAtel MPC [*NovAtel*, 2003]

MPCs in the SAN are configured to log raw pseudorange and carrier-phase measurements on L1 and L2. These files can be manually downloaded via the receiver's web page on the Internet, or by connecting the MPC to a laptop computer onsite. Data from the network is also currently streamed to a server at the University of Calgary. MET3A measurements are fed through the MPC receiver so that RINEX-formatted files are created on the MPC as well. Figure 4.3 below shows the MET3A instrument at the Sundre SAN site.

Figure 4.3. MET3A instrument at Sundre.

The MET3A measures [*Paroscientific*, 2004]

- pressure with accuracies of ±0.08 hPa from 620 to 1100 hPa,
- temperature with accuracies ±0.1 ºC from -50 to +60 ºC and
- relative humidity an accuracy of ±2% from 0 to 100 % at 25 ºC.

GPS data and RINEX-formatted meteorology data have been collected from all sites manually using a laptop and a crossover Ethernet cable to connect to the MPC, or from the archive of the data streams that are being logged. Once the data was pooled together, GPS data then had to be converted into RINEX format. NovAtel offers various conversion tools to carry out this process; Tconvert and Convert4 [*NovAtel*, 2003] were used for this purpose.

4.2 The A-GAME 2003 Data Collection Campaign

A data collection campaign was carried out during July 14-28, 2003 which was the period of time most likely to see hail and thunderstorms over the SAN [*Nicholson et al.*, 2003]. This data collection campaign was named the "Alberta – GPS Atmospheric Monitoring Experiment 2003" or A-GAME 2003. This campaign was a collaborative effort between

- the Geomatics Engineering Department from the University of Calgary
- the Meteorological Service of Canada and
- Weather Modification Incorporated / The Alberta Severe Weather Management Society.

The Geomatics Engineering Department is a division of the faculty of Engineering at the University of Calgary. The A-GAME data was of interest to researchers in the positioning, location and navigation field of Geomatics, particularly with respect to the SAN data for use in a multiple-reference station approach for better GPS positioning (see

Alves et al. [2004] and *Alves et al.* [2001] for details of work being undertaken in this area). For this application, information derived from the SAN would be used to correct GPS real-time kinematic position estimates determined within the SAN. A-GAME was also of interest to those working in the environmental engineering area for its ability to determine water vapour over the southern Alberta area accurately for applications such as meteorology, weather forecasting and hydrology studies.

The Meteorological Service of Canada (MSC) is an organization that is interested in the dissemination of weather information and warnings/watches across the country and research and education directed towards climate and weather.

Weather Modification Incorporated and The Alberta Severe Weather Management Society are interested in weather modification in southern Alberta through hail-cloud seeding. They base their operations in Alberta out of the Olds/Didsbury Airport where they release radiosondes and also operate TITAN radar, which measures precipitation through reflectivity or the backscattering of radio waves from water and ice in the atmosphere [*Andrews*, 2000]. They also deploy airplanes from various locations in southern Alberta to do hail-seeding during meteorologically active months. A recent publication on the operations of WMI and affects on precipitation can be found in *Krauss* [2003].

The Geomatics Department collected ground-based GPS data during the campaign, and dealt with any receiver problems that arose during this time remotely or through site visits. Two temporary sites were also maintained during A-GAME 2003 campaign, in order to strengthen network geometry, although these stations are not used in this work and are thus not shown in Figure 4.1.

MSC and WMI arranged for release of regular radiosondes during A-GAME 2003 at the sites indicated in Figure 4.1. Radiosondes were also released during times of severe

weather from the three sites. Results from Sundre radiosondes were not as accurate due to the fact that they were stored for a long period of time before use, and also they were tracked visually. Radiosondes released from Olds/Didsbury Airport (WMI) and Airdrie Airport were the Vaisala RS80.

4.3 Radiosonde Data

4.3.1 Airdrie Constraints

During A-GAME 2003, single radiosondes were released at Olds/Didsbury Airport (located halfway between Olds and Didsbury), Airdrie and Sundre. Airdrie radiosonde measurements were used as input observations into the tomographic model, to serve essentially as vertical profile constraints.

Observation variances were derived from the laws of error propagation with temperature and relative humidity having uncertainties as given by the manufacturer [*Vaisala*, 2004]. Section 5.2.1 shows mathematical details of these observations assimilation into the tomographic model. These radiosonde profiles are generally assumed to be most valid for a one-hour period after launch, and results presented in Chapter 6 not only uses one-hour validity, but also test a case study of long-term validity over eight hours from launch time.

4.3.2 Stony Plain Monthly Averaged Radiosondes

In the province of Alberta normally the only location where radiosondes are released is from Stony Plain which is located near the province's capital of Edmonton. This location is ~200 km from the north edge of the SAN. Because these radiosondes are likely to contain some information that would be helpful for overcoming limitations of the tomography model (see Section 3.4.3 for details) due to the strong vertical resolution of

radiosonde measurements, they were also assimilated into the tomography model (results in Chapter 6).

Radiosonde observations made in every month of 2003 at Stony Plain were averaged by Craig Smith from the Meteorological Service of Canada (MSC) and the variance observed in each parameter over each month was given in the data files as a standard deviation. Because of this averaging, and the fact that Stony Plain is located well outside of the network, these observations generally represent a climatological model for the entire province rather than a measurement valid for a specific location and time as were the Airdrie radiosonde constraints. A discussion on the details of the assimilation of these measurements into the tomography model follows in Chapter 5.

4.3.3 Olds/Didsbury Truth Data

Olds/Didsbury radiosonde observations were used as truth observations for comparison with tomography model predictions at that location. (Note that Airdrie and Olds/Didsbury sites are ~50 km apart.) For all analyses, radiosonde observations at Olds/Didsbury airport are taken as truth, as they have high accuracy (see Figure 5.3 for a visual representation of a single radiosonde and its error). These truth values of wet refractivity are integrated vertically to derive a truth zenith wet delay estimate.

In order to adequately assess the 4-D wet refractivity predictions versus truth, it is important that the radiosonde constraint information and the radiosonde truth data be available at approximately the same times. Unfortunately, the truth radiosonde observations at Olds/Didsbury did not always occur at the same time as the radiosonde launches from Airdrie. In fact, due to the expense of the radiosondes, the launches were in most cases purposely staggered in time from all three stations in order to get maximum temporal coverage of the atmosphere over the SAN during A-GAME 2003. On the days

used for processing (given in Section 4.4), the time differences between truth and constraint radiosondes are no more than two hours apart.

4.4 GPS and Radiosonde Data Processing

Two "quiet" days were processed for SWDs from the A-GAME 2003 data collection campaign - July 19 and 25, 2003. These days are deemed quiet because no significant storm events occurred over the network, which can be confirmed by the lack of activity seen in TITAN radar images for these days (for more information on the TITAN radar, see Section 4.2). July 20 and 26, 2003 saw large storms pass over the network and are processed as storm days. The main interest in processing storm and quiet days was to see if there was a difference in the quality of water vapour field retrieval if the atmosphere was more dynamic. Neither Olds nor Didsbury GPS observations were used in the tomography processing in order to independently assess model predictions in this region compared with radiosonde truth values.

GPS results shown here are processed using as many stations in the SAN as had surface pressure measurements and GPS data on days of interest. Some drop-outs were encountered at sites during the A-GAME 2003 campaign, and thus the stations used for processing were:

- July 19, 2003: Brooks, Calgary, Cochrane, Cremona, Strathmore, Sundre and Vulcan
- July 20, 2003: Brooks, Calgary, Cochrane, Cremona, Sundre, and Vulcan
- July 25, 2003: Airdrie, Brooks, Calgary, Cochrane, Cremona, Sundre and Vulcan
- July 26, 2003: Brooks, Calgary, Strathmore, Three Hills and Vulcan

In order to retrieve absolute and not relative troposphere measurements (see Appendix A), three IGS stations were included in the Bernese processing to derive SWD values:

ALGO (Algonquin Park in Ontario, Canada), DRAO (Dominion Radio Astrophysical Observatory in B.C., Canada) and NLIB (North Liberty, U.S.A.) which are approximately 2680 km, 430 km and 1890 km from the network, respectively. During all GPS processing, an elevation mask of 5º was used. This was to obtain the best possible accuracy from the GPS measurements [*Niell et al*., 2001]. This is due to increased observability with increased viewing in the lower layers of the troposphere, and because height errors in position cannot be separated from tropospheric errors without the use of low elevation data. For July data, three types of processing are conducted:

- Ground-based GPS stations alone. In this case, the tomography model uses only SWD input from available GPS stations. This approach is herein referred to as "GPS".
- The GPS approach is augmented by including radiosonde observations from Airdrie as observational input to the tomography model. This approach is herein referred to as "GPS + RS".
- The GPS approach is augmented by monthly averaged radiosonde observations from Stony Plain (~200 km north of the SAN's north edge). This approach is herein referred to as "GPS + AveRS".

Due to the expense of the radiosondes, the launches were in most cases purposely staggered in time from all three radiosonde launch sites in order to get maximum temporal coverage of the atmosphere over the SAN during A-GAME 2003. On the days used for processing, the time differences between truth and constraint radiosondes are as follows:

- July 19, 2003 – same time
- July 20 and 25, 2003 – one hour apart
- July 26, 2003 – two hours apart

4.5 Occultation Data

Total refractivity measures obtained through CHAMP occultations were obtained from Jens Wickert from the GeoForschungsZentrum (GFZ) in Potsdam, Germany from August 3 – October 26, 2003. These occultations were chosen as a starting data set since they occurred close to the SAN. These results were obtained using a canonical transform sliding spectrum (CTss) processing approach (for details see ***Wickert et al***. [2004]). The CTss method helps to mitigate negative refractivity biases for values derived for the lower troposphere. These biases are most common to (but not restricted to) retrievals made in the tropics. Details of the assimilation process for these observations are given in Section 5.4.

4.6 Global Environmental Multiscale (GEM) Model

In order to extract wet refractivity from the total refractivity derived from CHAMP occultations, profiles of temperature and pressure over the SAN were needed to derive hydrostatic refractivity in order to extract the wet refractivity from the total refractivity as given by CHAMP (seen in Equation 2.8). Hydrostatic refractivity was derived from the GEM model data. The GEM model is a complex data assimilation algorithm that uses observed data and applies dynamics models and atmospheric physics to hindcast atmospheric conditions. It is currently used by the Meteorological Service of Canada to produce background fields, short to long-range forecasts, regional and global scales. It provides meteorological parameters such as pressure, temperature and relative humidity for a specific region for 28 height levels (called eta levels), at a grid point spacing determined at the time of the model run [*Côté et al*., 2004].

4.7 Occultation and GEM Data Processing

GEM model data was supplied by Craig Smith from the Meteorological Service of Canada (MSC) in order to isolate wet refractivity from total refractivity supplied by the occultation measurements. The GEM model data gave pressure and temperature profile measurements to derive hydrostatic refractivity, which can be seen in the expression for total refractivity given in Equation 2.9.

The GEM model data supplied were for a 25 km grid spacing covering N 51.5-52.2º latitude and W 115.5-111.5º longitude on days of interest. September 1, 2003 was chosen for occultation processing due to the CHAMP occultation being located within the SAN and also located in the GEM model space provided from MSC. This occultation occurred at N 52.152° latitude and W 111.702° longitude. It was also chosen for the height down to which the CTss retrieval method gave estimates of total refractivity; if occultation retrievals of total refractivity were not found below 4 km, it was not used as it would only add information to half of the layers of the tomography model upon assimilation. Temperature and pressure profiles at the point closest to the occultation were then derived from GEM data. This GEM data point was found to be at N52.2003° latitude and W111.6200° longitude. The GEM data point does not exactly match the occultation location; however since the occultation measurement is made from an average over several hundred kilometres of the atmosphere this is assumed to be adequate. September 1, 2003 SAN data used during the occultation assimilation was from Brooks, Cremona, Hanna, Sundre, Three Hills and Vulcan - six stations. A 12-hour time span was processed from 01:45 -13:45 UTC, as the occultation measurement was tagged at 01:47:41 UTC. The occultation profile is assimilated throughout the entire processing time.

Unfortunately, no CHAMP occultations occurred over the SAN during A-GAME 2003, and thus there were no radiosondes to compare with the tomographic output (with

occultation observations assimilated). To make an assessment of the quality of the tomographic approach with occultation/GEM-derived wet refractivity, successive GPS stations were removed from the solution, and comparisons were made between the tomographic model for each GPS station and the GPS ZWD observations for each station left out of the adjustment.

CHAPTER 5

DATA ASSIMILATION

5.1 Description of Traditional Data Assimilation

Data assimilation (DA) describes the process by which observations are input to a model which predicts quantities for a span of time. DA is commonly used by those who perform numerical weather prediction (NWP). NWP is an initial value problem whereby an estimate of the present state of the atmosphere is made, and this state is propagated forward in time through a model. To be entirely described, the initial state required for NWP requires far more observations than are available, and thus it was found that a short range prediction made by the model could be fed back into the initial state description for later model runs [*Kalnay*, 2003]. Observations are used to make small corrections to the short-range forecast generated by the model. An interpolation needs to be formed between the observational input and the background generated by the model, and this can be done with successive correction methods (SCM), optimal interpolation (OI), 3D-variaional (3D-VAR) and 4D-variational (4D-VAR) methods or Kalman Filtering, which are discussed in *Kalnay* [2003]. An overview of the NWP process is shown in Figure 5.1.

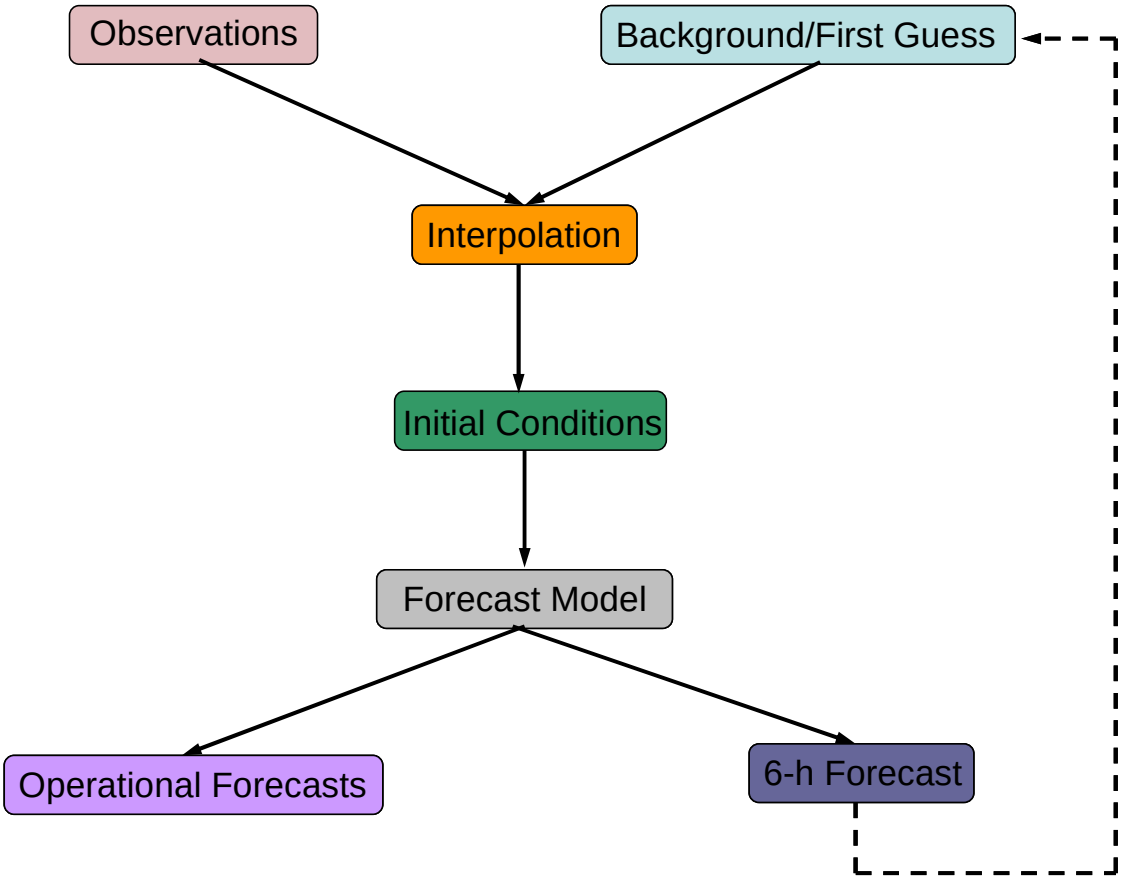

Figure 5.1. Flow diagram for a 6-hour NWP DA cycle (after *Kalnay* [2003]).

The accuracy with which forecasts are made with NWP is a function of the model used, the analysis method chosen to interpolate the data, and the data quality. Observations can be checked with background data for the same location and this provides a blunder detection method for the observations. Certainly computing power has also played a role throughout the last century in the complexity of the models utilized for NWP, and the amount of data assimilated [*Kalnay*, 2003].

Observations that are input into the DA scheme have nonuniform distribution; there are many more meteorological observations made over land masses such as North America and Europe and not many made over the oceans or at inhospitable locations such as Antarctica [*Kalnay*, 2003]. This combined with the fact that the model essentially feeds

back into itself causes spatially small, or rapidly occurring situations to not be resolved by NWP. In these situations forecasters need to determine how much emphasis to place on the NWP predictions versus observations made in the area where a disturbance is known to be occurring.

NOAA's Forecast Systems Laboratory (FSL) has been continuously calculating GPS-derived integrated quantities of atmospheric precipitable water (IPW) since 1994, and since 1997 has studied runs of their 4D data assimilation system for forecasting with and without the inclusion of such measurements. It was found that even though the new data being assimilated was an integrated quantity, the addition of these measurements showed an improvement consistently in short-range forecasts of relative humidity [*Smith et al*., 2000]. Data assimilation techniques have also been successful in characterizing the global distribution of ionospheric electron density distribution, through the successful inclusion of a wide range of observations into one, 3D model (for an example, see *Bust et al*. [2004]).

Considering the small spatial dimensions of the Southern Alberta Network (SAN) over which water vapour was to be determined, and also that the intent of this work was to determine only atmospheric water vapour distribution (versus the multitude of atmospheric parameters dealt with in NWP), a simple and easy to implement data assimilation scheme was sought. As far as the work performed in this publication is concerned, DA is a term which is used to describe the scheme by which additional observations were added to the existing ground-based GPS tomographic solution for wet refractivity. As an overview of the process, ground-based GPS SWD and vertical profile observations for each epoch were combined and put through a Kalman filter estimation technique, which uses previous estimates and estimate covariances in solutions for future epochs. A simple overview of the approach utilized in this work is given in Figure 5.2.

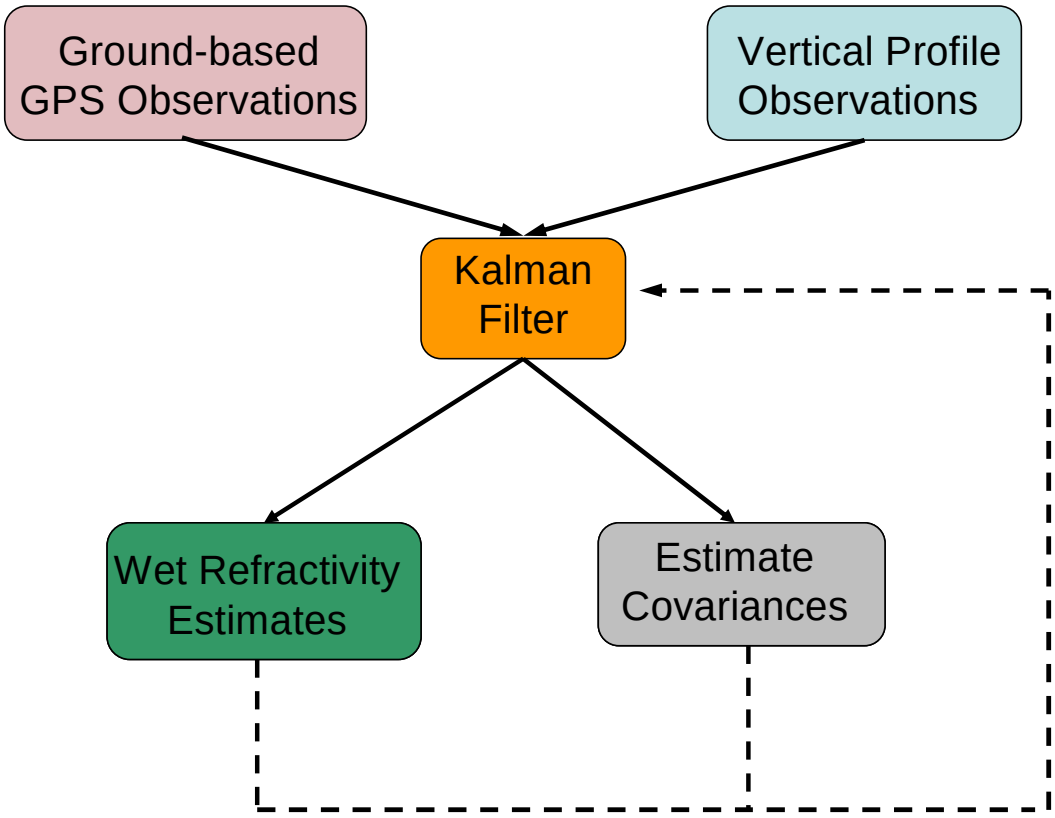

Figure 5.2. Flow diagram for the DA scheme used in this work.

5.2 Data Assimilation for Single Radiosonde Observations

Radiosondes are an accurate source of temperature, pressure and water vapour measurements. During the A-GAME 2003 campaign, single radiosondes were released at Olds/Didsbury Airport (located halfway between Olds and Didsbury), Airdrie and Sundre within the SAN. Airdrie radiosonde observations were assimilated into the tomography model and Olds/Didsbury Airport radiosondes were used as a truth to compare to the model output at this location.

To assimilate Airdrie radiosonde observations (RS) into the tomography model, it was necessary to convert RS observations into a format that could be easily added to the tomography model. To this end, they were formatted as direct observations of the wet

refractivity unknowns in each layer of the model. During the running of the tomography software for a day where RS measurements were to be assimilated, radiosonde files for the entire A-GAME 2003 campaign were searched to find those RS observations for the day of interest. Time tags given in these files were then used to determine which RS measurement was to be taken as valid. A routine was employed to determine how long RS measurements were to be assumed valid; different durations of validity are shown in Chapter 6 - with results from assuming RS measurements are valid over long and short periods of time. Normally, the RS measurement was taken to be valid over one hour, although Section 5.5 describes long-term testing where the RS was assumed valid over eight hours.

5.2.1 Mathematical Description of the Assimilation of RS Observations

Heights in the radiosonde observation files were given as orthometric heights, and they were converted to WGS-84 ellipsoidal heights using Natural Resources Canada Geodetic Survey Division's software GPS.H. To make measurements of wet refractivity, the radiosonde meteorological measurements were averaged for each layer being used in the model (i.e. the eight layers of 906.25 m thickness) and then N_W was calculated for each layer.

Meteorological measurements made by radiosondes from A-GAME 2003 that are needed to make calculations of wet refractivity are temperature (*T*) and relative humidity *(RH*). From temperature the saturation pressure of water vapour (*es*) can be calculated and from that and *RH*, the partial pressure of water vapour (*e*) can be derived, which combined with temperature yields wet refractivity (see Equations 5.1-5.3). The N_W values were calculated using the following equations from the *ICS* [2004]:

$$\log_{10}(es) = \frac{-2937.4}{T} - 4.9283\log_{10} T + 23.5470 \tag{5.1}$$

$$e = \frac{RH(\%) \times es}{100} \tag{5.2}$$

where

es is the saturation pressure of water vapour in hPa or millibars

T is the temperature in Kelvin

e is the vapor pressure in hPa or millibars

As a final step N_W was calculated from Equation 2.9 as

$$N_W = 3.73 \times 10^5 \left(\frac{e}{T^2} \right) \tag{5.3}$$

Values for truth wet refractivity in the layers of the tomography model derived from radiosondes released at Olds/Didsbury Airport were also calculated with the method outlined in Equations 5.1-5.3 above. Values calculated for Airdrie were added as additional observations to the tomographic adjustment through the augmentation of the observation (**z**) and observation covariance (**R**) matrices as such:

$$\mathbf{z} = \begin{bmatrix} l_1 \\ \mathbb{M} \\ l_n \\ l_{n+1} \\ \mathbb{M} \\ l_{n+m} \end{bmatrix} \tag{5.4}$$

where

n is the number of SWD observations at this epoch

m is the number of radiosonde N_W observations at this epoch and

l represents an individual observation

$$\mathbf{R} = \begin{bmatrix} s_1^2 & & & & & & \\ & \mathbf{O} & & & & & \\ & & s_n^2 & & & & \\ & & & s_{n+1}^2 & & & \\ & & & & \mathbf{O} & & \\ & & & & & s_{n+m}^2 \end{bmatrix} \tag{5.5}$$

where s is the standard deviation associated with a particular observation and the off-diagonal elements of this matrix are assumed to be zeros, implying no cross correlation of the .

Variances associated with the RS observations of N_W (terms $s_{n+1}^2 \ldots s_{n+m}^2$ in Equation 5.5) were calculated using the laws of error propagation, and from RS observation accuracies quoted by the manufacturer [*Vaisala*, 2004]. The observation accuracies for the RS observation were set as the Vaisala RS80 resolution [*Vaisala*, 2004], which is slightly better than the accuracy measurements given by the manufacturer. This was done so that the RS measurement is given a weighting during the tomographic adjustment that was high compared to the GPS measurement, since radiosondes are ***in situ*** measurements and considered to be very accurate [*Vaisala*, 2004].

Since the variables are a function of each other, their relationship can be represented as

$$\begin{aligned} es &= f(T) \\ e &= f(es, RH) \\ N_W &= f(e, T) \end{aligned} \tag{5.6}$$

If the equation for *es* is simplified then the following is derived:

$$\log_{10}(es) = \underbrace{\frac{-2937.4}{T} - 4.9283\log_{10} T + 23.5470}_{=x} \tag{5.7}$$

$$es = 10^{x}$$

Using the laws of error propagation for a quantity which is a function of measured quantities which have a variance associated with them [*Bevington*, 1992]

$$s_{es}^{2} \cong s_{T}^{2}\left(\frac{des}{dT}\right)^{2} \tag{5.8}$$

where

$$\frac{des}{dT} = x \times 10^{(x-1)}\frac{dx}{dT} \tag{5.9}$$

It follows that the variance equation for *e* is

$$s_{e}^{2} \cong s_{RH}^{2}\left(\frac{de}{dRH}\right)^{2} + s_{es}^{2}\left(\frac{de}{des}\right)^{2} \tag{5.10}$$

where

$$\frac{de}{dRH} = \frac{es}{100}$$
$$\frac{de}{des} = \frac{RH}{100} \tag{5.11}$$

and finally the variance equation for N_W is

$$s^2_{N_W} \cong s^2_e \left(\frac{dN_W}{de} \right)^2 + s^2_T \left(\frac{dN_W}{dT} \right)^2 \tag{5.12}$$

where

$$\frac{dN_W}{de} = \frac{3.73 \times 10^5}{T^2}$$
$$\frac{dN_W}{dT} = \frac{(-2)(3.73 \times 10^5)(e)}{T^3} \tag{5.13}$$

These new observations add rows to the design matrix **H**. Since these new observations happen at a particular spatial location within the SAN, their location is specified in the design matrix by their respective Dj and Dl from the expansion point. Using the form of the design matrix outlined in Chapter 3, the additional layers of the design matrix will be

$$\begin{matrix} & \textit{layers} & & & & \textit{gradients} & & & \\ \mathbf{H} = \begin{bmatrix} 1 & 0 & \mathbf{L} & 0 & \Delta j & \Delta j^2 & \Delta l & \Delta l^2 \mathbf{L} \\ 0 & 1 & \mathbf{L} & 0 & \mathbf{L} & & & \\ \mathbb{M} & & \mathbf{O} & & & & & \\ 0 & \mathbf{L} & & 1 & \mathbf{L} & & & \end{bmatrix} \end{matrix} \tag{5.14}$$

5.3 Data Assimilation for the Climatological Model

The variance of this measurement is much larger than those found for single radiosonde or RS measurements, particularly for the lower layers of the model where temperature and relative humidity are highly variable over a month.

Examples of a single sounding from Airdrie, Alberta and the monthly averaged climate information from Stony Plain for July 2003 are given in Figure 5.3.

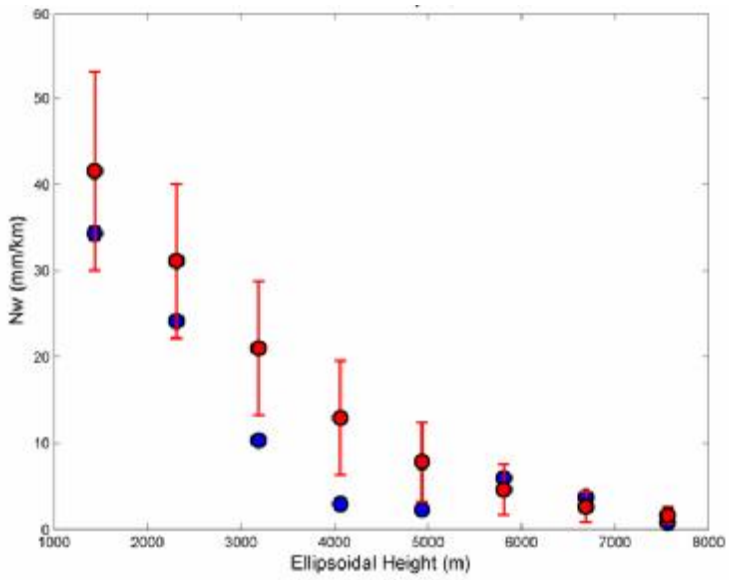

Figure 5.3. Single radiosonde observations of wet refractivity from Airdrie (blue - error bars negligible), and a climatological model made from the corresponding month's Stony Plain radiosonde observations (red).

The variability over one month makes for an increase in the uncertainty used for wet refractivity for the climatological model (larger error bars) when compared to the single radiosonde observations. This variability in the climatological model is especially prominent in the lowers layers where water vapour is notoriously variable. Assimilating the monthly average profile into a ground-based tomography approach should essentially add a constraint for wet refractivity values for the upper layers of the model only.

Although the lower layers give highly uncertain information to the adjustment when compared to the higher layers, they were included in the adjustment since as long as they are weighted properly they may add some valuable additional vertical information to the adjustment.

5.3.1 Mathematical Description of the Assimilation of the Climate Model

Given that the climate model was an average over a month, when assimilated it was assumed to be valid at every epoch during the month for which it was derived. For the assimilation of climatological model information from Stony Plain, wet refractivity measurements were derived using Equations 5.1-5.3 for July 2003 from monthly averaged measurements as processed by MSC. The result was a wet refractivity measurement for each layer of the tomography model that was used as input observations, or constraints.

For the inclusion of these measurements it was necessary to specify that these were valid across the entire SAN and not just at one location as the single RS measurements were characterized in Section 5.1. To achieve this, pseudo-observations were given for the higher order terms in the adjustment (i.e. those given with Dj and/or Dl in their coefficients). These particular coefficients are underlined in Equation 5.15 below, which is the reiteration of Equation 3.11, the fundamental observation equation for the tomography model.

$$SWD = \sum_{i=1}^{n} (a_{0i} + \underline{a_{1i}\Delta j} + \underline{a_{2i}\Delta j^{2}} + \underline{a_{3i}\Delta l} + \underline{a_{4i}\Delta l^{2}} + \underline{a_{5i}\Delta j \Delta l})dh_i \tag{5.15}$$

These terms are herein called gradient terms or gradient observations since they represent the horizontal gradient in each layer of the tomography model.

To determine the magnitude of the gradient pseudo-observations, magnitudes of the gradient terms during the tomographic adjustment using ground-based GPS SWD observations over several days during A-GAME 2003 were examined. During a process of trial and error using pseudo gradient observations which were made to be smaller than the observed nominal gradients, the maximum nominal gradient magnitude (0.2 mm/km) was reduced by a factor of ~10 to give a value of 0.01 mm/km and this was found to give reasonable results. It is recommended that for future work with this type of measurement, that gradients are examined for the specific time period of interest since gradients determined here were specific to the A-GAME 2003 campaign.

Additions made to the observation matrix during climatological model assimilation were as such:

$$\mathbf{z} = \begin{bmatrix} l_1 \\ \mathbb{M} \\ l_n \\ l_{n+1} \\ \mathbb{M} \\ l_{n+m} \\ l_{n+m+1} \\ \mathbb{M} \\ l_{n+m+p} \end{bmatrix} \tag{5.16}$$

where

n is the number of SWD observations at this epoch

m is the number of climate model N_W observations at this epoch

p is the number of pseudo gradient observations being added at this epoch and

l represents an individual observation

$$\mathbf{R} = \begin{bmatrix} s_1^2 & & & & & & & & \\ & \mathbf{O} & & & & & & & \\ & & s_n^2 & & & & & & \\ & & & s_{n+1}^2 & & & & & \\ & & & & \mathbf{O} & & & & \\ & & & & & s_{n+m}^2 & & & \\ & & & & & & s_{n+m+1}^2 & & \\ & & & & & & & \mathbf{O} & \\ & & & & & & & & s_{n+m+p}^2 \end{bmatrix} \tag{5.17}$$

where s is the standard deviation associated with a particular observation and the off-diagonal elements of this matrix are assumed to be zeros, implying no cross correlation between observations.

Standard deviations for the pseudo gradient observations of 0.5 mm/km were used in this work. This value was derived much like the gradient magnitudes themselves; they were determined from studies of nominal values for several days of tomographic adjustments using GPS SWD observations, as well as some trial and error during adjustment runs with the climate model assimilated.

Additional rows to the design matrix from the addition of this new observation had the form:

$$\mathbf{H} = \begin{array}{c} \begin{matrix} \textit{layers} & & & \textit{gradients} & \end{matrix} \\ \begin{bmatrix} 1 & 0 & 0 & \mathbf{L} & 0 \\ 0 & 1 & 0 & \mathbf{L} & 0 \\ \mathbf{M} & & \mathbf{O} & & \mathbf{M} \\ \mathbf{M} & & & \mathbf{O} & \\ \mathbf{M} & & & \mathbf{O} & \\ 0 & 0 & \mathbf{L} & & 1 \end{bmatrix} \end{array} \tag{5.18}$$

5.4 Data Assimilation for Occultation Observations

Total refractivity measures obtained from CHAMP occultations were used for September 1, 2003. These measurements are unique from either the radiosonde observations made at Airdrie, or the climate model information from Stony Plain, as they represent an average measurement spatially, but are taken over a very short time scale.

September 1, 2003 was chosen for occultation processing due to the CHAMP occultation being located within the SAN and also located in the GEM model space provided from MSC. Two hour and eight-hour time spans are processed from 01:45 UTC, as the occultation measurement was time-tagged at 01:47:41 UTC. The occultation profile is assimilated throughout the entire processing time.

To determine the observation variance on the occultation measurements, values used by the European Centre for Medium-Range Weather Forecasts (ECMWF) for the assimilation of GPS occultation measurements into their forecast models were taken into consideration. Below 10 km, ECMWF uses a variance value of 3% of the total refractivity derived by GPS occultations as the error. This number is also supported by work done by ***Kuo et al***. [2004]. After consulting with Craig Smith from MSC [***Smith***, 2004b] and Geoff Strong [***Strong***, 2004], an Alberta meteorologist, it was concluded that GEM data accuracies were not available with sufficient accuracy to derive estimates of

the accuracy of wet refractivity in the same manner as they were for radiosonde measurements. Since the occultation observation of wet refractivity used in this study was derived from GEM measurements as well, which have errors associated with them, the variance of 3% total refractivity was increased to a variance of 5% of the total refractivity. This was used through out occultation assimilation as a measurement accuracy estimate for the wet refractivity derived from the occultation and GEM data.

The Stony Plain radiosonde measurements (abbreviated AveRS) profile for September 2003 is plotted along with the occultation measurement from September 1, 2003 in Figure 5.4.

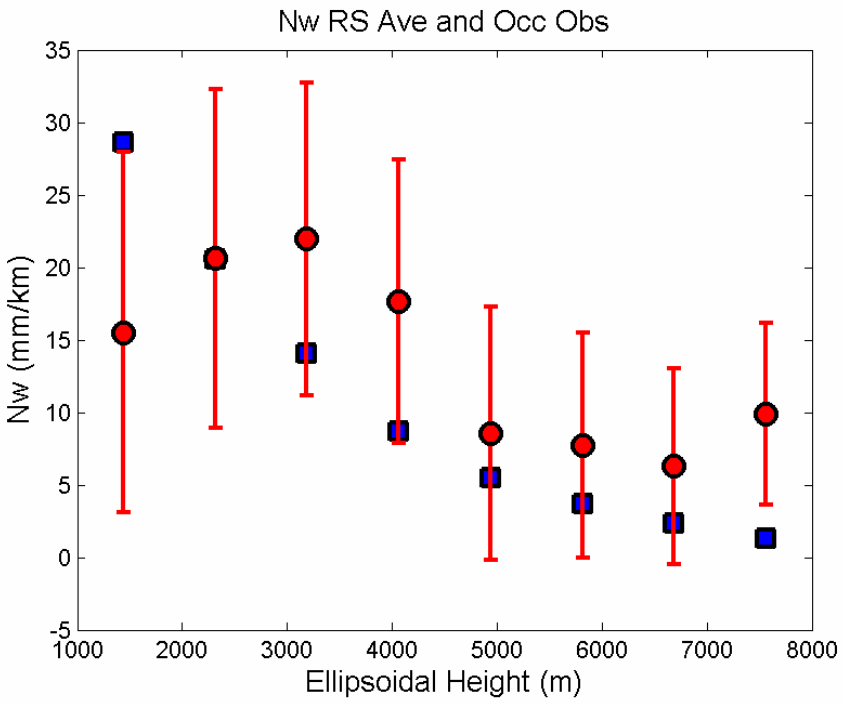

Figure 5.4. Vertical N_W profile of AveRs for Sept 2003 (blue squares) and occultation (red circles) assimilated on Sept 1, 2003.

The AveRS is plotted here for comparison purposes, to show an additional source of a wet refractivity profile which is valid for this month, and does not show error bars (for an

example of AveRS error measurement bars, see Figure 5.3). The occultation profile shows an inversion occurring in the lowest layer of the tomography model. However, the occultation measurement is notoriously weak below 2 km, and this may or may not be a real characteristic of the atmosphere at this point in time.

5.4.1 Derivation of N_W Measurements

Measurements of total refractivity were derived from the CTss method for CHAMP GPS occultations as described in Section 4.4. The total refractivity measurements were then averaged in the same layers that were being used in the tomography model.

Temperature and pressure profiles at the point closest to the occultation were then derived from GEM data. This GEM data point was found to be at N52.20° latitude and W111.62° longitude. The GEM data point does not exactly match the occultation location; however, since the occultation measurement is made from an average over several hundred kilometres of the atmosphere, this is assumed to be adequate. GEM data is given for pressure levels, and this needed to be converted to ellipsoidal height. As an intermediate step, pressure levels were converted to orthometric heights using an equation from the Portland State Aerospace Society (PSAS) web page [*PSAS Web Site*, 2004], as suggested by Craig Smith from MSC [*Smith*, 2004a].

$$ortho = 44332.3 - (4947.2 \times P^{0.190255}) \tag{5.19}$$

where

ortho is the orthometric height, or altitude in metres above sea level and

P is the level pressure in Pascals.

The orthometric height was then converted to WGS-84 height using the GPS.H program from NRCan. Once averaged for the tomography layers, pressure and temperature measurements were used to derive hydrostatic refractivity from Equation 2.8:

$$N_H = 77.6\frac{P}{T} \tag{5.20}$$

The wet refractivity was then calculated from the total refractivity found from the occultation measurement minus the hydrostatic refractivity found from the GEM data.

Occultation measurements are an average spatial representation of the atmosphere that the signal travels through while making an observation (see Section 3.5.3 for details). This distance can be hundreds of kilometres, and therefore, this type of observation was considered to give the same spatial information to the SAN as the climatological model. Pseudo gradient observations and associated standard deviations were added to the adjustment when the occultations were assimilated into the tomography adjustment, of the same magnitude and uncertainty as those mentioned in Section 5.3.1 for the inclusion of climatological measurements. This was to specify that the occultation measurements were valid across the whole SAN. As before, it is recommended that for future work with this type of measurement, that gradients are examined for the specific time period of interest since gradients utilized here were determined from July A-GAME 2003 campaign data.

Additions made to the observation matrix during occultation assimilation were as such:

$$\mathbf{z} = \begin{bmatrix} l_1 \\ \mathbb{M} \\ l_n \\ l_{n+1} \\ \mathbb{M} \\ l_{n+m} \\ l_{n+m+1} \\ \mathbb{M} \\ l_{n+m+p} \end{bmatrix} \tag{5.21}$$

where

n is the number of SWD observations at this epoch

m is the number of occultation-derived N_W observations at this epoch

p is the number of pseudo gradient observations being added at this epoch and

l represents an individual observation.

$$\mathbf{R} = \begin{bmatrix} s_1^2 & & & & & & & \\ & \mathbf{O} & & & & & & \\ & & s_n^2 & & & & & \\ & & & s_{n+1}^2 & & & & \\ & & & & \mathbf{O} & & & \\ & & & & & s_{n+m}^2 & & \\ & & & & & & s_{n+m+1}^2 & \\ & & & & & & & \mathbf{O} \\ & & & & & & & & s_{n+m+p}^2 \end{bmatrix} \tag{5.22}$$

where s is the standard deviation associated with a particular observation and the off-diagonal elements of this matrix are assumed to be zeros.

Standard deviations for the pseudo gradient observations of 0.5 mm/km were used in this work, as described in Section 5.3.1.

Additional rows to the design matrix from the addition of the occultation observations had the form

$$\mathbf{H} = \begin{array}{c} \begin{matrix} \textit{layers} & & & \textit{gradients} & \end{matrix} \\ \begin{bmatrix} 1 & 0 & 0 & \mathbf{L} & 0 \\ 0 & 1 & 0 & \mathbf{L} & 0 \\ \mathbb{M} & & \mathbf{O} & & \mathbb{M} \\ \mathbb{M} & & & \mathbf{O} & \\ \mathbb{M} & & & \mathbf{O} & \\ 0 & 0 & \mathbf{L} & & 1 \end{bmatrix} \end{array} \tag{5.23}$$

CHAPTER 6

RESULTS AND ANALYSIS

Results are presented in this chapter for the assimilation of radiosonde observations, climate data, and GPS occultation observations into the tomography model. Various testing conditions are used to determine the optimal way to assimilate each observation. Accuracy measures are determined using a radiosonde truth integrated profile of zenith wet delay, and vertical profiles of wet refractivity are also examined for certain epochs. Improvements are sought in the integrated (ZWD) domain with respect to the tomographic solution using ground-based GPS data alone. Two quiet days (July 19 and 25) were examined for the accuracies obtainable with the different tomographic methods used with radiosonde and climate data assimilated, and also two storm days (July 20 and 26) were examined. GPS occultation assimilation is tested for September 1, 2003.

6.1 Overview of Data

Data from SAN stations was processed with Bernese for batched hourly zenith total delay (ZTD) at each station. After the data was processed in the tomography solution, the hourly batched nature of the GPS SWD solution became apparent as jumps that occurred every 60 minutes. July 19, 2003 was processed twice with 60-minute and 30-minute batch intervals to determine if these jumps would be removed with a different batch time. ZTD at Calgary for this day are plotted in Figure 6.1.

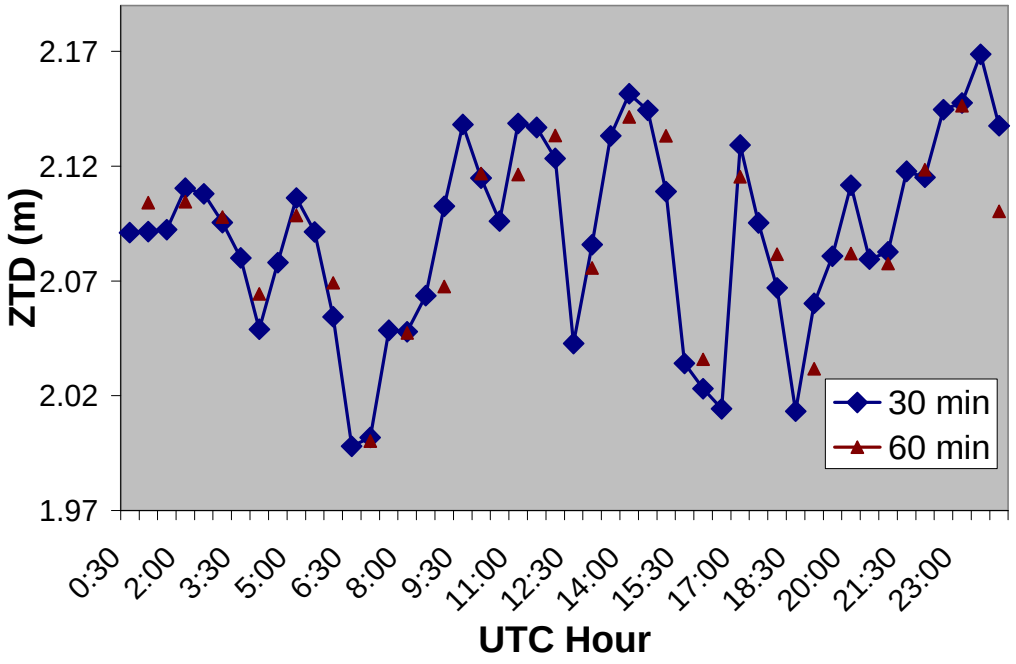

Figure 6.1. ZTD Bernese solutions for Calgary on July 19, 2003 using 30-minute and 60-minute batch intervals.

Changing the batch interval from 30 to 60 minutes sometimes results in 30-minute estimates that vary smoothly between 60-minute estimates (as can be seen around 4:00 in Figure 6.1), and sometimes the two 30-minute estimates for a particular 60-minute time span are both very close in magnitude to the 60-minute estimate (around 8:00 in Figure 6.1). In general, the 30-minute solution does not very greatly from the 60-minute solution, although there are some 30-minute data points that would not be resolved from simply smoothing between 60-minute data points, such as the point shown at 13:00. Discontinuities in the solutions for ZTD seem to due to the Bernese estimation process and not always a consequence of batch interval.

Data was processed with the tomography solution for two days where storms could be discerned by radar and confirmed by A-GAME participants, and two days where no such activity occurred. Radiosondes released at Olds/Didsbury Airport are examined for these days as well (labelled “truth” in plots) for an hour after their launch. There is a maximum

of three radiosondes released at this site in a day, thus making times sparse where comparisons can be made to the tomography solution for the Olds/Didsbury Airport. The first day examined is July 19, 2003 in Figure 6.2, which is considered to be a quiet day for solutions obtained at the Olds/Didsbury Airport.

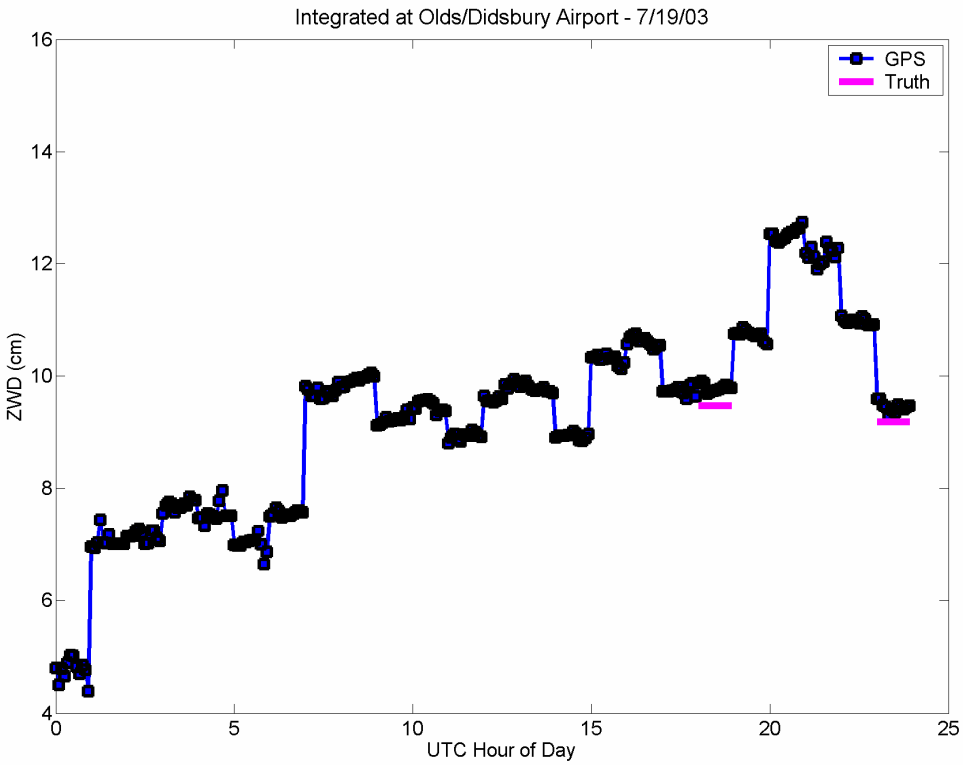

Figure 6.2. July 19, 2003 tomography and truth radiosonde solution for ZWD.

Figure 6.2 shows a solution which has discontinuities related to the Bernese hourly estimates. The radiosonde truth solution matches the tomography solution closely for the hours when it is plotted. The rise in ZWD for the tomography solution between the truth measurements cannot be verified from the truth solution, due to its sparse temporal nature. There is a gradual rise throughout this day of ZWD at this location.

This quiet day is followed by a storm day, July 20, 2003. On this day a large storm cell passed through the SAN, travelling from the northwest corner of the network to the southeast corner of the network. The formation of this storm was filmed by A-GAME collaborator Geoff Strong near Limestone Mountain (Figure 6.3).

Figure 6.3. Picture of the July 20, 2003 cell near Limestone Mountain at ~1500 local time [courtesy of Geoff Strong].

This storm was also tracked by Weather Modification Incorporated's (WMI) TITAN radar. Figure 6.4 gives the maximum reflectivity values found for the SAN area on July 20, 2003. A scale of the colours representing these reflectivities is given on the right hand side of the image; the higher the colours in the image, the higher the reflectivity value. Reflectivity is given in dBZ, which is a unitless representation of a logarithmic power radio (in decibels) with respect to a radar reflectivity factor *Z*. An outline of the city of Calgary can be seen in this image in the middle of the lower half of the image, and Red Deer can be seen in the middle in the top half of the image. False reflections are always visible from the mountains and larger foothills at the lower left-hand side of the TITAN radar images.

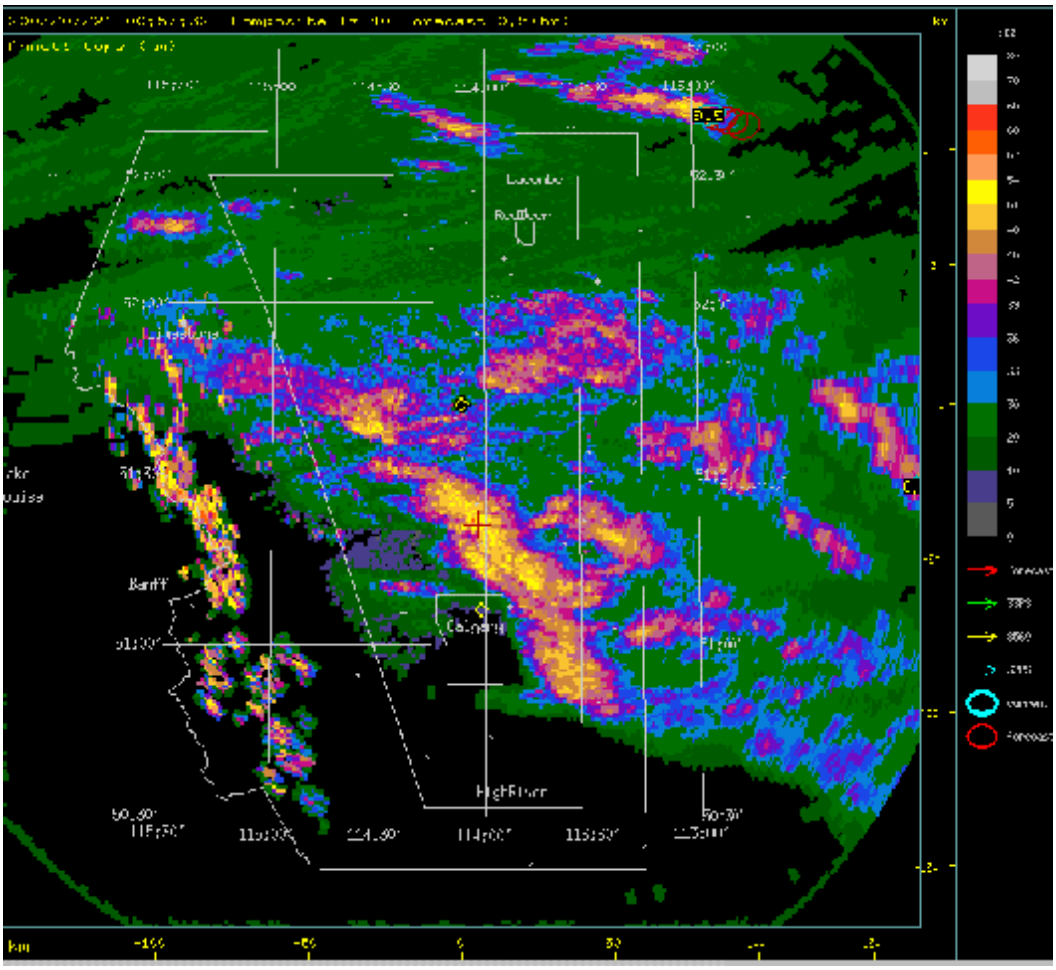

Figure 6.4. TITAN radar image of the max reflectivity over July 20, 2003 [courtesy of WMI and The Alberta Severe Weather Management Society].

In Figure 6.4, the Olds/Didsbury Airport is seen as a small yellow diamond north of the city of Calgary. As can be seen in this figure, the main cell of the storm misses the location where results are being examined.

The full-day tomographic solution is shown in Figure 6.5 for July 20, 2003.

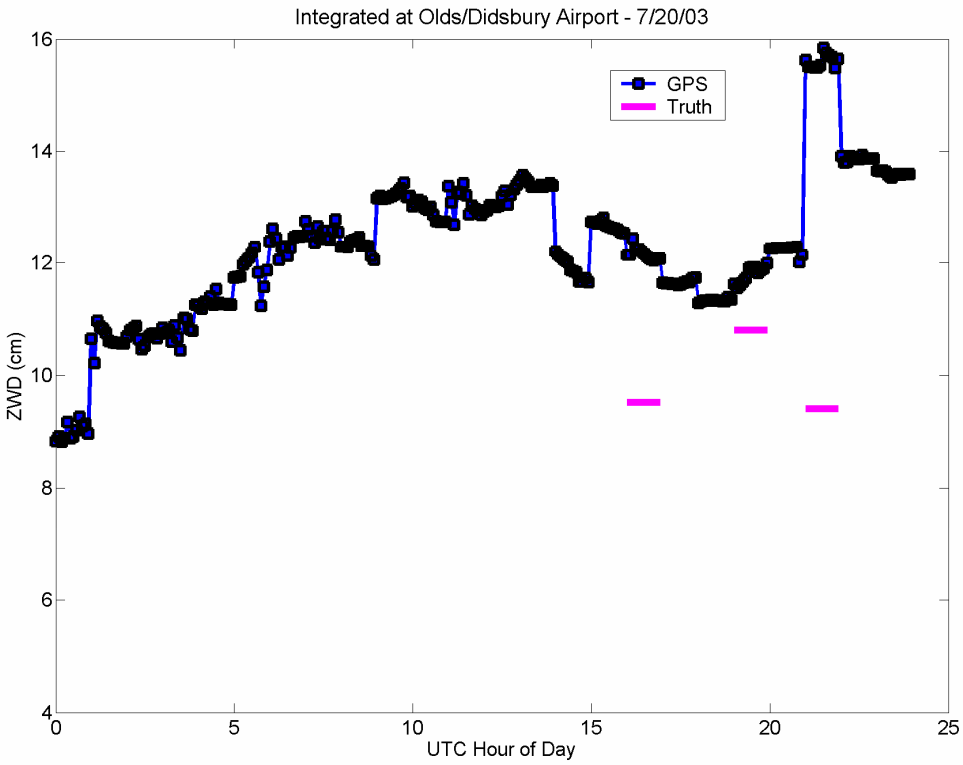

Figure 6.5. July 20, 2003 tomography and truth radiosonde solution for ZWD.

This day shows a few discontinuities in the tomographic GPS solution related to the Bernese hourly estimates of ZTD. The tomographic solution appears high when compared to the truth solution. The gradual rise in ZWD continues from July 19, 2003 until approximately 10:00 where a decrease in ZWD begins to occur. The large jump at ~21:30 appears to be a poor Berenese ZWD estimate, given the truth solution for this time and the hour-long nature of the jump. It is interesting to note however, that the large cells of this storm was active around 22:00 on this day in the vicinity of the Olds/Didsbury Airport [*Hoyle*, 2003], when this discontinuity is evident. Also, the July 20, 2003 storm became active after a rise in ZWD seen at this station over July 19th and 20th.

The next day of data used for analysis was July 25, 2003. This was considered to be a meteorologically calm day.

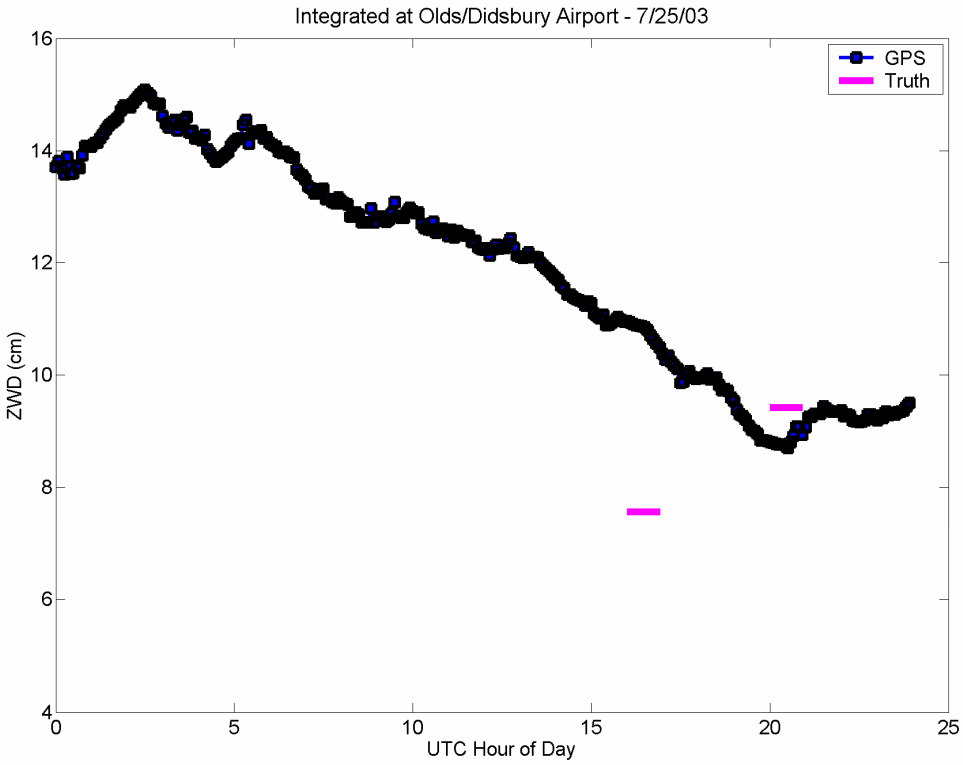

Figure 6.6. July 25, 2003 tomography and truth radiosonde solution for ZWD.

This day's tomographic solution with GPS only as input (Figure 6.6) does not show the discontinuities from the Bernese ZTD solution. The tomography solution matches the truth solution at 21:00, but not at 17:00. A decreasing trend of ZWD can be seen throughout this day. This day is followed by another storm day which was used for analysis; July 26, 2003.

On July 26, 2003, a large storm passed through the SAN. Significant hail was reported by A-GAME participants in the Olds/Didsbury region (shown in Figure 6.7). Figure 6.8

is a TITAN radar image of the max reflectivity observed by Weather Modification Inc. on this day over southern Alberta.

Figure 6.7. Picture of hailstorm taken at ~1900 local time at Olds/Didsbury airport [courtesy of Geoff Strong].

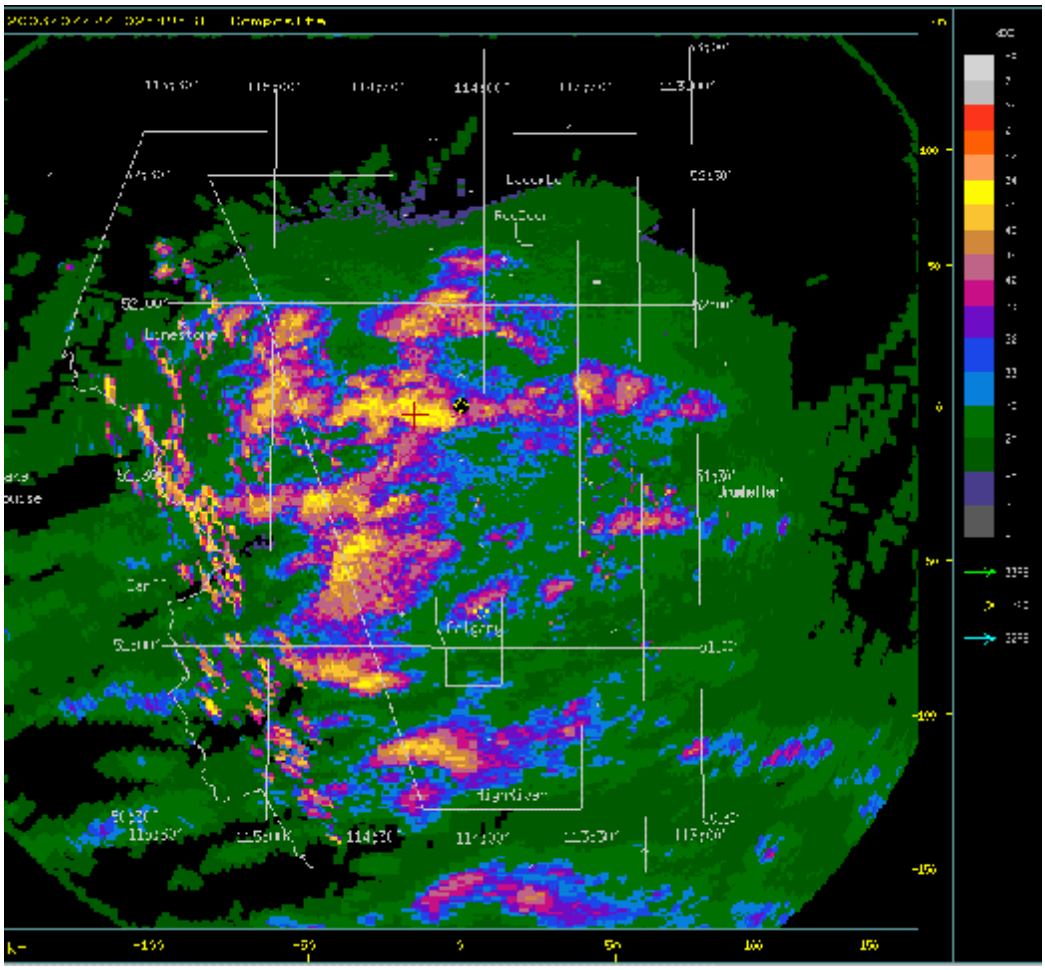

Figure 6.8. TITAN radar image of the max reflectivity over July 26, 2003 [courtesy of WMI and The Alberta Severe Weather Management Society].

The full-day tomographic solution for July 26, 2003 is shown below.

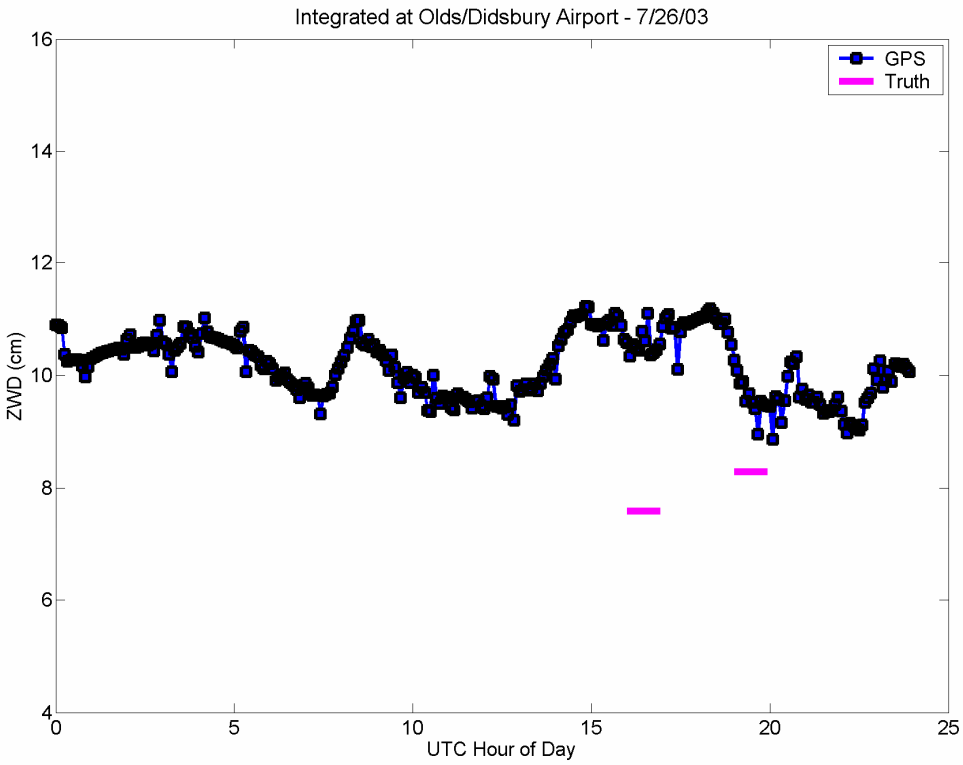

Figure 6.9. July 26, 2003 tomography and truth radiosonde solution for ZWD.

The tomographic solution for ZWD stays at a constant level throughout this day (Figure 6.9) and shows short term variations, indicating short-term dynamics in the water vapour for this location on this day. The effects of this storm were seen at the Olds/Didsbury Airport (Figure 6.7) at the very end of the UTC day. Leading up to this time, the tomographic solution (Figure 6.9) does not show a sharp incline or decline in ZWD. However, this day does show fluctuations throughout the day in ZWD which may be indicative of atmospheric turbulence related to the generation of the storm.

6.2 Assimilation of Radiosonde Observations

There were three different types of processing performed for each day of data analysed. This processing is labelled on plots in this chapter as such: GPS, GPS + RS and GPS + AveRS. Truth values are derived from Olds/Didsbury radiosonde measurements, and are

used to derive accuracy estimates for the estimation schemes tested. The RMS of the difference between truth and the solution generated from tomography at every epoch that a solution is generated is presented as a measure of accuracy. The mean of the difference between the tomography solution and truth is also presented. The maximum is also taken of the difference between the model and truth to show points where the solutions are most different in magnitude from the truth solution, and the minimum of the difference is also shown.

Integrated plots of zenith wet delays (ZWD) are found from integrating through the estimated wet refractivity field from the solutions from the tomography model, as outlined in Section 3.4.1 and Equation 3.13. This equation is used to integrate through the part of the model that lies directly above the Olds/Didsbury Airport radiosonde launch location so that solutions can be compared to ZWD derived from the truth (Olds/Didsbury Airport) radiosondes.

Testing is conducted using data from the hour after the radiosonde launch at Airdrie ("RS") for analysis, since the radiosonde measurement is most representative of the actual atmospheric conditions for times closest to the launch time. The radiosonde profile from Olds/Didsbury that is closest to the Airdrie radiosonde launch time is used as the truth. Days and times were chosen when these two radiosonde measurements occurred as close together as possible for a better comparison:

- July 19, 2003 – same time
- July 20, 2003 – one hour apart
- July 25, 2003 – one hour apart
- July 26, 2003 – two hours apart

Unless otherwise stated, all times given in this chapter are in UTC.

6.2.1 Quiet Days

July 19 and 25, 2003 did not see any significant storms pass through the SAN of GPS receivers. This was verified by confirming with A-GAME collaborators the amount of activity seen on these days and also searching the *National Climate Data and Information Archive* [2004] to see if any significant meteorological events happened on these days within the SAN.

6.2.1.1 July 19, 2003

The results for GPS + RS best match the truth in both the integrated ZWD (Figure 6.10) and vertical N_W (Figure 6.11) plots. Accuracies of 0.3 cm are achieved for the model ZWD values in this case when compared to the truth values from Olds/Didsbury radiosonde.

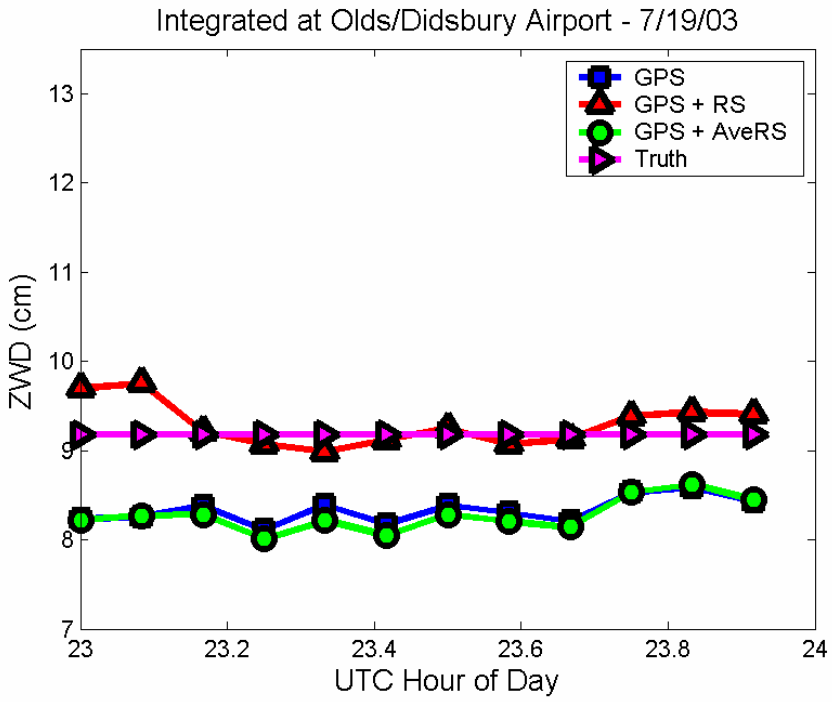

Figure 6.10. Integrated ZWD solutions at Olds/Didsbury airport for July 19, 2003.

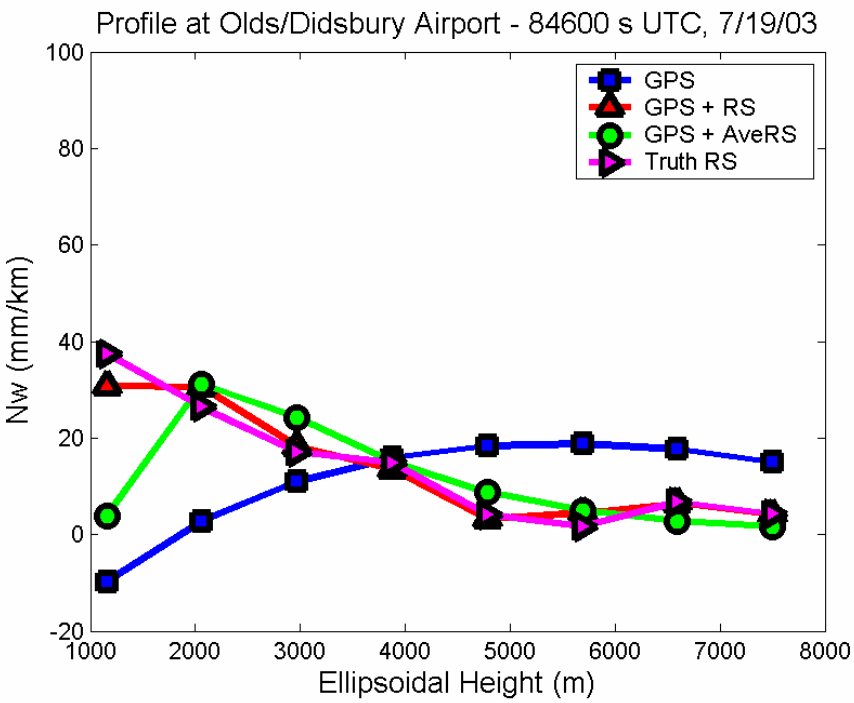

Figure 6.11. Vertical N_W profile at Olds/Didsbury airport July 19, 2003, 23:30 UTC (midpoint of Figure 6.10).

Adding the AveRS profile to the GPS tomographic solution makes no improvement over the GPS-only solution in the integrated domain (Figure 6.10), but does change the model vertical profile (Figure 6.11) so that it generally better matches the truth. The profile given by the GPS only solution does not give a reasonable vertical profile as negative N_W values are a physical impossibility. The GPS + AveRS profile's N_W value in the lowest layer significantly deviates from the truth and converges towards the GPS-only solution at this point. This occurs because the lowest layer's variance over one month is large for the AveRS N_W (see Figure 5.3), which in turn defines a lower weight for the AveRS information at this altitude in the overall GPS + AveRS solution. When comparing to truth, the GPS and GPS + AveRS ZWD results are very similar, even though N_W profiles for each result differ. This is due to the non-uniqueness of the problem, in which the same integrated value may be derived from any number of different N_W profiles.

6.2.1.2 July 25, 2003

Integrated ZWD results for July 25 show the GPS + RS solution to be just over 1 cm larger than the truth solution, while the GPS and GPS + AveRS solutions are similar and have errors around 2 cm (Figure 6.12).

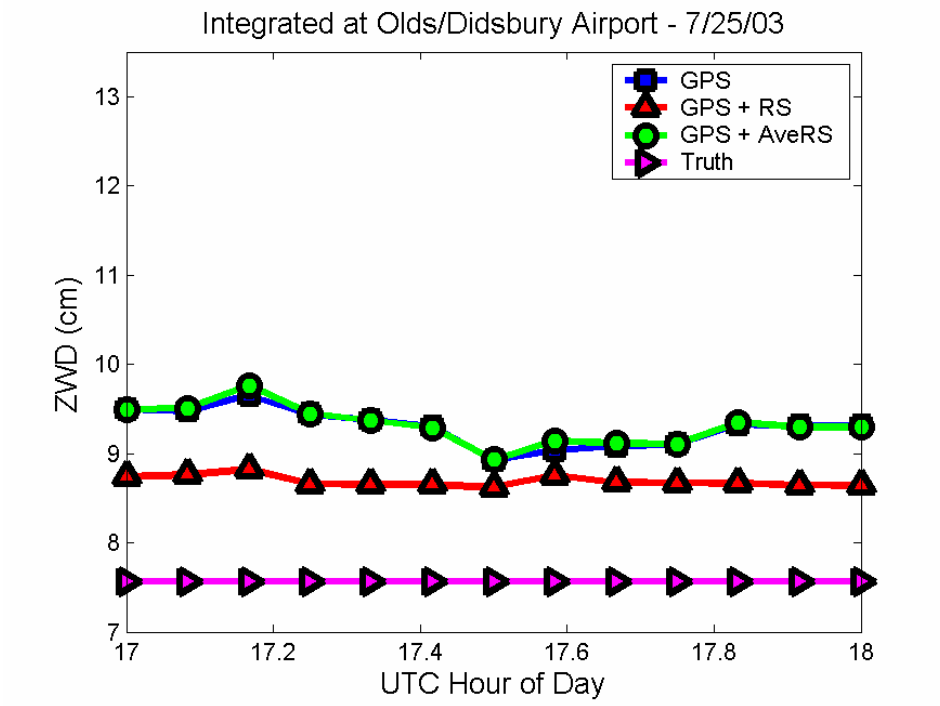

Figure 6.12. Integrated ZWD solutions at Olds/Didsbury airport for July 25, 2003.

The GPS N_W profile for this day has a general shape that is more reasonable than for July 19; the general shape is what would be expected for the region normally, with water vapour dropping off exponentially. However it is too high in the lower layer and negative for the higher layers (Figure 6.13).

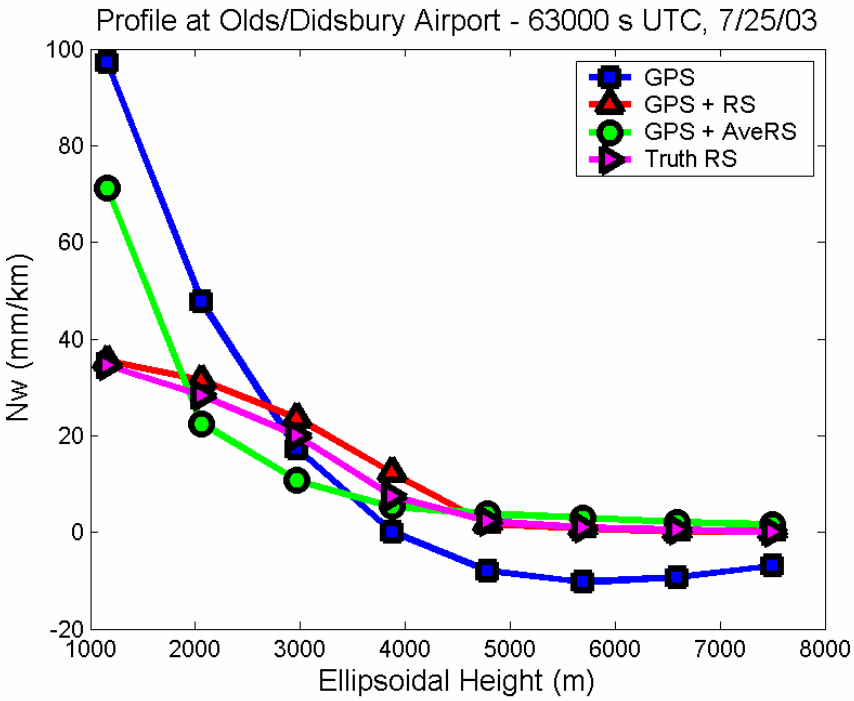

Figure 6.13. Vertical N_W profile at Olds/Didsbury airport July 25, 2003, 17:30 UTC (midpoint of Figure 6.12).

Adding the AveRS to the tomographic estimation creates profiles for this time period that are more physically realistic (i.e. not negative), but that once again converge significantly towards the GPS solution in the lower layer. A summary of solutions found for quiet days is given in Table 6.1.

6.2.1.3 Summary of Results

The GPS + RS solution is better than the GPS or GPS + AveRS solutions for the times compared by 0.6 cm for both quiet days. The integrated accuracies for the GPS and GPS + AveRS solutions are very similar in their RMS, mean, max and min. The difference in these two approaches can be seen in the vertical profiles that they give (Figures 6.11 and 6.13). Adding climate data to the GPS solution produces profiles that are more physically realistic, particularly for the upper layers of the atmosphere.

Table 6.1 Zenith Wet Delay Accuracies from Tomography Model during Times when Radiosonde Observations are Available on Quiet Days

Date	GPS	GPS + RS	GPS + AveRS
RMS (cm)			
July 19	0.9	0.3	0.9
July 25	1.7	1.1	1.8
Mean (cm)			
July 19	-0.8	0.1	-0.9
July 25	1.7	1.1	1.8
Max (cm)			
July 19	-0.6	0.6	-0.6
July 25	2.1	1.3	2.2
Min (cm)			
July 19	-1.1	-0.2	-1.2
July 25	1.4	1.1	1.4

6.2.2 Storm Days

The same analysis as was performed on quiet days was performed on two storm days during A-GAME 2003 campaign: July 19, 2003 and July 26, 2003. The times of analysis were restricted by the timing of the radiosonde launches, and thus, were not always analyzed through times when the storm cells were over the network. However, these tests were at noon or later in the day, and would most likely be a time when convection was occurring over the SAN for these storm days, or at least increased atmospheric dynamics were expected to be present.

6.2.2.1 July 20, 2003

The tomographic results for this day follow.

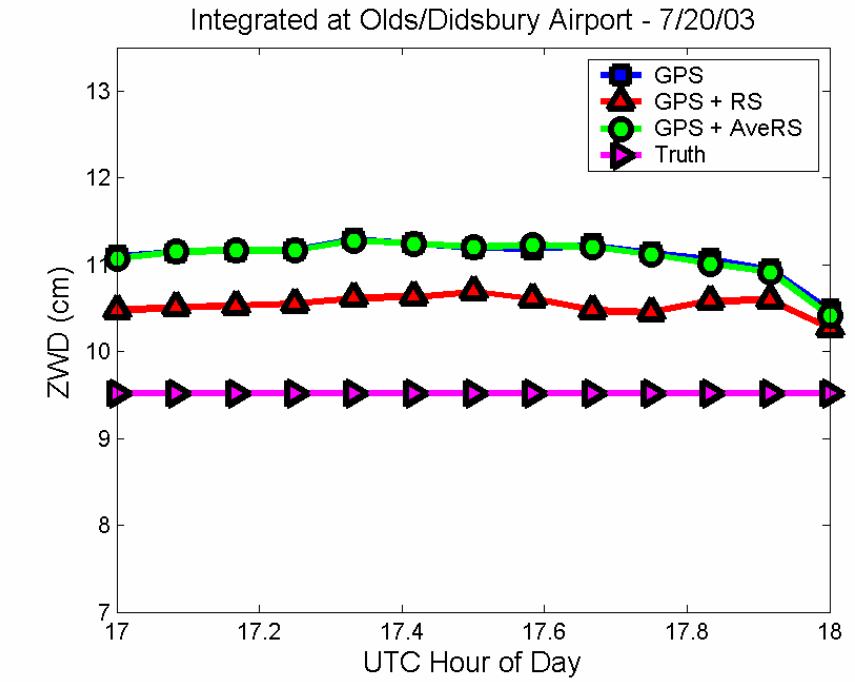

Figure 6.14. Integrated ZWD solutions at Olds/Didsbury airport for July 20, 2003.

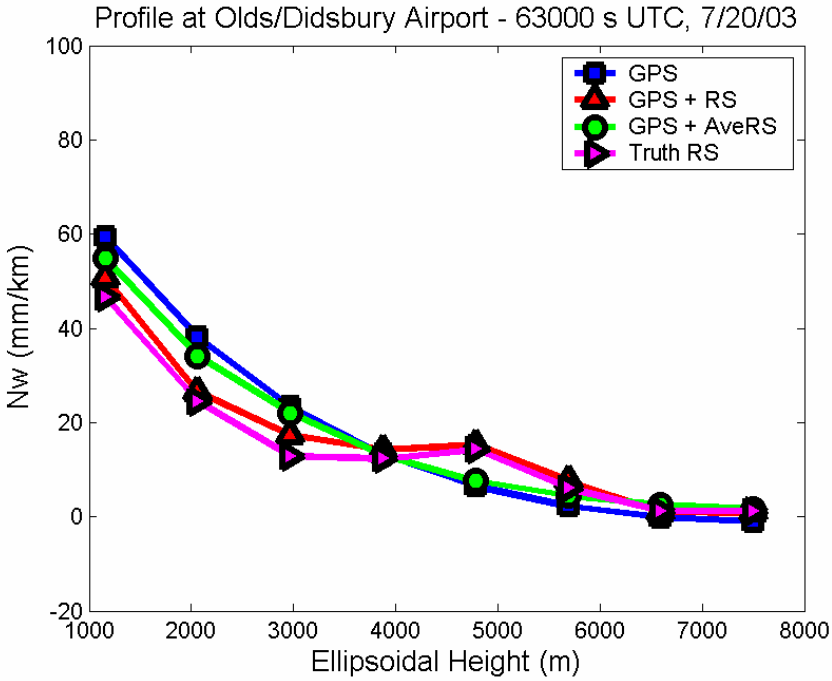

Figure 6.15. Vertical N_W profile at Olds/Didsbury airport July 20, 2003, 17:30 UTC (midpoint of Figure 6.14).

Figures 6.14 and 6.15 show the integrated ZWD values and N_W vertical profiles, respectively, for July 20, 2003. Integrated ZWD values show that the GPS + RS solution is closer to the truth solution (accuracy of ~1 cm from Figure 6.14) than the GPS or GPS + AveRS solution, which is consistent with results in Section 6.2.1 for the quiet days. Profiles for July 20, 2003 show small scale variation in the GPS + RS and truth vertical profiles. These features, which appear to be real, are smoothed through in the GPS and GPS + AveRS solutions. GPS and GPS + AveRS solutions have a higher error when compared with the truth integrated solution than the GPS + RS solution, except at the very end of the comparison time, when the GPS and GPS + AveRS solutions drop down to near the same values as the GPS + RS solution (Figure 6.14).

6.2.2.2 July 26, 2003

Tomographic results for July 26, 2003 follow.

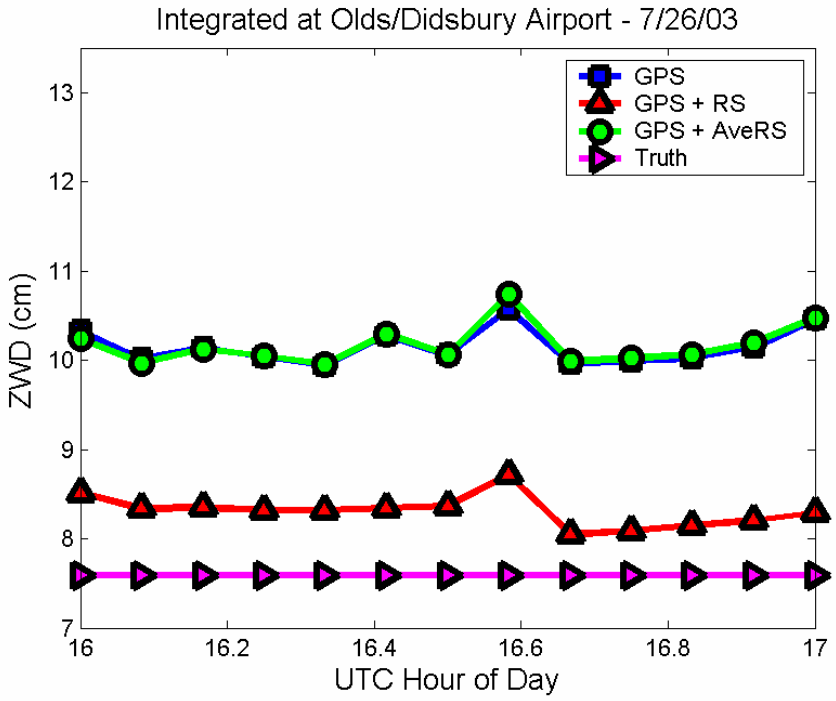

Figure 6.16. Integrated ZWD solutions at Olds/Didsbury airport for July 26, 2003.

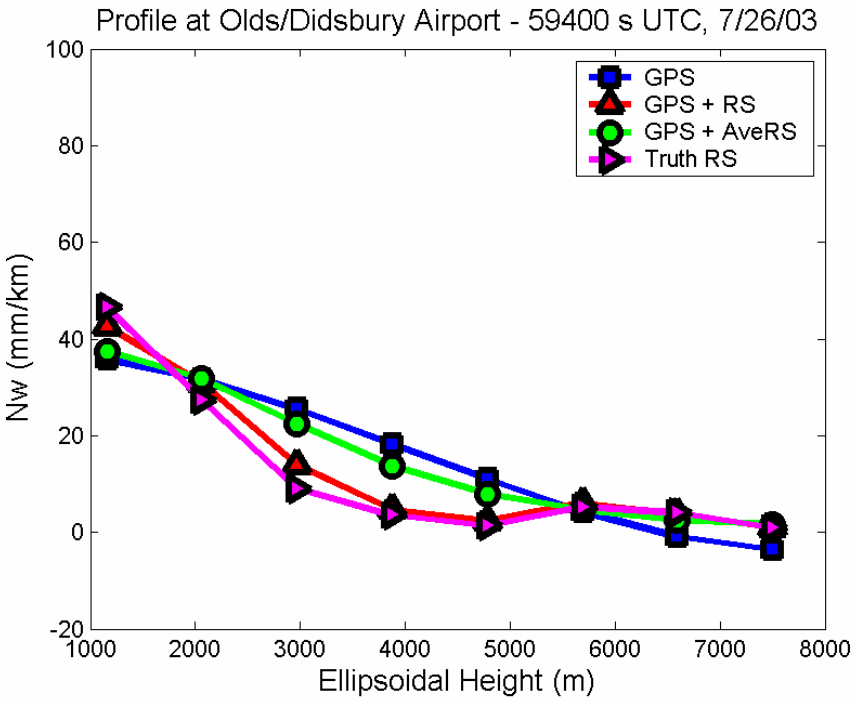

Figure 6.17. Vertical N_W profile at Olds/Didsbury airport July 26, 2003, 16:30 UTC (midpoint of Figure 6.16).

Figures 6.16 and 6.17 show the integrated ZWD values and N_W vertical profiles, respectively, for July 26, 2003. The ZWD plot shows the GPS + RS solution to be within about 1 cm of the truth solution, while the GPS and GPS + AveRS solutions are around 2 cm higher than truth. Again, ZWD results are improved the most by including the RS information in the tomography solution. The GPS N_W profile is flatter than the GPS + RS and GPS + AveRS N_W profiles, which follow the truth profile more closely. This smoothing over small variations was also seen in Section 6.2.2 for the other storm day analyzed, July 20, 2003. Table 6.2 summarizes the results for both storm days.

6.2.2.3 Summary of Results

On storm days examined, the GPS + RS solution was at least 0.5 cm better than the GPS or GPS + AveRS solutions, with the most marked improvement showing on July 26, 2003, when almost 2 cm improvement is made by using the GPS + RS solution versus the

GPS or GPS + AveRS solutions. GPS and GPS + AveRS solutions are virtually the same to the millimetre level, which was also the result from quiet days. This is because there is a very low weight associated with the AveRS measurements and so the adjustment resembles the GPS solution closely.

Table 6.2 Zenith Wet Delay Accuracies from Tomography Model during Times when Radiosonde Observations are Available on Storm Days

Date	GPS	GPS + RS	GPS + AveRS
RMS (cm)			
July 20	1.6	1.0	1.6
July 26	2.6	0.7	2.6
Mean (cm)			
July 20	1.6	1.0	1.6
July 26	2.6	0.7	2.6
Max (cm)			
July 20	1.8	1.2	1.8
July 26	3.0	1.1	3.1
Min (cm)			
July 20	1.0	0.8	0.9
July 26	2.3	0.5	2.4

In comparing the results from quiet and storm days (Table 6.1 and 6.2 respectively), there is not much difference between the results for storm and quiet days, indicating that increased atmospheric activity does not seem to affect the accuracy of the model, except in the case of July 26, 2003, where model accuracies are worse with GPS and GPS + AveRS than for other times analysed.

6.3 Long-Term Testing

Tests were conducted treating the Airdrie radiosonde and measurements as valid over the last eight hours instead of over just one hour. The last eight hours of the day (in UTC) were chosen as the long-term test period because this was the time of day when the most radiosondes were released, therefore increasing the number of radiosondes for

comparison. These tests were designed to determine if a radiosonde measurement would be a benefit to the tomography model over a longer period of time. Since the AveRS measurements taken at Stony Plain are considered to be valid over an entire month, they are also included in the long-term testing. Considering that radiosondes are normally released every 12 hours in the province of Alberta, treating the radiosonde measurements as valid over a longer period of time may allow these temporally sparse measurements to benefit the tomographic adjustment for a longer period of time, and during times when no additional constraints are available.

The danger in assuming the radiosonde measurements are valid over a longer period of time is that if there are changes in the atmosphere after the radiosonde launch such as storms or instabilities, particularly those occurring on a smaller scale, they will not be represented by the radiosonde measurements. In these situations the assimilation of radiosonde data with ground-based GPS measurements will provide a strong solution which will detect small-scale variation in the atmosphere.

When the radiosonde measurements were being treated as valid over eight hours, the first testing performed used the same measurement uncertainty over the entire interval from start to finish. The assimilation technique and measurement uncertainty derivation used is the same as described in Section 5.2.

Further testing was done while assuming the radiosonde measurement to be valid over the same eight hours as tested before, but with an age factor applied to the measurement uncertainty with increasing time from the radiosonde launch. To determine how the uncertainty should age with time, a study was made of all radiosonde observations made over the whole A-GAME 2003 campaign (Figure 6.18). Subsequent radiosondes launched at Airdrie and Olds/Didsbury airport are differenced from the very first radiosonde launched in the campaign at these sites, and the result is plotted for the eight layers being used in the tomographic adjustment.

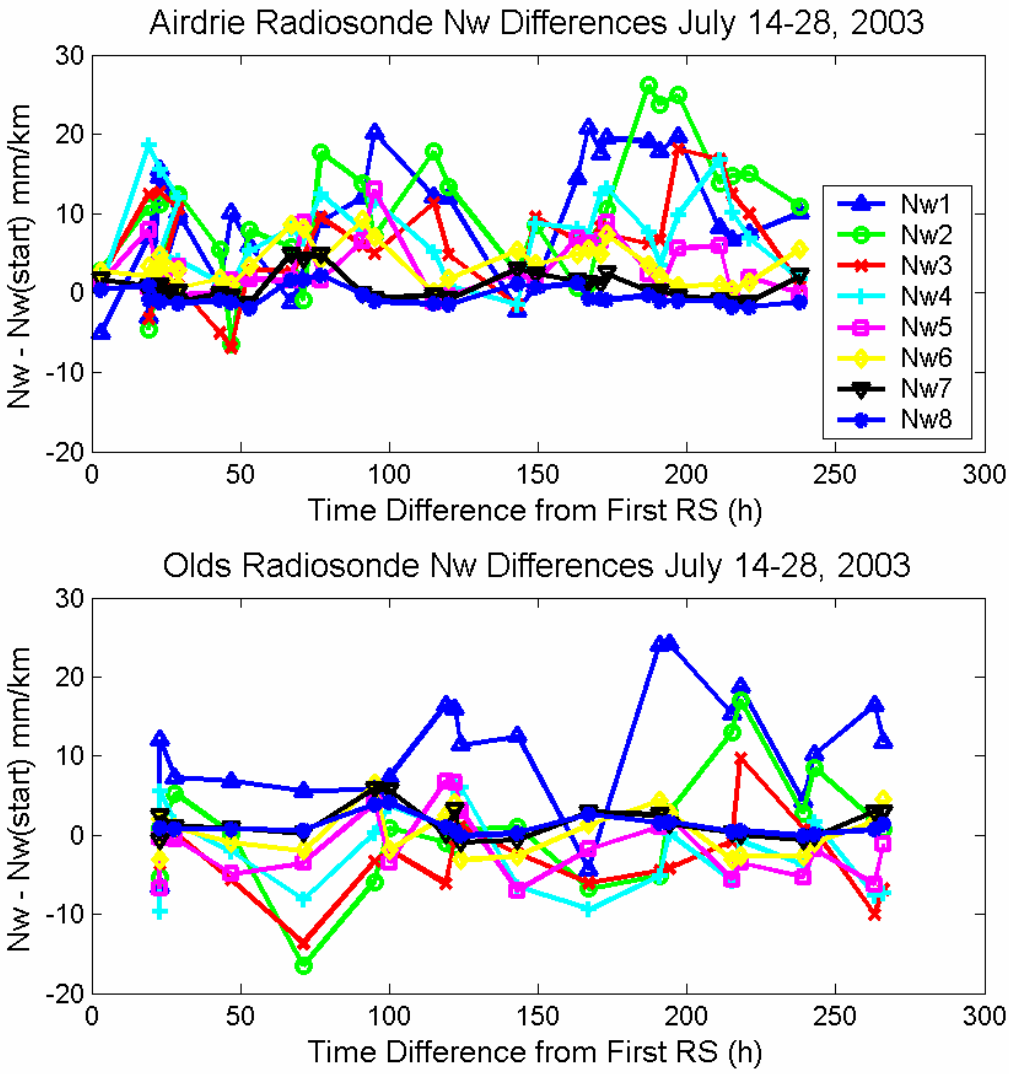

Figure 6.18. Differences in N_W from the first radiosonde in the A-GAME 2003 campaign for the eight layers being used in the tomographic adjustment.

Even over a long period of time, the information contained in a single radiosonde observation holds generally some useful information for later times. Variations seen in Figure 6.18 are not steadily increasing with time from the first launch. For this reason it does not make physical sense to keep increasing the uncertainty for a radiosonde measurement with increasing time from launch since it does include some general

information for the following days, due to the atmosphere behaving over the whole 2003 A-GAME campaign within certain bounds. All radiosondes launched in four-hour intervals were examined for the difference between one radiosonde to the next at Airdrie. These radiosondes were mostly released at 13:00 UTC and 17:00 UTC (7:00 and 11:00 LT), which can be an active time of day for convection and atmospheric variation during the summer in southern Alberta (see Table 6.3).

Table 6.3 Differences in Wet Refractivity (in mm/km) for the Eight Layers Being Estimated During All Four-Hour Intervals of Radiosondes at Airdrie, Alberta in A-GAME 2003

UTC Hour	Date	Nw1	Nw2	Nw3	Nw4	Nw5	Nw6	Nw7	Nw8
17-13	7/16/2003	8.6	0.3	0.3	-3.0	-7.5	2.6	0.2	-2.1
17-13	7/17/2003	17.6	7.5	4.7	3.7	-0.8	-0.2	-0.4	-0.2
17-13	7/18/2003	9.1	-12.0	-1.9	-0.2	1.6	-0.7	-0.3	-0.3
17-13	7/19/2003	3.1	-6.7	1.9	-1.4	7.3	-0.3	-0.7	0.0
17-13	7/20/2003	8.1	-6.7	-1.0	3.6	6.4	-2.2	-0.7	-0.9
17-13	7/23/2003	6.4	0.5	-0.2	-0.9	-0.6	0.6	-0.3	-2.0
21-17	7/23/2003	-3.2	6.1	1.9	5.2	0.3	-0.6	-0.1	0.0
17-13	7/24/2003	-1.3	-2.4	0.5	-4.1	-2.1	-1.4	0.0	-0.7
17-13	7/25/2003	-1.5	0.9	-4.3	-6.6	-6.2	-0.6	-0.4	-0.8
Standard Deviation		**6.7**	**6.3**	**2.6**	**4.0**	**4.9**	**1.3**	**0.3**	**0.8**

The standard deviation found in Table 6.3 was used as a starting point to create an aging factor that was added to the calculated uncertainty of the measurement over time. The standard deviations in Table 6.3 were derived from radiosondes which were taken at the same time of day with the exception of one. This time of day can have convection and other atmospheric dynamics and so the standard deviations presented in Table 6.3 were reduced in order to take the time of day that these differences were made into account. Values of 3, 2, 1, 1, 0.8, 0.6, 0.4 and 0.2 (mm/km) were used for standard deviations for layers one to eight corresponding to the tomography model. When the age factor was added to radiosonde measurement uncertainty (as calculated in Section 5.2), it was not simply added at once, or increased with increasing time. The age factor was ramped up

linearly over the first four hours from the radiosonde's launch, from zero to the values given above, and then held at the values given above for time periods thereafter.

All quiet and storm days were examined while including RS observations into the tomographic adjustment for eight hours at a time. This was to determine for how long the radiosonde measurements could be assimilated into the adjustment and still have a positive impact on accuracy of the tomographic solution.

6.3.1 July 19, 2003 Long-Term Results

Because tests are restricted by the launch times of radiosondes during the A-GAME 2003 campaign, long-term testing for July 19, 2003 starts at 17:00, and a 17:00 Airdrie radiosonde launch is applied from one hour before its launch time until the end of the day (16:00 to 24:00). Truth radiosondes were launched at 18:00 and 23:00 on this day from Olds/Didsbury Airport. The 18:00 truth radiosonde was applied two hours before its launch so that there was some measure of truth to compare to from 16:00 to 18:00, and then the 23:00 truth measurement was applied at 21:00. This was done in an effort to avoid using a truth measurement for accuracy determination after it was three hours old. Applying the radiosonde truth and assimilated observations backwards in time is a definite advantage of post-processing, as if this work were to be done in real-time, it would be necessary to have radiosondes launched from truth and observation locations at the same time in order to perform this kind of analysis.

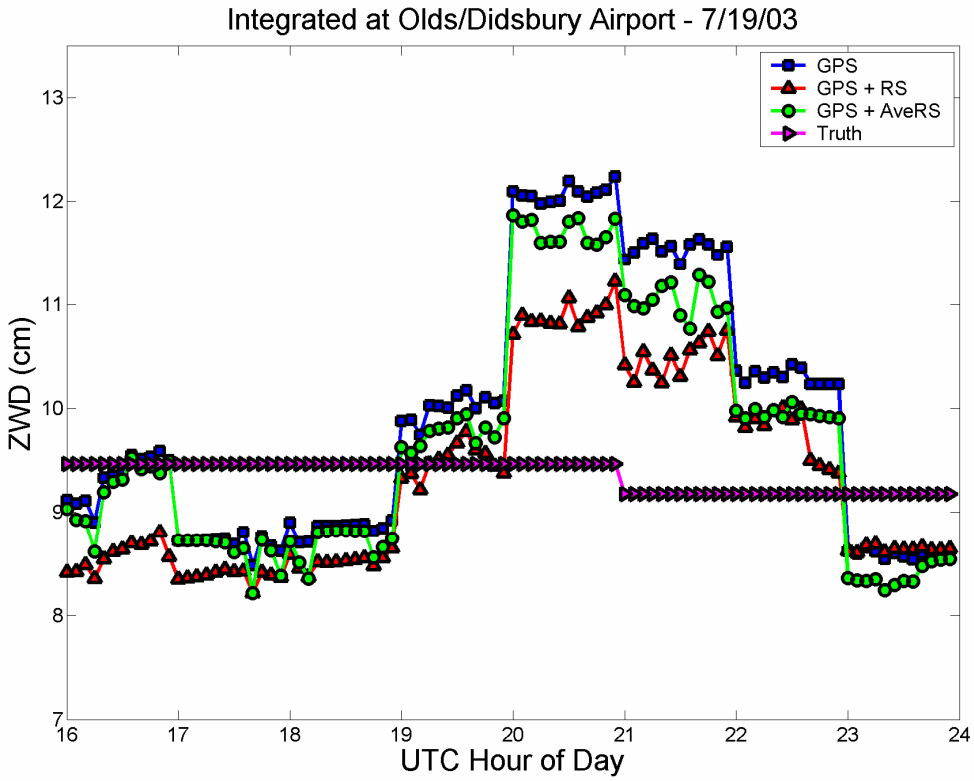

Figure 6.19. Integrated ZWD solutions at Olds/Didsbury airport for July 19, 2003, during testing from 16:00 to 24:00.

The integrated quantities (Figure 6.19) for the GPS + RS match the truth solution better for the most part, especially after 19:00. GPS only and GPS + AveRS solutions closely match each other, which also could be seen in the shorter testing.

A test was conducted using the same day and the same eight-hours of data, but including a factor to age the measurement uncertainty on the RS measurement, as described in Section 6.3. The integrated results are shown in Figure 6.20.

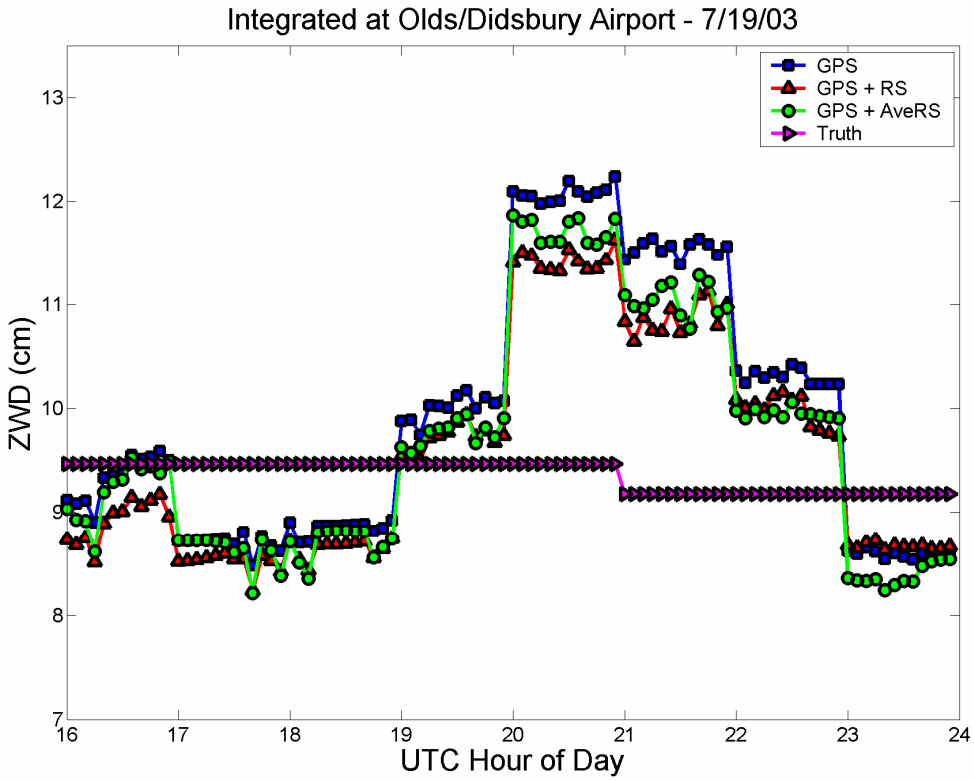

Figure 6.20. Integrated ZWD solutions at Olds/Didsbury airport for July 19, 2003, during testing from 16:00 to 24:00, with an aging RS measurement uncertainty.

The GPS + RS solution is overall much closer to the GPS and GPS + AveRS solutions throughout the test time than was seen in Figure 6.19, particularly near the end of the test time (after 23:00) when the RS measurement has little weight.

6.3.2 July 20, 2003 Long-Term Results

For July 20, 2003, a 17:00 Airdrie radiosonde was assimilated into the tomographic adjustment and was considered valid from 16:00-24:00 on this day. Three truth radiosondes were launched from Olds/Didsbury Airport during the eight-hour test: at 18:00, 21:00 and 23:00. Additional radiosondes were launched on this day due to the storm activity over the SAN, described in Section 6.1. The 18:00 truth radiosonde was

applied starting at 16:00, such that there are truth values for comparison during the period 17:00 to 18:00, and 21:00 and 23:00 truth radiosondes were applied according to their respective time stamps.

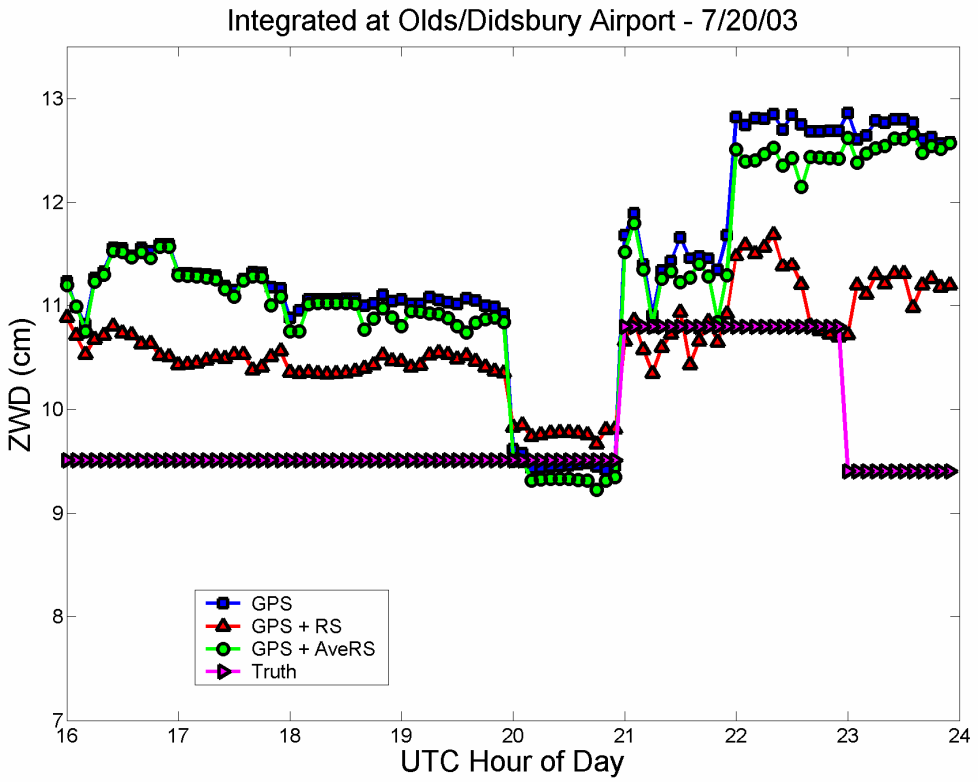

Figure 6.21. Integrated ZWD solutions at Olds/Didsbury airport for July 20, 2003, during testing from 16:00 to 24:00.

In Figure 6.21 there is a significant drop in all tomographic solutions from 20:00 to 21:00, which since it stays constant over the full hour, is probably related to the hourly GPS Bernese V 4.2 estimates for this hour. The truth radiosonde at first viewing might seem to give evidence that this drop is real, but since the "truth" at this point is three hours old, the real truth is probably closer to the 21:00 truth measurement, which is significantly higher. Figure 6.22 shows the integrated solution for the same test as plotted in Figure 6.21, but with the age factor applied.

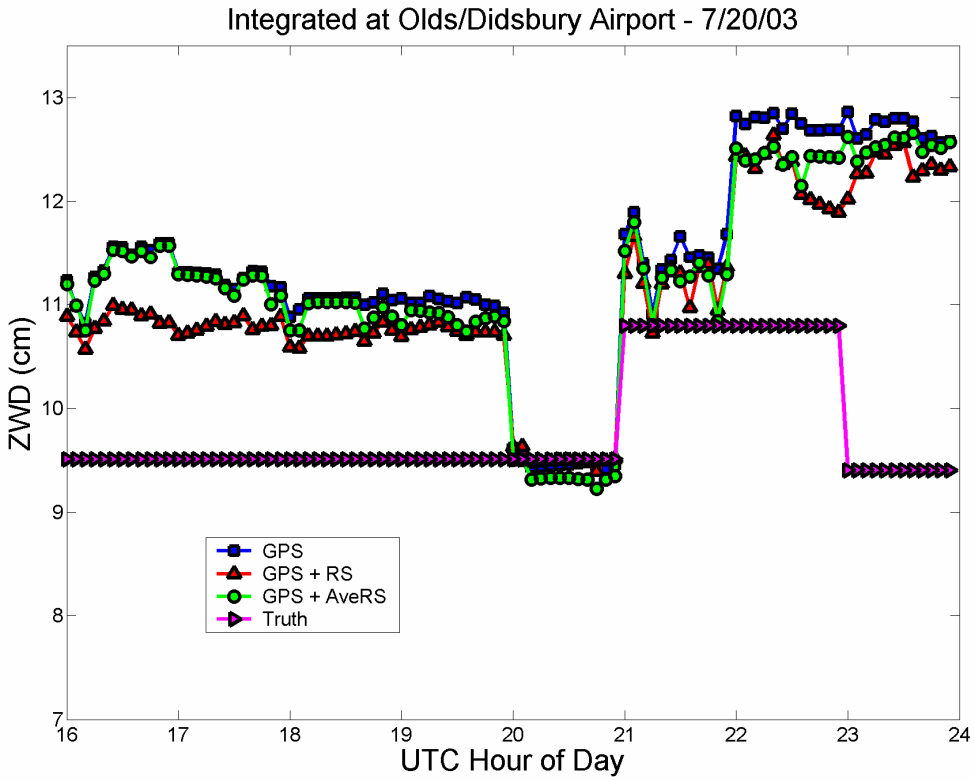

Figure 6.22. Integrated ZWD solutions at Olds/Didsbury airport for July 20, 2003, during testing from 16:00-24:00, with an aging RS measurement uncertainty.

The GPS + RS solution becomes closer to the GPS solution when Figure 6.22 is compared to Figure 6.21, due to the lower weight of the RS measurement.

6.3.3 July 25, 2003 Long-Term Results

In the processing for July 25, 2003 long-term results, a 17:00 Airdrie radiosonde measurement was assimilated at 16:00 and considered valid until 24:00. Truth radiosondes were launched at 18:00 and 23:00 from Olds/Didsbury airport on this day. The 18:00 truth radiosonde was assumed valid from 17:00 until 21:00, at which time the 23:00 truth radiosonde was assumed valid so as to not let the 18:00 truth radiosonde

measurement age past three hours from launch. Results from the long-term testing on this day without a measurement uncertainty age factor applied are given in Figure 6.23.

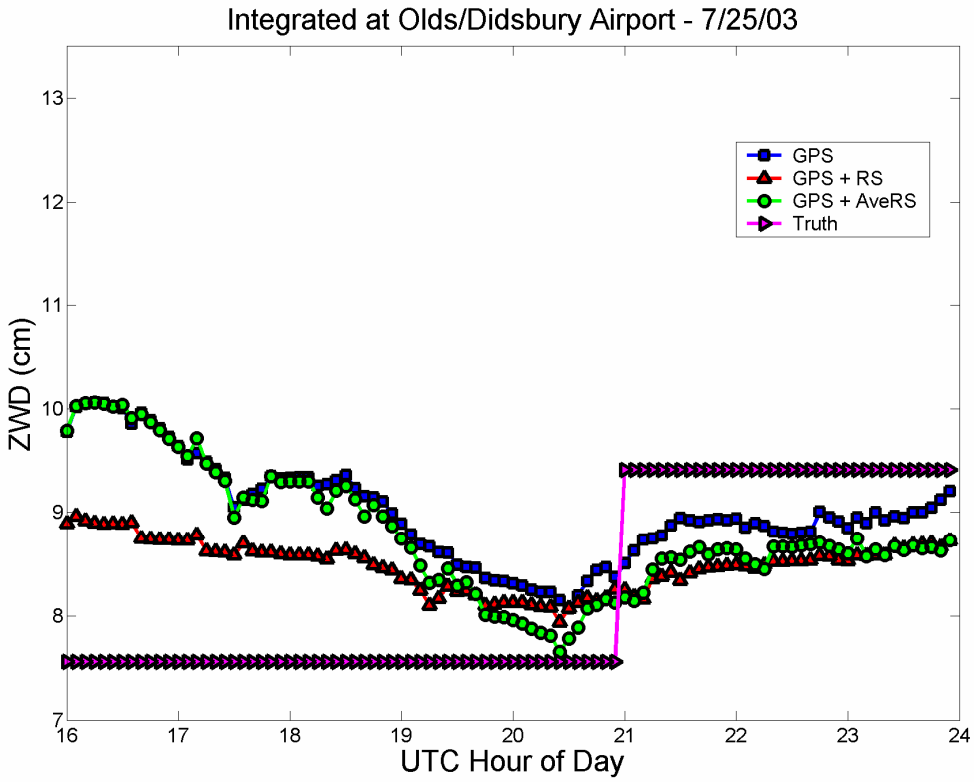

Figure 6.23. Integrated ZWD solutions at Olds/Didsbury airport for July 25, 2003, during testing from 16:00 to 24:00.

The results in Figure 6.23 show the GPS + RS solution being closest to truth out of any solution except from approximately 16:00 to 19:00, where the GPS + AveRS solution is closest to truth until about 21:00. After this time, the GPS solution follows the truth solution most closely out of all tomographic solutions until 24:00. The same test with the age factor applied is shown in Figure 6.24.

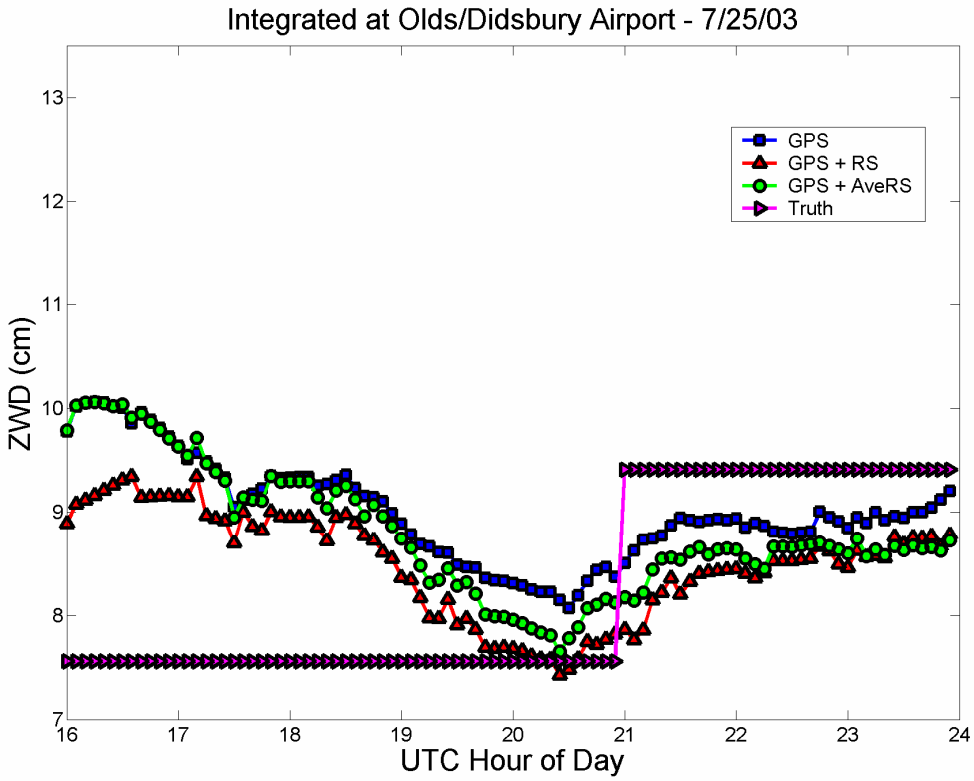

Figure 6.24. Integrated ZWD solutions at Olds/Didsbury airport for July 25, 2003, during testing from 16:00 to 24:00, with an aging RS measurement uncertainty.

With the age factor applied to the RS measurement accuracy, the GPS + RS solution appears to be the best solution from 16:00 to 21:00, here the GPS solution mostly closely follows the truth solution until the end of the test.

6.3.4 July 26, 2003 Long-Term Results

Only one Airdrie radiosonde was launched on July 26, 2003, and this was at 16:00. This measurement was assimilated into the tomography solution for long-term testing during the interval 16:00 to 24:00. Truth radiosonde measurements were taken at 18:00 and 21:00. The 18:00 truth radiosonde was assumed valid from 16:00 to 21:00, when the

21:00 truth radiosonde was then assumed to be valid. Results from the first long-term test are shown in Figure 6.25.

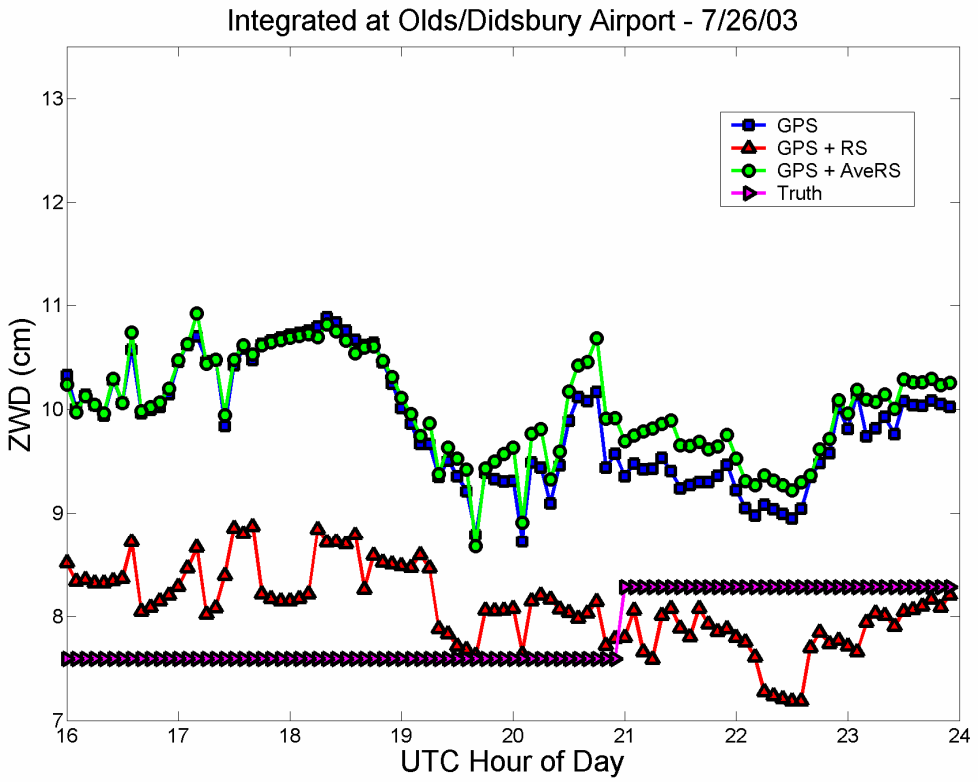

Figure 6.25. Integrated ZWD solutions at Olds/Didsbury airport for July 26, 2003, during testing from 16:00 to 24:00.

The GPS + RS solution can be seen to be the best solution throughout this entire test; the RS measurement assimilated over the eight-hour testing must be representative of the atmosphere as characterized by the truth measurement over this time. GPS and GPS + AveRS solutions only vary slightly from each other, and do not match the truth solution as well as the GPS + RS solution at any point. This long-term test is also performed for July 26, 2003 with an age factor applied to the radiosonde measurement uncertainty, as shown in Figure 6.26.

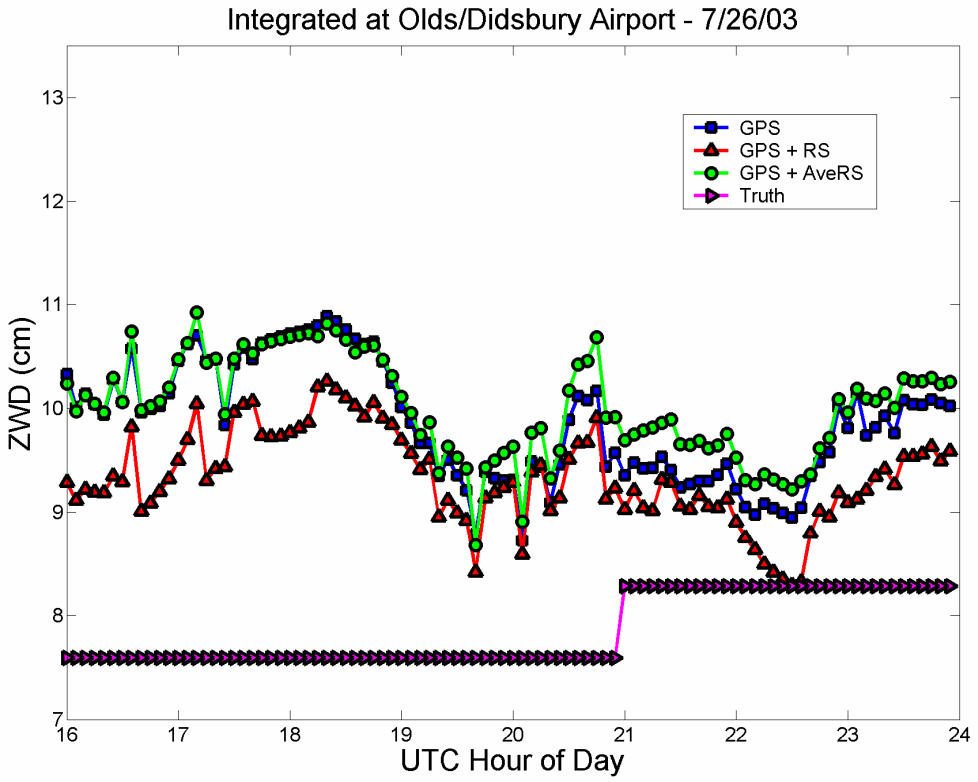

Figure 6.26. Integrated ZWD solutions at Olds/Didsbury airport for July 26, 2003, during testing from 16:00 to 24:00, with an aging RS measurement uncertainty.

When the aging factor is applied in this case, the GPS + RS solution moves significantly towards the GPS and GPS + AveRS solutions, away from the truth. Although the GPS + RS solution is still the tomographic solution closest to the truth, the accuracy for this case becomes degraded versus the case where the RS measurement uncertainty was not aged with time (Figure 6.25). The RS measurement was seen in Figure 6.26 to be closely representative of the truth solution and therefore de-weighting it degraded the accuracy of the solution.

The results for all long-term testing are summarized in Table 6.4.

6.3.5 Summary of Long-Term Results

Aging the measurement accuracy degraded the GPS +RS solution accuracy in every case, from 0.1 cm to 0.9 cm, with this degradation being most prominent on storm days. Storm days show degradation in the GPS + RS solution of at least 0.5 cm with the addition of an aging measurement uncertainty factor. The magnitudes of accuracy for GPS, GPS + RS and GPS + AveRS solutions are similar to those found in Section 6.2 for testing over shorter time periods.

Table 6.4 Zenith Wet Delay Accuracies from Tomography Model over Eight-Hour Testing (Storm Days Shaded)

Date	GPS	GPS + RS	GPS + AveRS
RMS (cm)			
July 19, Long	1.4	1.0	1.2
July 19, Long & Aged	1.4	1.1	1.2
July 20, Long	1.8	1.0	1.7
July 20, Long & Aged	1.8	1.5	1.7
July 25, Long	1.3	0.9	1.3
July 25, Long & Aged	1.3	1.1	1.3
July 26, Long	2.2	0.7	2.3
July 26, Long & Aged	2.2	1.6	2.3
Mean(cm)			
July 19, Long	0.6	0.0	0.3
July 19, Long & Aged	0.6	0.2	0.3
July 20, Long	1.6	0.8	1.4
July 20, Long & Aged	1.6	1.2	1.4
July 25, Long	0.7	0.2	0.5
July 25, Long & Aged	0.7	0.2	0.5
July 26, Long	2.0	0.2	2.2
July 26, Long & Aged	2.0	1.5	2.2
Max (cm)			
July 19, Long	28	18	24
July 19, Long & Aged	28	22	24
July 20, Long	35	19	33
July 20, Long & Aged	35	32	33
July 25, Long	25	14	25
July 25, Long & Aged	25	18	25
July 26, Long	33	13	33
July 26, Long & Aged	33	27	33
Min (cm)			
July 19, Long	-1.0	-1.2	-1.3
July 19, Long & Aged	-1.0	-1.2	-1.3
July 20, Long	-0.1	-0.5	-0.3
July 20, Long & Aged	-0.1	-0.1	-0.3
July 25, Long	-0.9	-1.3	-1.3
July 25, Long & Aged	-0.9	-1.6	-1.3
July 26, Long	0.7	-1.1	0.9
July 26, Long & Aged	0.7	0.0	0.9

GPS and GPS + AveRS results stay the same since they are not being changed for both long-term tests. Using the GPS + RS solution over eight hours improves this solution only slightly over GPS and GPS + AveRS solutions for all days examined, with accuracies from 0.1 cm to 1.5 cm. To assimilate the single radiosonde measurements over such a long time can be of benefit during some intervals of the test, or during the entire test in some cases. Examining the solution hour by hour however, some hours have a good GPS + RS solution versus GPS, while others are not. Assimilating the radiosonde observations over a long time span is best if accuracy is desired in the long term. If short term accuracy is desired, then this approach is not recommended. This approach is best suited for times of the day or seasons when it can be determined that the water vapour fluctuations are low in the troposphere, so that a single radiosonde measurement is highly likely to be representative of the atmosphere for a longer time.

6.4 Sensitivity Analysis for GPS+RS Approach

During the assimilation of radiosonde data for July 19, 2003, a sensitivity study was performed to determine how sensitive the tomographic adjustment (with radiosonde data assimilated) was to changes in the assumed measurement uncertainties of the radiosonde measurement. July 19 was chosen for this analysis because it was a quiet day with good results shown in the testing in Section 6.2; accuracies for the GPS + RS estimation approach were under 0.5 cm for the short tests on this day. The integrated plot for this day (Figure 6.10) shows a GPS + RS solution that closely matches the truth solution and GPS and GPS + AveRS solutions are lower than the truth. This provides an advantageous situation for analysis of the improvement for different settings or cases because visually in the integrated plots for each solution, it will be evident when the GPS + RS solution estimates are closer to truth.

The short test was repeated while radiosonde temperature and then relative humidity measurements were given degraded accuracies to investigate the effect on the

tomographic GPS + RS adjustment. The seven cases studied are summarized in Table 6.5.

Table 6.5 Sensitivity Analysis Settings for the Seven Cases Studied (Default Case Shaded)

Case	Temp Meas. Accuracy (°C/°K)	RH Meas. Accuracy (%)
1	0.1	1
2	0.2	1
3	1	1
4	10	1
5	20	1
6	0.1	1.5
7	0.1	3

Temperature and relative humidity measurement uncertainty was increased slowly at first, and then if no real change in the solution was found, they were changed in large increments until a GPS + RS solution accuracy of 0.7 cm was reached. This value was used because it was still a bit better than the GPS solution which achieves accuracies of 0.9 cm for this day. In effect, the GPS + RS solution was degraded until it reached nearly the same accuracy as the GPS solution, but still had a marginal improvement over the GPS solution. Results for the default case (Case 1) for this testing were derived in Section 6.2.

6.4.1 Sensitivity Testing Results

6.4.1.1 Temperature Measurement Accuracy Degradation

The integrated plots of ZWD were derived for Olds/Didsbury Airport for a truth radiosonde and three tomographic solutions in the same manner as Section 6.2 and 6.3, with different settings for the GPS + RS measurement as given in Table 6.5. The integrated plots for the GPS + RS solution do not show visible changes from the default

case (Case 1) for Cases 2 and 3. The integrated ZWD values for Case 4 are shown in Figure 6.27.

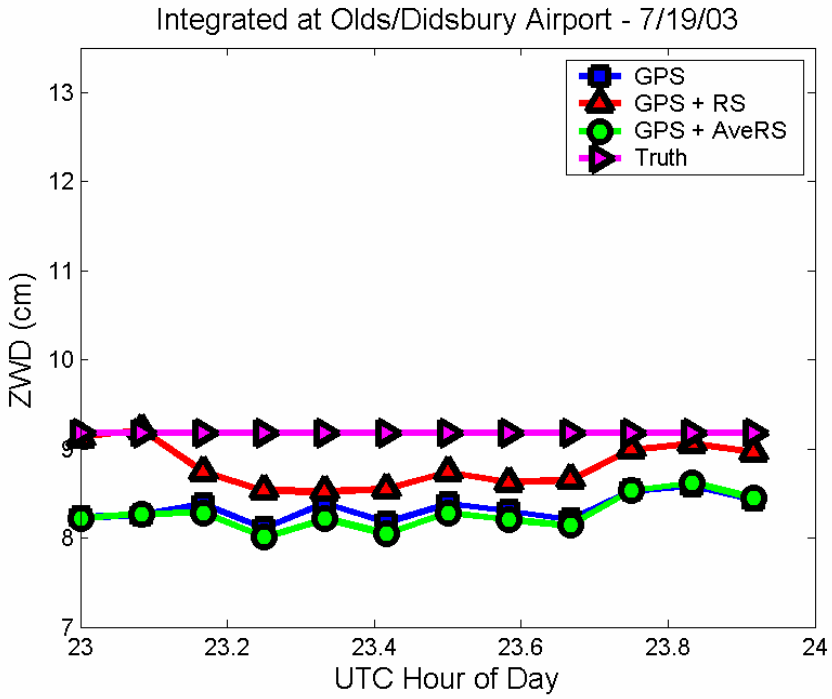

Figure 6.27. Integrated ZWD solutions at Olds/Didsbury airport for July 19, 2003, for Case 4 sensitivity analysis.

The GPS + RS solution in Figure 6.27 is lowered towards the GPS and GPS + AveRS solutions which have not been altered from Case 1 (the default case) in the sensitivity analysis. The RS observation is starting to be weighted less in the tomographic solution for Case 4 and the tomographic GPS + RS solution is becoming more dependent on the GPS data. The general shape of the GPS + RS solution is preserved from the default case (as can be seen in Figure 6.10). The profile for the mid-time of Figure 6.27 is shown for Case 4 in Figure 6.28 to demonstrate in which layers the N_W solution changes.

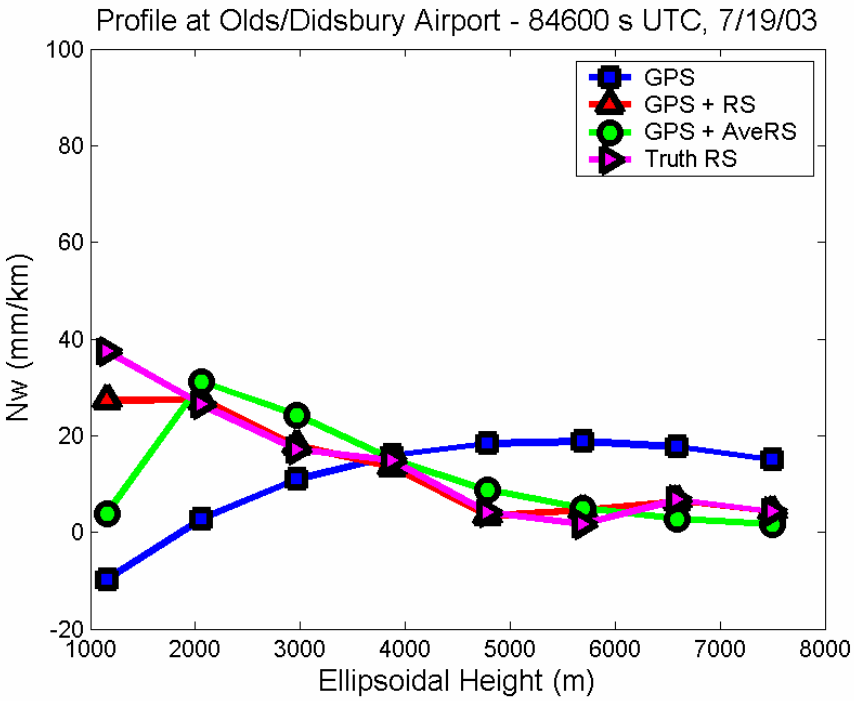

Figure 6.28. Wet refractivity profile over Olds/Didsbury airport for July 19, 2003, for Case 4 sensitivity analysis.

The solution for GPS + RS changes particularly for its estimation of the lowest layer, which indicates estimates for this layer in the adjustment are most affected by changes made to the accuracy of temperature in the RS measurement during assimilation. This layer will see the highest temperatures out of any layer being estimated (see Figure 2.3 for confirmation). Profiles for cases where the assumed temperature uncertainty is further increased show solutions for this bottom layer converging with that for the GPS solution. This is a reasonable result since as the RS measurement is being weighted less heavily (through higher uncertainties in temperature measurement) in the adjustment, the GPS observations will be more heavily weighted in the solution, and GPS measurements themselves make a very low estimation of N_W for the lowest layer in the tomography model during this test.

The gradual convergence of the GPS + RS solution towards the GPS and GPS + AveRS solutions can be further seen in Figure 6.29 for Case 5.

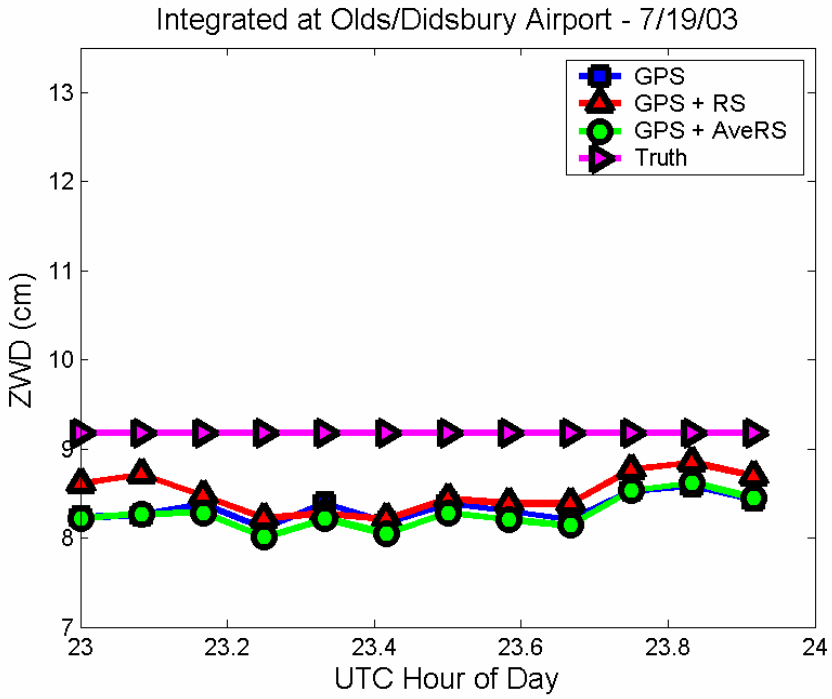

Figure 6.29. Integrated ZWD solutions at Olds/Didsbury airport for July 19, 2003, for Case 5 sensitivity analysis.

The GPS + RS solution in Figure 6.29 starts to lose some of its characteristics, particularly between 23.2 and 23.4 UTC, where the ZWD solutions for Cases 1-4 were curved downwards, it now shows a small spike which can be seen in the GPS and GPS + AveRS solutions. The GPS + RS solution has become more similar to the GPS and GPS + AveRS solutions in this case, diverging away from the truth solution. This is the last case where the temperature has been changed from the default values.

6.4.1.2 Relative Humidity Measurement Uncertainty Degradation

Case 6 and 7 present the ZWD solutions derived while varying the relative humidity assumed measurement uncertainty for the RS measurement, as given in Table 6.5. Case 6 is presented in Figure 6.30.

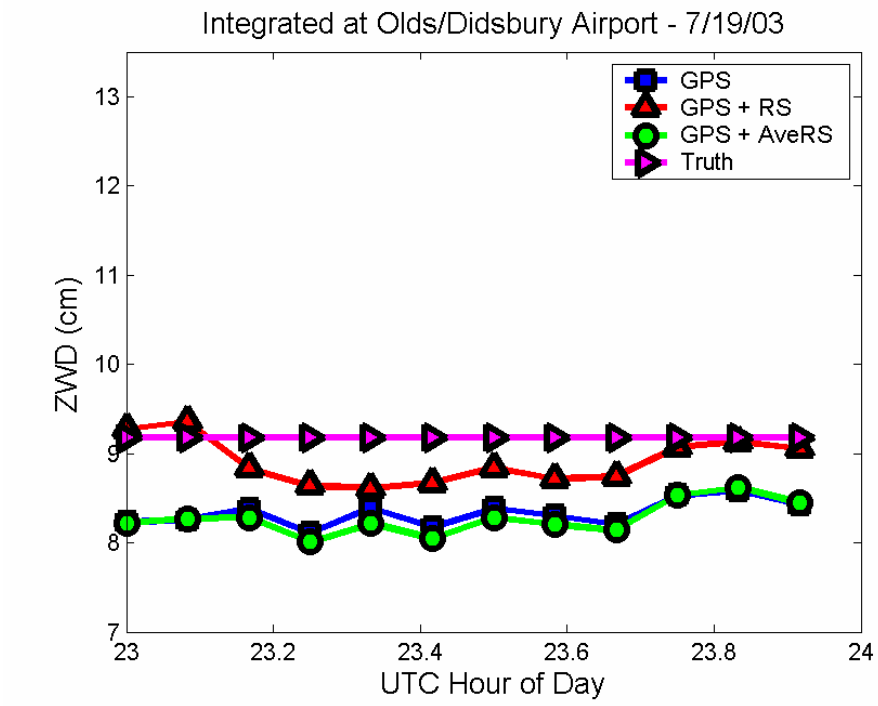

Figure 6.30. Integrated ZWD solutions at Olds/Didsbury airport for July 19, 2003, for Case 6 sensitivity analysis.

Already for this case, there is a significant change in the GPS + RS solution with only a change in the relative humidity measurement uncertainty of 0.5% from the default case (Case 1). The tomographic solution with the RS measurements assimilated converges towards the GPS and GPS + AveRS integrated ZWD results.

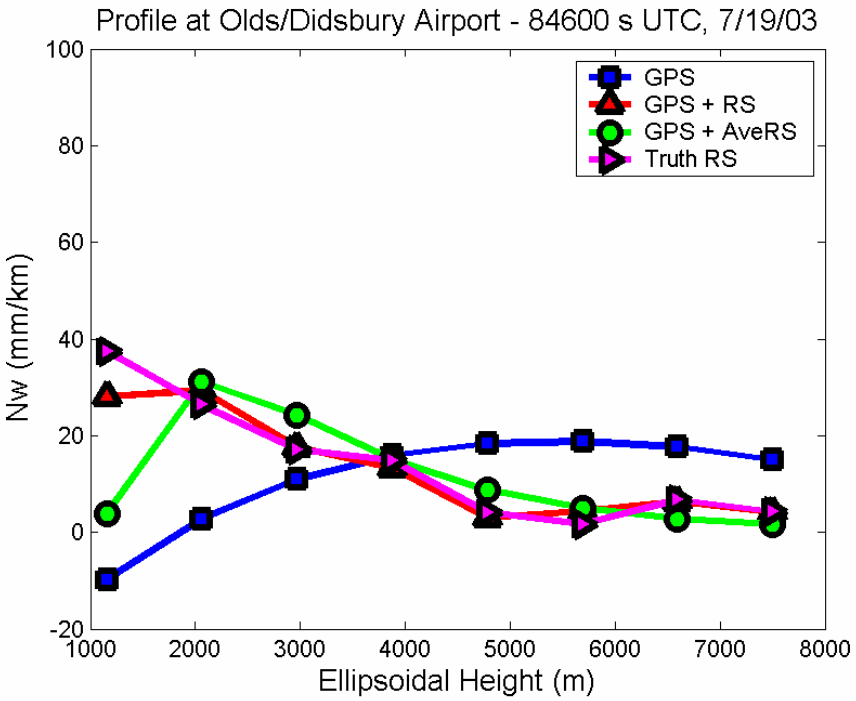

Figure 6.31. Wet refractivity profile over Olds/Didsbury airport for July 19, 2003, for Case 6 sensitivity analysis.

The profile given in Figure 6.31 for Case 6 is very similar to the one shown in Figure 6.28, but not only has the solution for the lowest layer changed, but also the second lowest layer. Generally it can be said that water vapour falls off exponentially with increasing height, so these layers should have the largest N_W values out of all layers being estimated, however in Figure 6.31 the estimation for the lowest layer is converging towards the GPS solution as the weighting on the RS measurement for this layer is lessened.

The final case in the sensitivity analysis is shown in Figure 6.32.

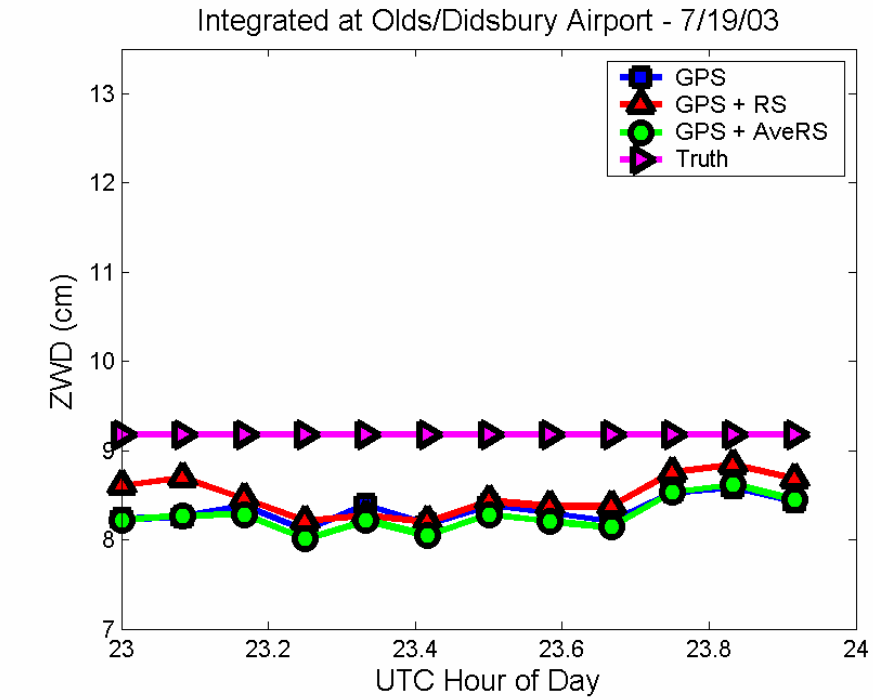

Figure 6.32. Integrated ZWD solutions at Olds/Didsbury airport for July 19, 2003, for Case 7 sensitivity analysis.

With an increase of 2% in the measurement accuracy of relative humidity from the default settings as used in Case 7, the same result is achieved as increasing the temperature measurement accuracy on the RS measurement of 20 ºC/ºK (Case 5). Small changes in the uncertainty of the radiosonde measurements make a significant impact on the tomographic solution. In order to achieve this same level of degradation by changing temperature measurement uncertainty, changes have to be made on the order of 20 ºC/ºK.

6.4.2 Summary of Results

Changing the measurement uncertainty for the temperature observations did not affect the tomographic adjustment significantly until very large uncertainties were obtained, such as 10 °C; however, small changes in the assumed accuracy of the relative humidity measurement allowed large changes in the accuracy of the tomographic GPS + RS

predictions. The adjustment is very sensitive to changes in the accuracy of relative humidity, and it takes large changes in the assumed temperature measurement uncertainty to affect the tomographic accuracy, as seen in Table 6.6.

Table 6.6 Zenith Wet Delay Accuracies (GPS + RS) from Tomography Model during Times when Radiosonde Observations are Available on July 19, 2003 for Sensitivity Analysis (Default Setting for Previous Sections Shaded)

Case	Temp Meas. Accuracy (°C/°K)	RH Meas. Accuracy (%)	RMS (cm)
1	0.1	1	0.3
2	0.2	1	0.3
3	1	1	0.3
4	10	1	0.4
5	20	1	0.7
6	0.1	1.5	0.4
7	0.1	3	0.7

6.5 Climate Model Measurement Uncertainty

To determine if an increased measurement certainty for the climate data would make an improved solution over weighting this measurement as a monthly average (as was done in all previous testing), tests were conducted for GPS + AveRS using the same measurement uncertainty derived for a RS measurement used on July 19, 2003. This measurement uncertainty was used for all days since it represented a very high weight that was successfully applied for the single radiosonde (RS) measurements. (Recall Figure 5.3 which shows the measurement uncertainty for an RS measurement versus an AveRS measurement.) Weighting the AveRs measurement more than this would not be valid since the RS direct observations are the most accurate measurement of vertical wet refractivity that is available (since it is made *in situ*). The same tests that were used in Section 6.2 were conducted for this additional analysis, except with different AveRS observation uncertainties used in the assimilation.

Since the AveRS measurement is an average over a month, it is hypothesized that on those instances when the AveRS measurement is close to the truth measurement, increasing the weight for the AveRS measurement will improve tomography model accuracies through improved vertical constraints. If, however, the AveRS solution is not similar to the truth measurement at the time tested, it will cause the model to estimate integrated solutions which are further from the truth. For this reason, the AveRS integrated ZWD measurements are plotted on all figures of integrated ZWD so as to better illustrate the expected impact of higher weighting of AveRS measurements (and how these observations might affect the overall tomography solution).

6.5.1 July 19, 2003 Results

The GPS + AveRS ZWD estimates are increased through higher weighting of AveRS measurements for this day (Figure 6.33), and the GPS + AveRS solution becomes more accurate than for the default weighting scheme used in Section 6.3 (Figure 6.10). This is because the integrated AveRS ZWD measurement is higher than truth values, and it has a positive affect on the overall GPS + AveRS solution, causing it to increase and diverge from the GPS ZWD solution - which is lower than truth.

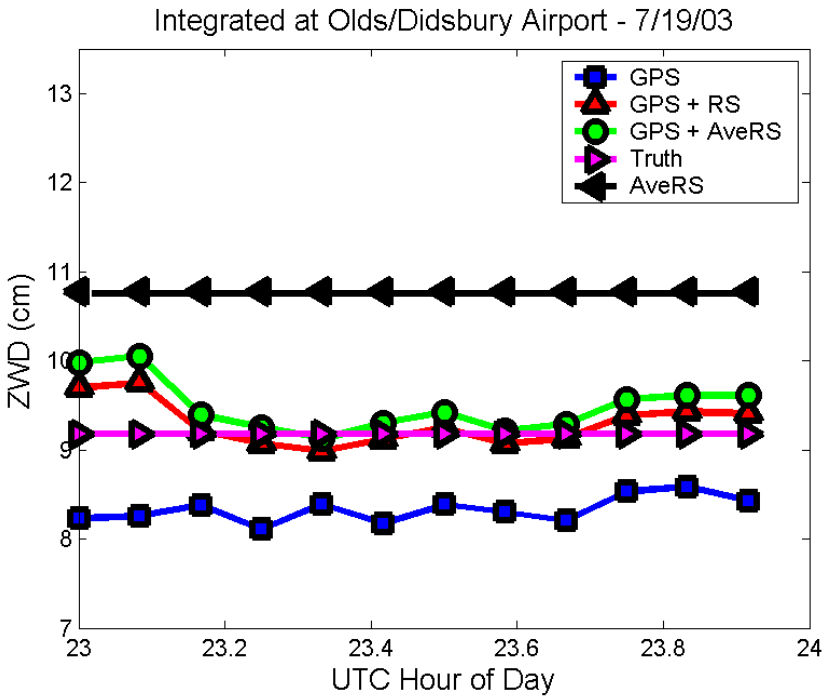

Figure 6.33. Integrated ZWD solutions at Olds/Didsbury airport for July 19, 2003, with AveRS weighted as a RS measurement.

A similar shape is seen in the GPS + RS and GPS + AveRS solutions. This is because the vertical profiles of N_W at this time for both of these solutions is very similar, which can be seen in Figure 6.34.

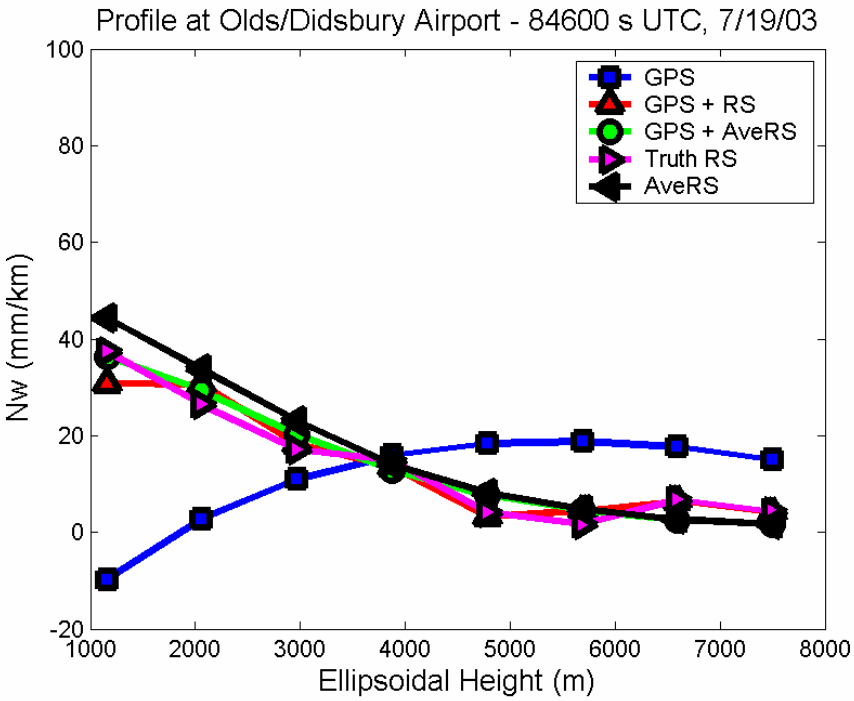

Figure 6.34. Vertical N_W profile at Olds/Didsbury airport July 19, 2003, 23:30 UTC (midpoint of Figure 6.33), with AveRS weighted as a RS measurement.

6.5.2 July 20, 2003 Results

Because the AveRS solution is closer to the truth solution than the GPS solution (Figure 6.35), higher weighting of the AveRS measurement (as a RS measurement) improves the ZWD solution over solutions derived in Section 6.3 for this test time. In this case, however, the AveRS observations can only improve the tomography ZWD solution by a marginal amount (versus GPS only) since the AveRS observations of ZWD are more than 1 cm larger than the truth solutions. Therefore, assimilation of the AveRS observations has only a minimal impact.

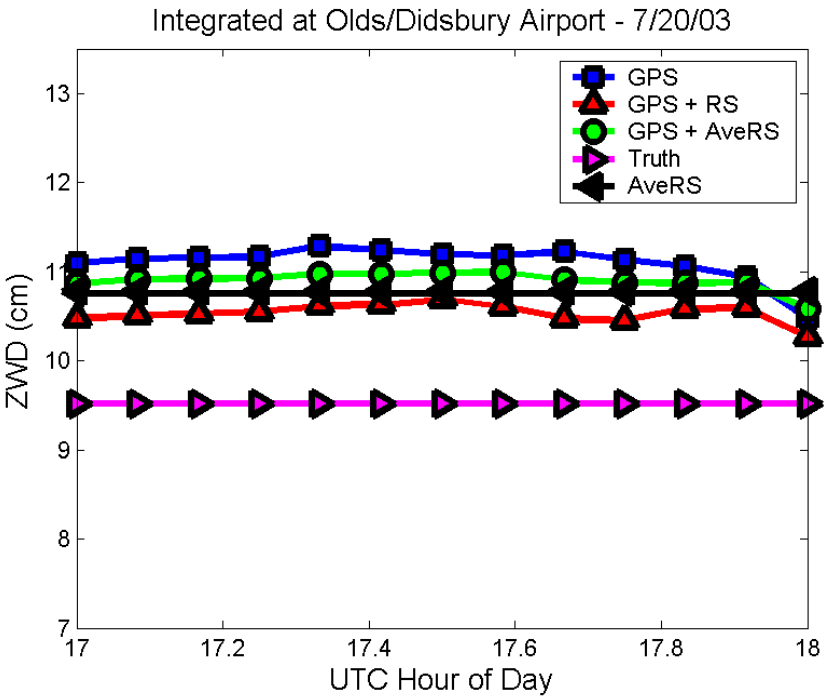

Figure 6.35. Integrated ZWD solutions at Olds/Didsbury airport for July 20, 2003, with AveRS weighted as a RS measurement.

The profile for the mid-time of Figure 6.35 is shown in Figure 6.36. Some of the local variation resolved in the GPS + RS solution is lost by weighting the AveRS solution heavily. Figure 6.36 shows that the AveRS measurement alone does not show this local variation in its profile, the AveRS profile being an average climate estimate.

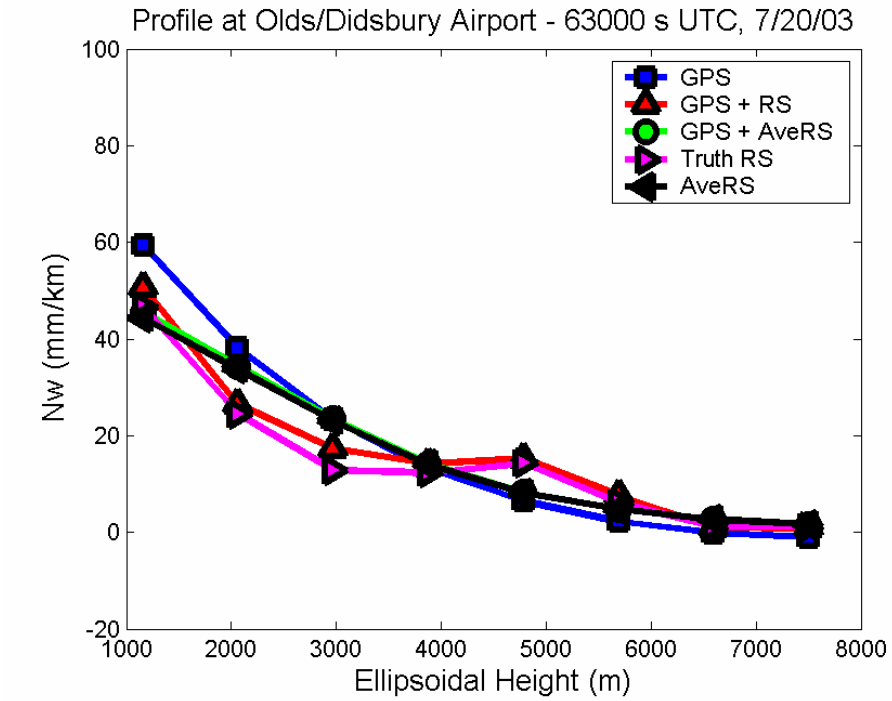

Figure 6.36. Vertical N_W profile at Olds/Didsbury airport July 20, 2003, 17:30 UTC (midpoint of Figure 6.31), with AveRS weighted as a RS measurement.

6.5.3 July 25, 2003 Results

In Figure 6.37, the AveRS measurement of ZWD is larger than both the truth ZWD and the GPS ZWD solutions. In this case, increasing the weight for the AveRS measurement in the tomography adjustment degrades the GPS + AveRS solution, as compared to the GPS solution.

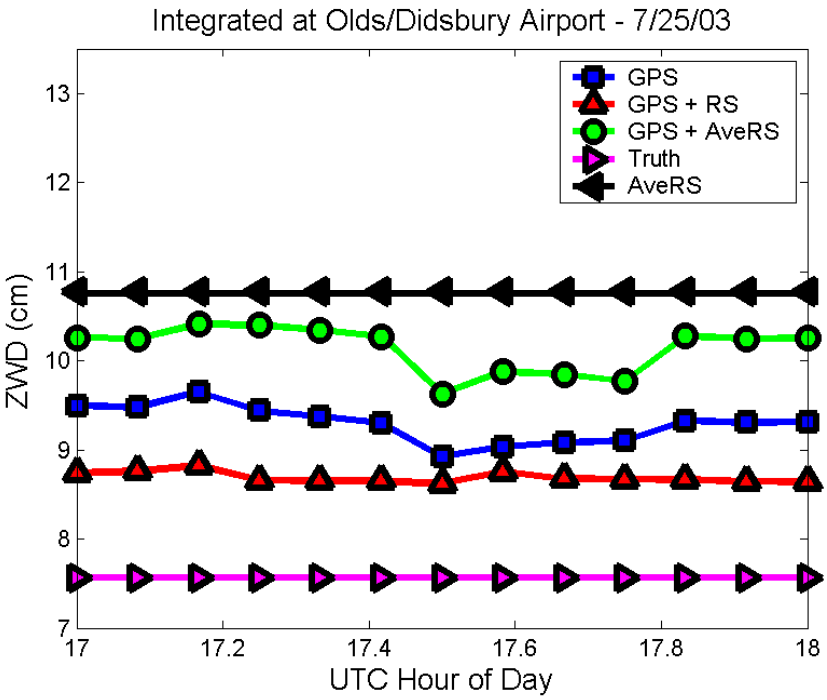

Figure 6.37. Integrated ZWD solutions at Olds/Didsbury airport for July 25, 2003, with AveRS weighted as a RS measurement.

The profiles for the mid-time of Figure 6.37 do not show a vertical solution for GPS + AveRS that is significantly different from the truth (Figure 6.38); however, Figure 6.38 is valid for just one epoch out of the entire adjustment period, which is the time (Figure 6.37) at which the GPS and GPS + AveRS solutions best match the truth. Profiles have only been taken at the mid-time of integrated graphs for consistency and brevity.

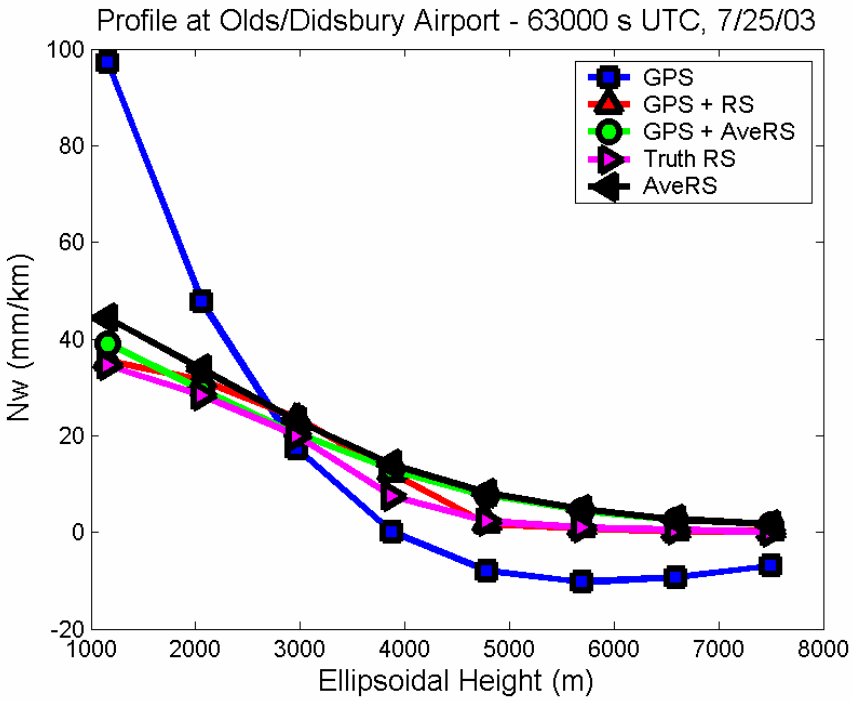

Figure 6.38. Vertical N_W profile at Olds/Didsbury airport July 25, 2003, 17:30 UTC (midpoint of Figure 6.33), with AveRS weighted as a RS measurement.

6.5.4 July 26, 2003 Results

The results for ZWD estimates here (Figure 6.39) are similar to the results derived for July 25, 2003 (Section 6.5.3); because the integrated ZWD solution for AveRS is higher than the GPS solution or truth solution increased weighting of the AveRS observations in the tomography solution causes larger errors in the GPS + AveRS ZWD estimates.

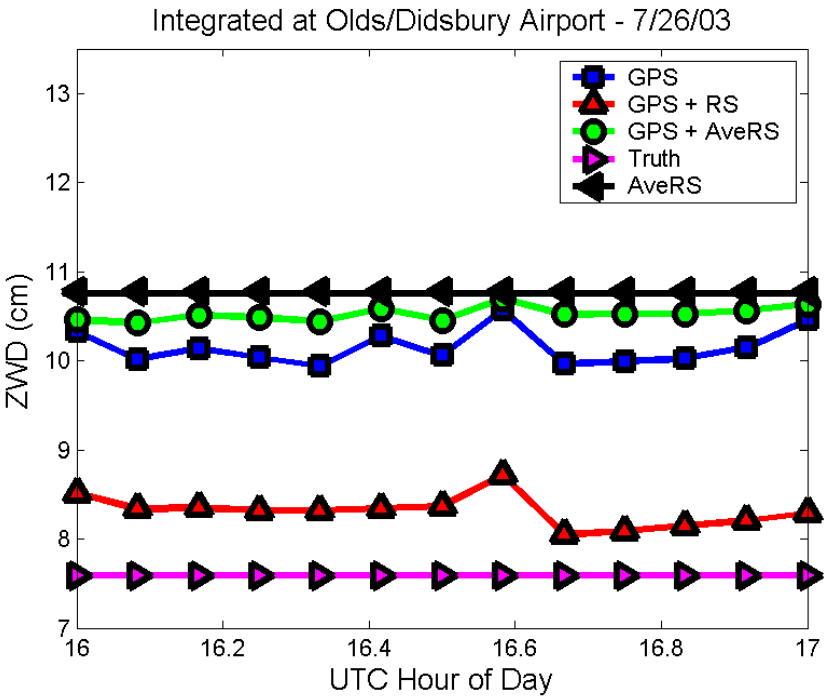

Figure 6.39. Integrated ZWD solutions at Olds/Didsbury airport for July 26, 2003, with AveRS weighted as a RS measurement.

The profile for the mid-time of Figure 6.39 shows a GPS + AveRS solution for *Nw* which is very close to the AveRS *Nw* profile (Figure 6.40). Some very local variation seen in the truth and GPS + RS solution in Figure 6.40 is not resolved by the GPS + AveRS solution since the RS observations are the only measurements that resolve this short term variation.

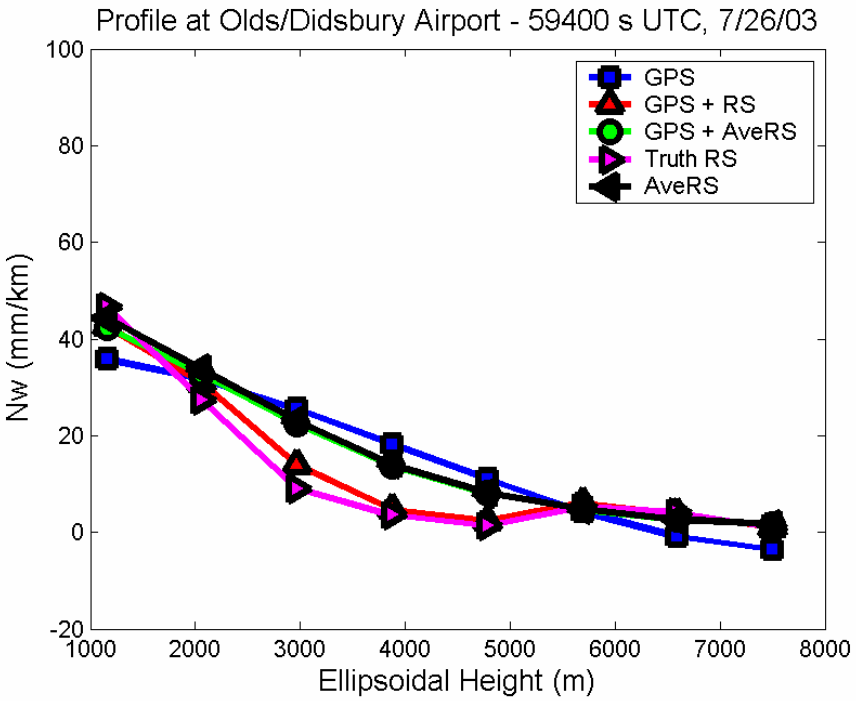

Figure 6.40. Vertical N_W profile at Olds/Didsbury airport July 26, 2003, 16:30 UTC (midpoint of Figure 6.39), with AveRS weighted as a RS measurement.

6.5.5 Summary of Results

Table 6.7 summarizes all results for the climate model measurement accuracy testing. The increased weighting on the GPS + AveRS measurement in the tomographic adjustment is seen to improve the accuracy of the solution on July 19 and 20, and negatively affect the solution accuracy on July 25 and 26.

Table 6.7 Zenith Wet Delay Accuracies from Tomography Model over Reduced Climate Model Measurement Uncertainty Testing

Date	Original GPS + AveRS	GPS + AveRS
RMS (cm)		
July 19	0.9	0.4
July 20	1.6	1.4
July 25	1.8	2.6
July 26	2.6	3.0
Mean (cm)		
July 19	-0.9	0.3
July 20	1.6	1.4
July 25	1.8	2.6
July 26	2.6	2.9
Max (cm)		
July 19	-0.6	0.9
July 20	1.8	1.5
July 25	2.2	2.9
July 26	3.1	3.1
Min (cm)		
July 19	-1.2	0.0
July 20	0.9	1.1
July 25	1.4	2.1
July 26	2.4	2.8

Because the AveRS measurement is made as an average of an entire month of RS measurements, it is not appropriate to always weight these observations heavily - as sometimes the AveRS measurements can benefit the tomography solution, and sometimes the AveRS measurements can cause the ZWD (and N_W) solutions to diverge from truth values. Tests conducted in this section prove that the weighting scheme applied in Section 6.2 to AveRS measurements is most appropriate, since it increases the accuracy of the vertical profile of wet refractivity. The weighting scheme applied in Section 6.2 does not improve the ZWD estimates, however, this is preferable to having estimates that could be beneficial or harmful to the adjustment since this will not be able to be determined until the post-processing stage.

6.6 Occultation Data Assimilation Results

Occultation measurements were assimilated into the tomography model using GEM data to isolate wet refractivity, as outlined in Section 5.4. The occultation measurement (N_W profile) was taken to be valid over the entire test time on September 1, 2003, and two test intervals were evaluated: 1) a short-term test period of two hours, and 2) an extended eight-hour test period. These two intervals were chosen to investigate the length of time over which the occultation measurement could be assumed valid and improve the vertical accuracy of the tomographic adjustment. A second eight-hour test was also conducted in which the occultation measurement is given an aging measurement uncertainty over time to determine if this made an improvement to the previous eight-hour test results.

Work done by *Aparicio and Deblonde* [2004] indicates a poor quality of occultation observations below 5 km and, therefore, all tests were repeated with the lower five occultation measurements removed (altitudes below 5 km) so that the occultation observations were only used to constrain the upper three atmospheric layers in the tomography model - to see if this would improve model accuracies versus those found for the eight-layer occultation case.

No truth radiosonde measurements were available during this day. An alternate measure of accuracy is therefore used for the results presented here. In deriving the occultation results, the tomography adjustment was computed several times, with each SAN station (with data) removed from the solution, in turn, in successive adjustments. Zenith wet delays (ZWD) from the excluded station were considered to be independent measures of truth and were compared with model predictions at the given station location. Results were derived in this way for the various tests. RMS values were computed for comparisons between the excluded station's ZWD (derived from Bernese V 4.2 processing) and the tomographic ZWD prediction at the station. These values are represented spatially in latitude and longitude, with a block of colour surrounding each

station name to represent the RMS value for that station. A colour bar in each image shows the magnitude that each colour block represents.

It should be noted that removing a station from the adjustment weakens the tomographic solution, particularly for the area around the given station since there are a lower number of observations. Stations that are located in regions sparse in data already suffer from the model errors resulting from less data in that area.

6.6.1 Raw Solution Examination

In order to use the Bernese V 4.2-derived ZWD for comparisons, these values are assessed to verify that there are no biases in the ZWD estimates with respect to the occultation observations (e.g. tomographic solutions with the occultation observations assimilated). Therefore, ZWD predictions from the tomography model were compared with the Bernese-derived ZWD observations at each GPS station in the adjustment. This was done for all tests performed, but results here show the case for two-hour, not-aged-with-time occultations measurements being assimilated for eight and three layers. Some stations had Bernese-derived ZWD observations that were higher than the tomography predictions, as in Figure 6.41 from Three Hills.

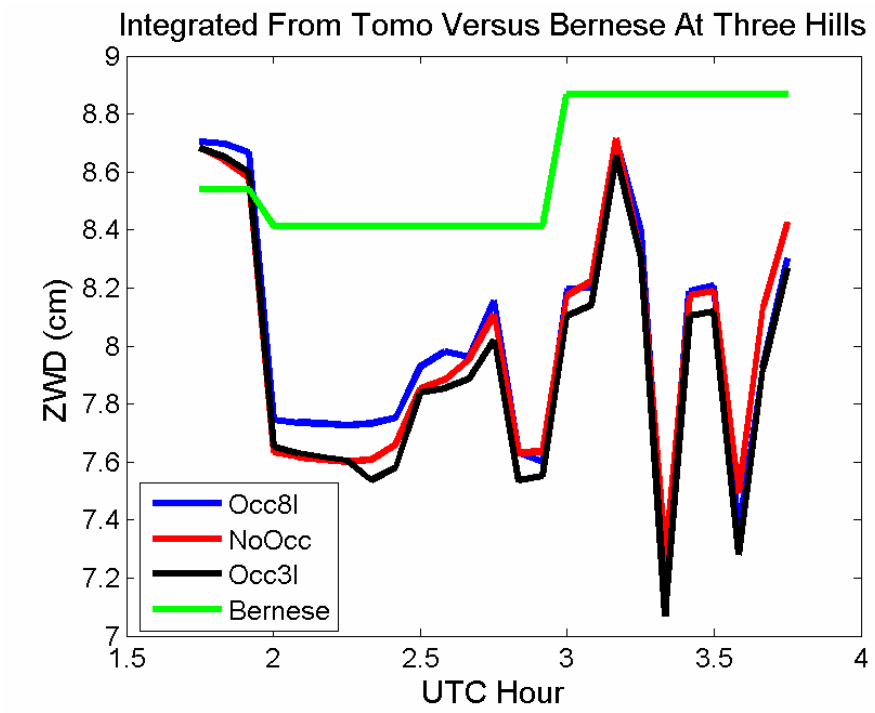

Figure 6.41. Integrated ZWD solutions (Bernese) on September 1, 2003 compared with tomographic predictions at Three Hills.

ZWD observations were also derived (from Bernese) that were lower than the tomographic solutions, as shown for Brooks in Figure 6.42.

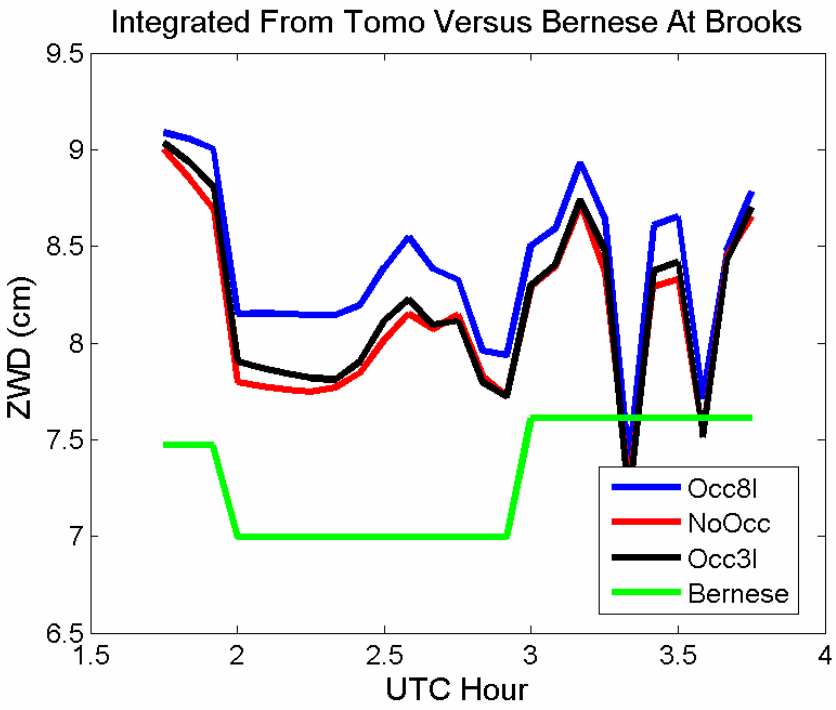

Figure 6.42. Integrated ZWD solutions (Bernese) on September 1, 2003 compared with tomographic predictions at Brooks.

The Bernese ZWD solution also closely matches the solution from the tomography model in some cases. Figure 6.43 compares the Bernese-derived ZWD observations to the tomography predictions of ZWD at Hanna. The solutions are close in magnitude.

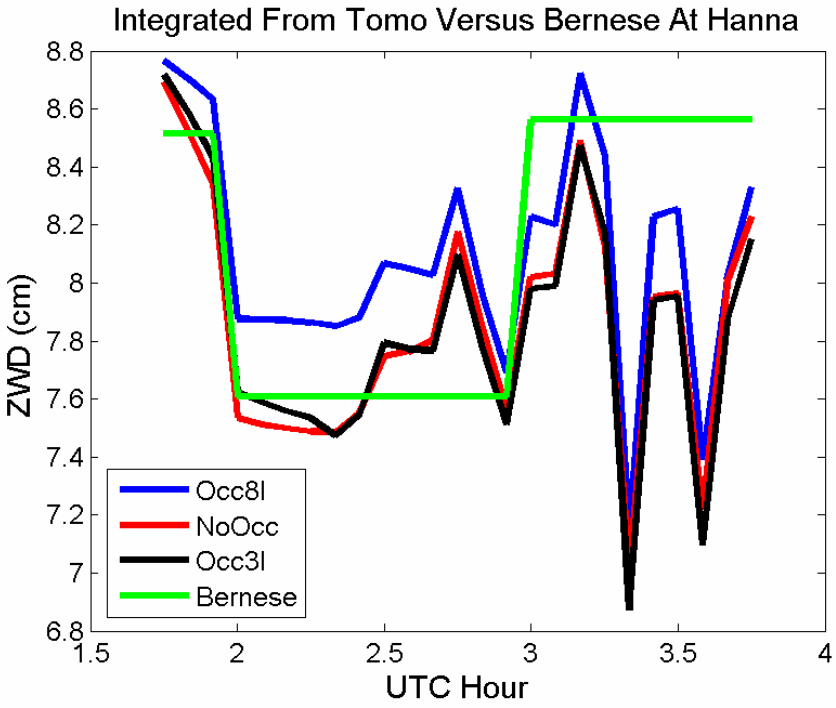

Figure 6.43. Integrated ZWD observations (Bernese) on September 1, 2003 compared with tomographic solutions at Hanna.

Observations of ZWD derived using Bernese software were not consistently lower or higher with respect to the tomographic solutions for ZWD at the stations for the overall tests. *Ergo* it was concluded that there was no bias in the Bernese network solutions for ZWD that may bias the "truth" values with respect to network tomographic solutions of ZWD for the GPS SAN stations processed.

6.6.2 Results from Two-Hour Test Interval With Measurement Uncertainty Not Aged

Results are first shown for the case where no occultation measurements are assimilated into the tomographic solutions in Figure 6.44.

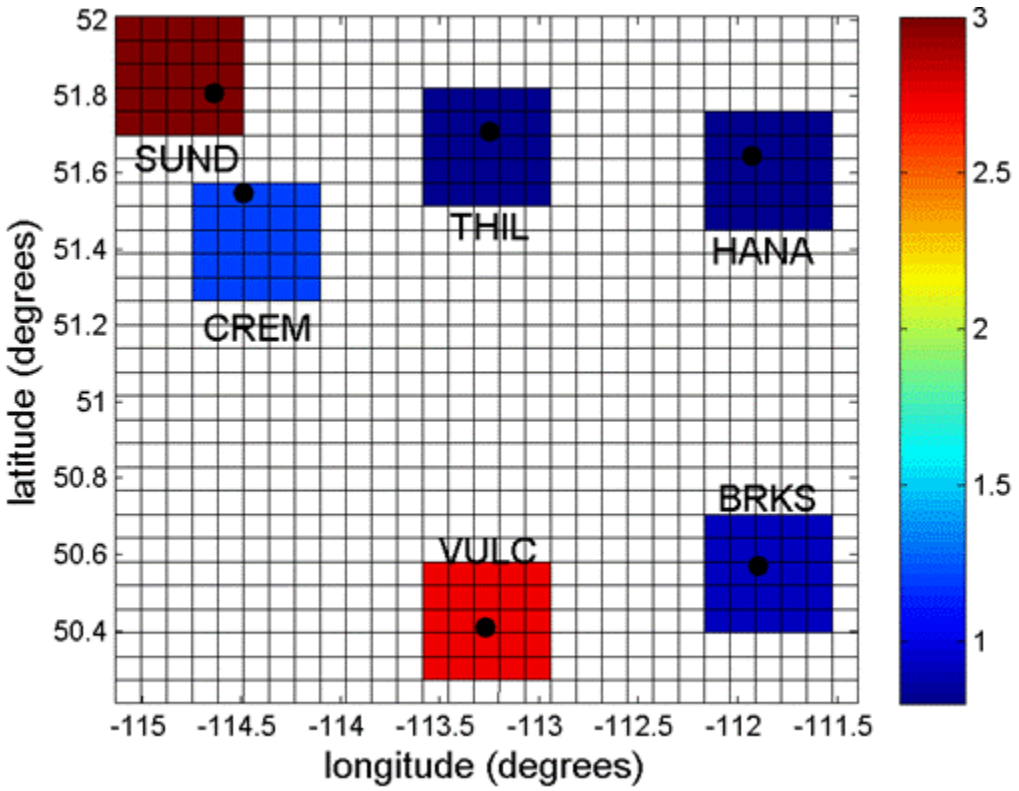

Figure 6.44. RMS (cm) of ZWD accuracies over two-hour interval without occultation measurements assimilated.

This solution shows good agreement between the tomographic output and ZWD observations at Cremona, Three Hills, Hanna and Brooks. Sundre and Vulcan have RMS values at least one centimetre greater than the other sites. Once the eight-layer occultation measurement is assimilated into the tomographic adjustment, the RMS values are changed from this default case (Figure 6.45).

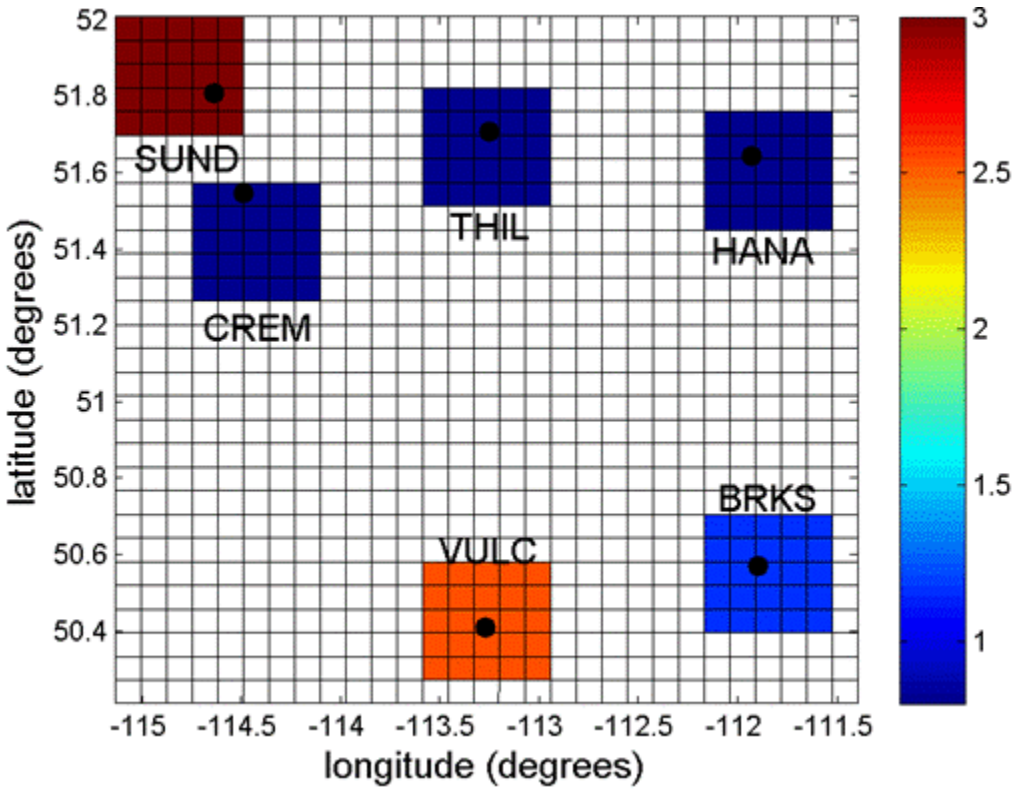

Figure 6.45. RMS (cm) of ZWD accuracies over two-hour interval with an eight-layer occultation measurement assimilated.

The results from Figure 6.45 show an improved solution at Vulcan and Cremona, for the case where occultations are assimilated into the tomography model, and a slightly worse solution at Brooks. Testing was repeated with only the three top layers of the occultation measurement being included and results are shown in Figure 6.46.

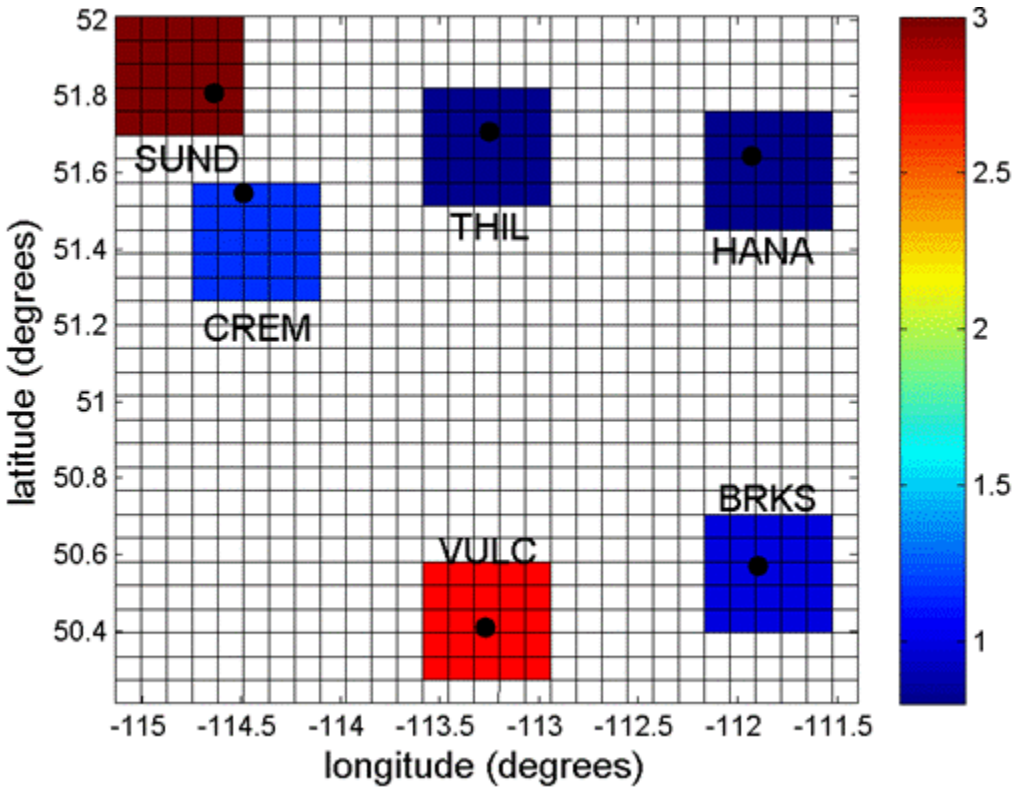

Figure 6.46. RMS (cm) of ZWD accuracies over two-hour interval with a three-layer occultation measurement assimilated.

For the case where only the upper three layers of the occultation measurement are assimilated, Vulcan is the only station that has a slightly improved solution (lower RMS) in comparison to the case with no occultation measurements assimilated. This level of improvement is not as good as that obtained from including all eight layers of the occultation measurement in the tomography adjustment.

6.6.3 Results from Two-Hour Test Interval With Measurement Uncertainty Aged

Testing was also conducted, similar to that of the previous section, with the occultation measurement uncertainty increasing over time (starting from the time at which the occultation measurement occurred). In this analysis, an additional 5% of the total refractivity was added to the occultation measurement uncertainty each hour. The value

of 5% was chosen to add after every hour from occultation measurement time because it was a reasonable increment, given that the measurement starts with this much uncertainty. This was different from similar testing performed with the single radiosonde measurements used in Section 6.2 and 6.3. Occultation measurements are assumed to be a spatial average of the atmosphere over which the measurement is taken (nominally a horizontal scale of several thousand kilometres), but for a very limited time. For this reason occultation measurements were increasingly de-weighted in the adjustment over time without a maximum threshold imposed, so that over a large amount of time the occultations gradually cease to contribute information to the tomographic adjustment. Figure 6.47 shows the results with the eight-layer occultation measurement being assimilated into the adjustment while aging the sigma (measurement uncertainty) over the test.

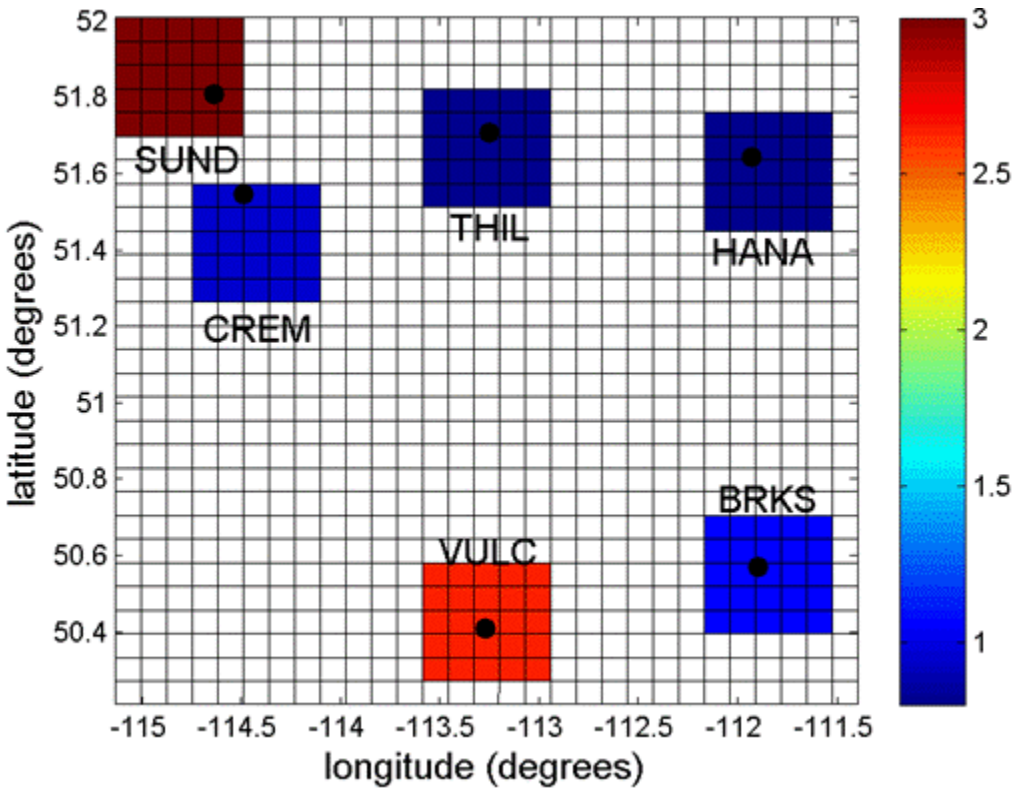

Figure 6.47. RMS (cm) of ZWD accuracies over two-hour interval with an eight-layer occultation measurement assimilated, with aging uncertainty applied.

In this case only Cremona shows a better RMS value over the test period, and Brooks and Vulcan have larger RMS values when compared to the case with no occultation measurement assimilated (Figure 6.45). The case with only the top three layers of the occultation measurement assimilated is shown in Figure 6.48.

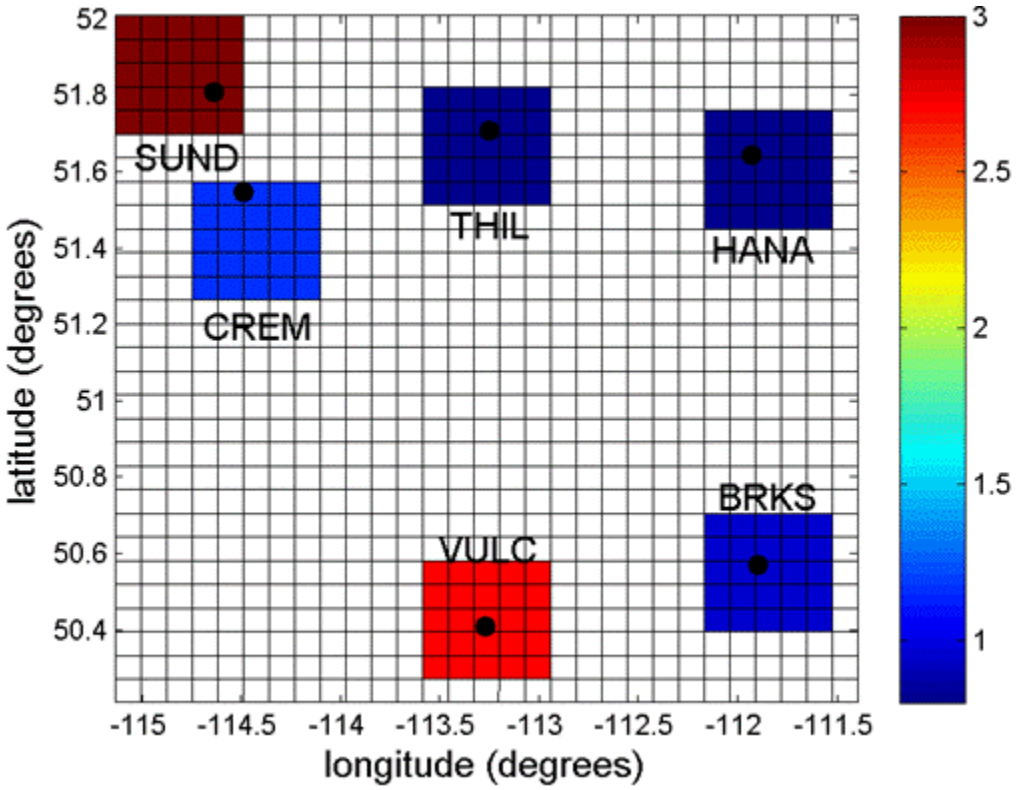

Figure 6.48. RMS (cm) of ZWD accuracies over two-hour interval with a three-layer occultation measurement assimilated, with aging applied.

Similar to the case where measurement uncertainty was not aged over time, Vulcan is the only station that has an improved RMS value with the aged, three-layer occultation measurement uncertainty being added.

6.6.4 Results from Eight-Hour Test Interval With Measurement Uncertainties Not Aged

The occultation measurements were also assimilated over an eight-hour interval, in a manner similar to results of Section 6.6.2, with the same measurement uncertainty being held fixed over the test period. The solution without occultation measurement assimilation is shown in Figure 6.49, for comparison purposes (as a default case).

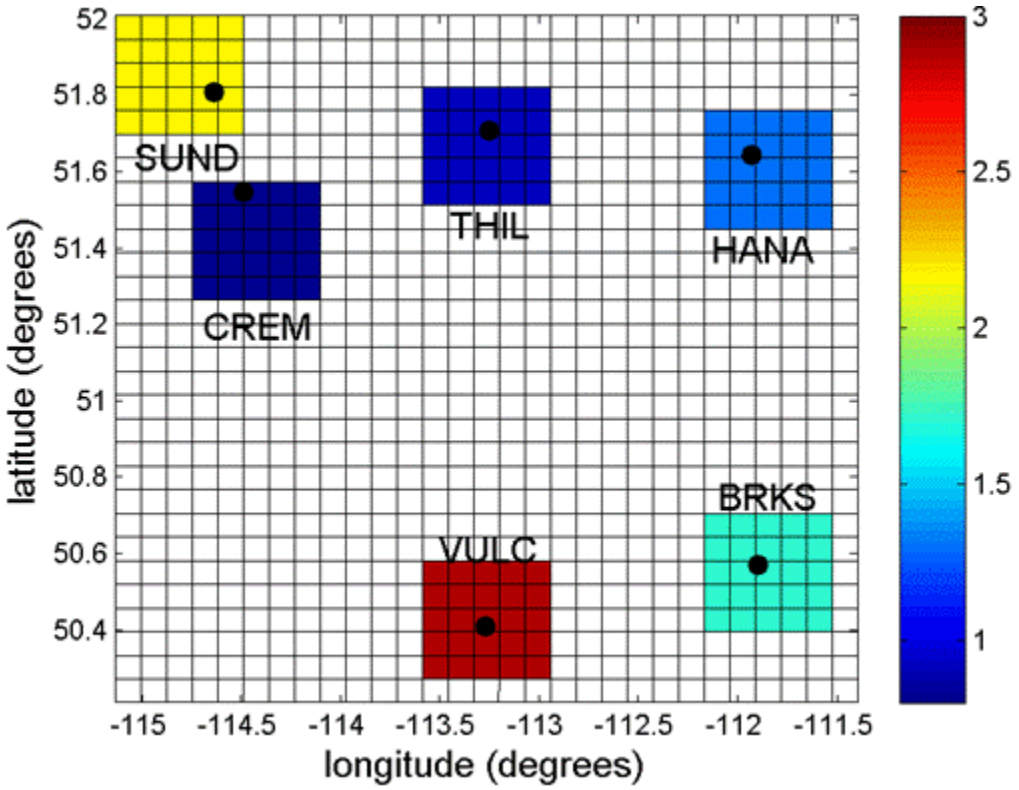

Figure 6.49. RMS (cm) of ZWD accuracies over eight-hour interval without occultation measurements assimilated.

RMS values indicate agreements better than 2 cm at Cremona, Three Hills, Hanna and Brooks. Results for the eight-layer occultation measurement assimilated into the tomography adjustment are shown in Figure 6.50.

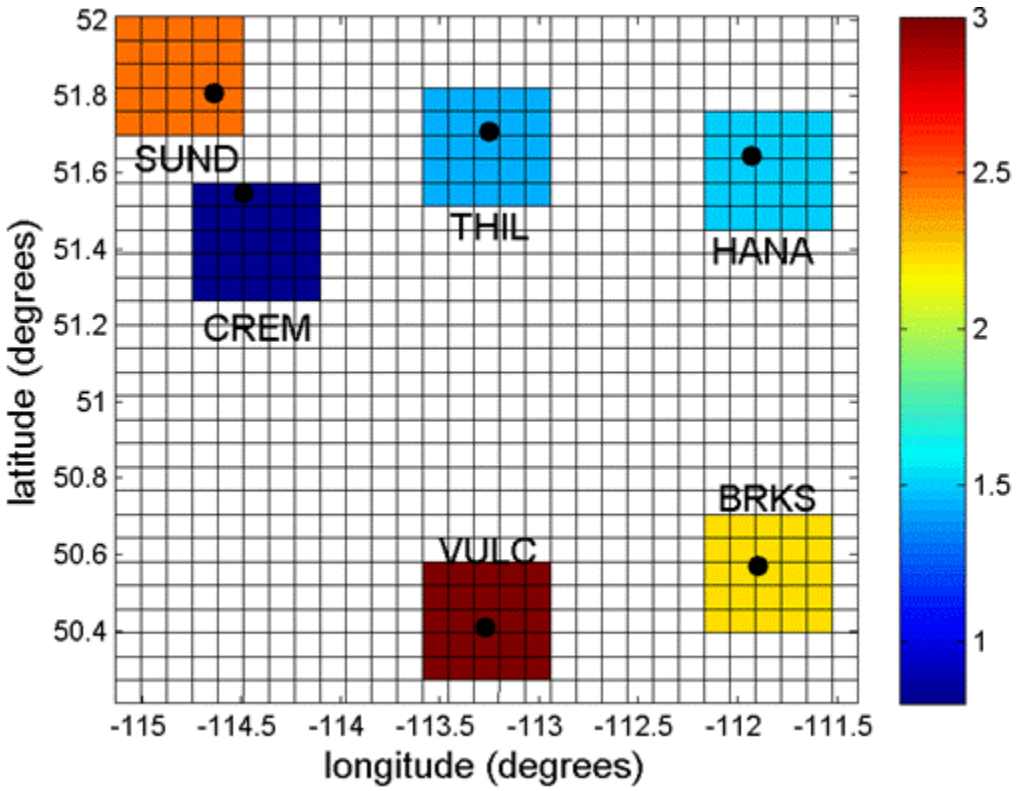

Figure 6.50. RMS (cm) of ZWD accuracies over eight-hour interval with an eight-layer occultation measurement assimilated.

When compared to the case without occultation measurements assimilated (Figure 6.49), all stations but Cremona have larger RMS values for the eight-layer occultation measurement assimilated. Results at Cremona appear to be of the same level of accuracy as the default case (no occultation measurement assimilated). These results indicate that an eight-hour interval is too long of an interval to assume that the eight-layer occultation measurement is valid. Results for the three-layer occultation measurement were also derived, and compared with the default case (where no occultation measurement was included) for an eight-hour interval. Results are shown in Figure 6.51.

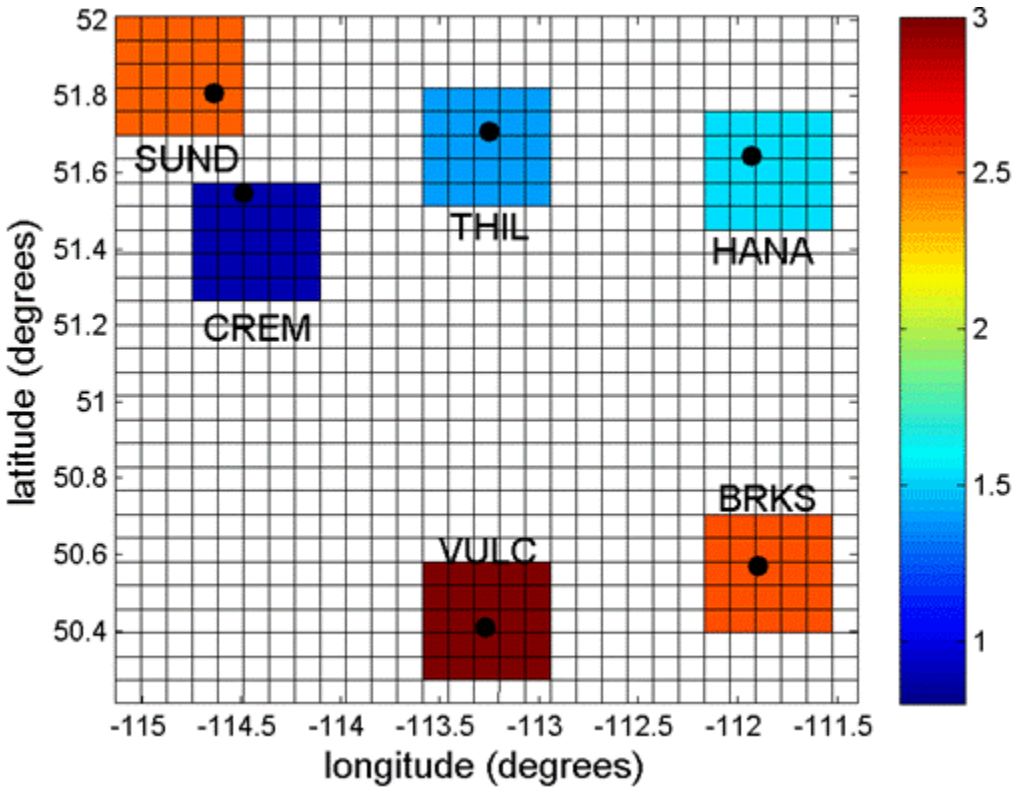

Figure 6.51. RMS (cm) of ZWD accuracies over eight-hour interval with a three-layer occultation measurement assimilated.

The only change in Figure 6.51 from results for the eight-layer occultation measurement assimilated is that Brooks RMS values are larger. The three-layer occultation observation does not do as well over eight hours as it did over two.

6.6.5 Results from Eight-Hour Test Interval With Measurement Uncertainty Aged

To determine if aging the measurement accuracy with time would allow the occultation measurement to make a positive impact over the default case (no occultation measurement assimilated), tests were conducted in the same manner as in Section 6.6.2, but for an eight-hour interval. The results for using an eight-layer occultation are given in Figure 6.52.

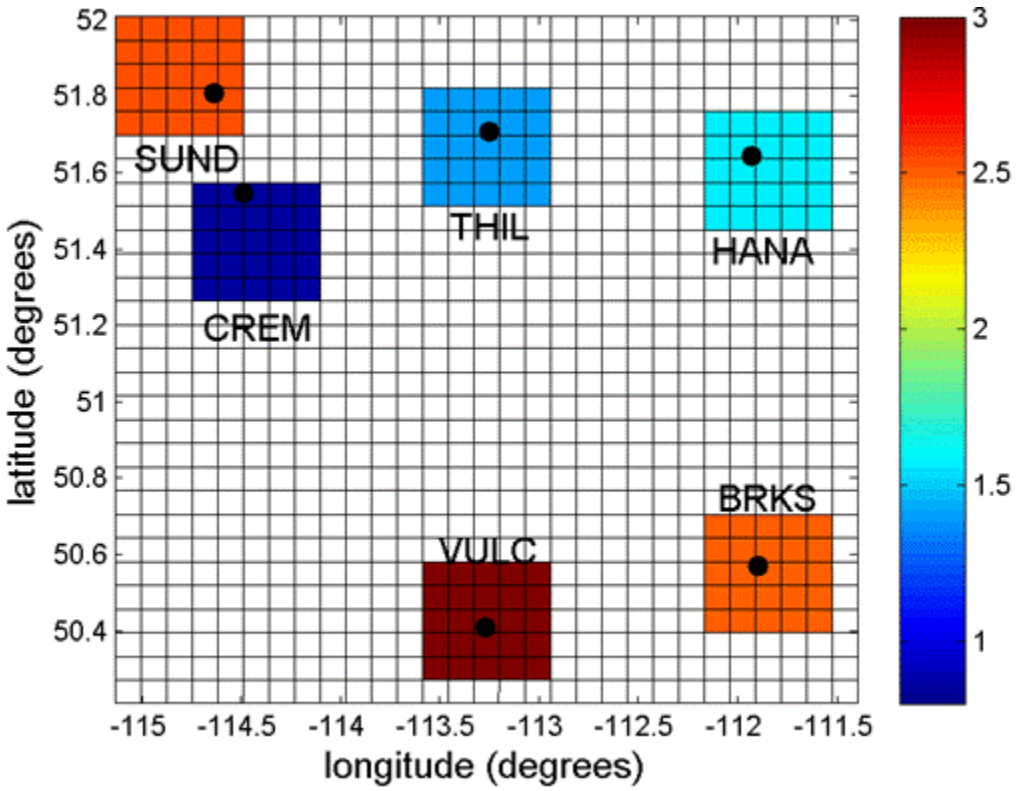

Figure 6.52. RMS (cm) of ZWD accuracies over eight-hour interval with an eight-layer occultation measurement assimilated, with aging uncertainty applied.

RMS values at Brooks are slightly larger than was found for the case with no occultation measurement assimilated. The results for a three-layer occultation observation assimilated are shown in Figure 6.53.

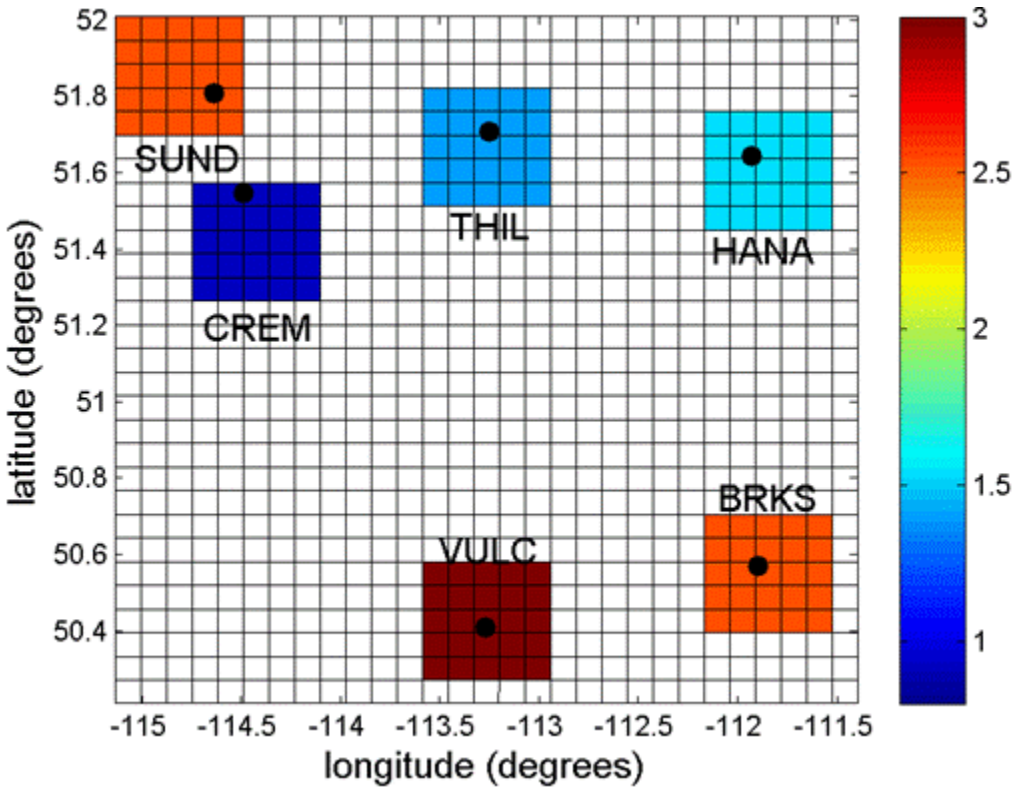

Figure 6.53. RMS (cm) of ZWD accuracies over eight-hour interval with a three-layer occultation measurement assimilated and aging applied.

Figure 6.53 shows exactly the same results as derived for the assimilation of the eight-layer occultation measurement (Figure 6.52). Any occultation measurement applied over eight hours with an aging uncertainty factor is not better than the tomography solution without the occultation included.

6.6.6 Summary of Results

A summary of results for all tests conducted assimilating occultation observations into the tomography model is given in Table 6.8.

Table 6.8 Zenith Wet Delay Accuracies for Occultation Assimilation

RMS (cm)				
Test	**Station**	**Without**	**8-Layer**	**3-Layer**
2 hour	BRKS	2.8	2.5	2.7
	CREM	0.7	0.7	0.8
	HANA	3.0	3.1	3.0
	SUND	0.5	0.5	0.6
	THIL	1.2	0.7	1.2
	VULC	0.9	1.2	1.0
Test	**Station**	**Without**	**8-Layer**	**3-Layer**
2 hour, with aging	BRKS	2.8	2.6	2.7
	CREM	0.7	0.8	0.8
	HANA	3.0	3.1	3.0
	SUND	0.5	0.6	0.6
	THIL	1.2	0.9	1.2
	VULC	0.9	1.1	1.0
Test	**Station**	**Without**	**8-Layer**	**3-Layer**
8 hour	BRKS	2.9	3.4	3.5
	CREM	0.9	1.4	1.4
	HANA	2.2	2.5	2.5
	SUND	1.3	1.5	1.5
	THIL	0.8	0.7	0.9
	VULC	1.7	2.2	2.5
Test	**Station**	**Without**	**8-Layer**	**3-Layer**
8 hour, with aging	BRKS	2.9	3.5	3.5
	CREM	0.9	1.4	1.4
	HANA	2.2	2.5	2.5
	SUND	1.3	1.6	1.5
	THIL	0.8	0.9	0.9
	VULC	1.7	2.5	2.5

The results are best for most stations when the occultation measurements are assimilated for a two-hour interval, without aging the measurement uncertainty. Stations that show the best improvement with occultations assimilated for this case are Brooks, which shows an improvement of 0.2 cm over the default case (no occultations assimilated), and Three

Hills, which shows an improvement of 0.5 cm. These improvements are significant for Three Hills, but are not significant for Brooks when compared to the level of improvement found from assimilating radiosonde measurements as per Section 6.2.

In every case, the solutions with occultations assimilated cause degraded accuracy of ZWD estimates at Vulcan, versus the case without occultations assimilated. This could be due to the fact that removing Vulcan GPS observations of ZWD from the solution (to use it as an independent test site) weakens the tomographic solution - due to low observability in the southeast corner of the network on this day; there are only two stations observing in this area (Vulcan and Brooks).

CHAPTER 7

CONCLUSIONS AND RECOMMENDATIONS

7.1 Conclusions

The Global Positioning System (GPS) consists of 27 satellites orbiting the earth at approximately 20 000 km altitude. The system is useable in all-weather, does not require calibration, can operate at a high data rate and allows for continuous measurements provided lines of sight are available to satellites. Ground-based receivers collect ranging information from satellites' RF signals, and derive a position. One source of error in the signal received is due to the delay caused by propagation through the troposphere. This error is due to water vapour, and other gases, and can be separated into hydrostatic and wet components. If a receiver's coordinates are known and surface pressure measurements are available, the positioning problem can be inverted such that the wet delay in the signal can be used to derive water vapour content in the atmosphere.

Traditional methods used to determine water vapour profiles have some limitations. Radiosondes provide good spatial resolution, but are expensive, and are only launched twice daily. Water vapour radiometers (WVR) have been used successfully to derive water vapour structure in the past, but are expensive. Characteristics of GPS make it advantageous for deriving three-dimensional spatial distribution, and the temporal variation of atmospheric water vapour for many environmental applications, such as meteorology, hydrology and climate monitoring.

Total zenith delays can be estimated for a GPS network of receivers using Bernese V 4.2. The hydrostatic zenith delay component of these total delays can be removed using Saastamoinen's hydrostatic delay model, which is accurate to the millimetre level. The remaining zenith wet delay can then be mapped down to its respective elevation angle by

the Niell wet mapping function. SWD retrieval has been shown in previous work to be accurate to 1-2 cm [*Shrestha*, 2003]. SWD can be used as input into a simple tomographic model, which uses an inversion technique to transform integrated measurements of SWD into the three-dimensional structure of water vapour over an area where GPS network measurements have been made. Resolving vertical structures of water vapour using data from a flat GPS network alone, using a tomography approach, results in poor vertical resolution of wet refractivity, although integrated quantities are accurate to approximately 1-2 cm. Through the use of other available sources of vertical profile information, improvements may be made in tomographic modeling of wet refractivity. Sources of vertical profile information include radiosonde data, climate models, microwave profilers, and radio occultation estimates. In this thesis, the impact of assimilating local radiosonde observations, monthly-averaged climate data and occultation-derived wet refractivity measurements into the tomography model was investigated.

The Southern Alberta Network (SAN) consists of 16 GPS receivers deployed in the Calgary region in Spring/Summer 2003. A data collection campaign called "A-GAME 2003" took place during the summer of 2003 during which radiosonde measurements were taken by the Meteorological Service of Canada within the SAN. Single radiosonde measurements taken at Airdrie, Alberta were assimilated into a tomographic adjustment performed with the GPS data from the SAN on four days ("GPS + RS"). Climatological data were also assimilated, which was derived from monthly radiosonde measurements from the MSC permanent radiosonde site for the Province of Alberta located at Stony Plain ("GPS + AveRS"). Both of the tomographic solutions formed from the assimilation of radiosonde measurements, and solutions formed from "GPS" only input were compared to a truth radiosonde at Olds/Didsbury airport. A summary of the results obtained with the assimilation of radiosondes and the GPS only solution is given in Table 7.1 below.

Table 7.1 Zenith Wet Delay Accuracies from Tomography Model during Times when Radiosonde Observations are Available (Storm Days in Shaded Cells)

Date	GPS	GPS + RS	GPS + AveRS
	RMS (cm)		
July 19	0.9	0.3	0.9
July 25	1.7	1.1	1.8
July 20	1.6	1.0	1.6
July 26	2.6	0.7	2.6

If monthly averaged radiosonde observations (climatological models) are derived for a station outside the SAN and assimilated into the tomographic solution, vertical profiles of wet refractivity are improved, especially at the upper altitudes due to the high uncertainty for this sort of a measurement in the lowest layer of the model. However, integrated ZWD quantities do not vary significantly from the GPS-only solution. The lack of improvement in ZWD values arises from the non-uniqueness of 4-D profiles generated by the tomography model: i.e., two different profiles can give a similar integrated solution. Since the lower atmospheric layers cannot be constrained with better certainty in this situation, the impact of assimilating climate data into the tomography model is minimal unless the vertical profile of water vapour is known more accurately. Vertical profiles retrieved with the GPS + AveRS solution were far better and more physically realistic than what was found with GPS alone; GPS alone can sometimes cause the retrieved profiles to be physically unrealistic due to the geometry of the observing GPS stations.

The addition of radiosonde point measurements from a location within the GPS network (GPS + RS) to ground-based GPS tomography improves the integrated ZWD solution by at least 0.5 cm when compared to the GPS-only tomographic solution, and improves the vertical wet refractivity profiles derived from the tomography model. Absolute ZWD accuracies, when compared to truth values, are in the range 0.3-1.1 cm for both quiet and storm days.

There are no significant differences in the results obtained for the July 20, 2003 storm day versus the quiet days, showing that the tomographic solutions obtained are likely not influenced by higher levels of atmospheric dynamics, or at least the dynamics associated with storms that occurred on July 20, 2003 in southern Alberta. July 26, 2003 showed the highest errors for the tests performed, but it is not clear if this is due to the storm dynamics on this day, or the fact that this day had the least number of ground-based stations for processing; July 26, 2003 had five stations of data whereas other days processed had six or seven.

In results discussed above, the radiosonde point observations (i.e. RS observations) are only assumed valid for a one-hour interval following launch. Tests were conducted in which the radiosonde observations were assumed to be valid for an eight-hour period. An approach was also implemented where rather than using the same uncertainty (error estimates for the radiosonde data) for the entire time span of interest, the radiosonde data carried less weight in the tomography solution over time. With this approach, the hope was that the weight on the radiosonde observations would allow the solution to be more representative of the true atmospheric conditions, since it was not constraining to a radiosonde which was taken at a specific time. A summary of the results from the long-term testing is shown in Table 7.2.

Table 7.2 Zenith Wet Delay Accuracies from Tomography Model for 8-Hour Testing (Storm Days Are Shaded)

Date	GPS	GPS + RS	GPS + AveRS
	RMS (cm)		
July 19, Long	1.4	1.0	1.2
July 19, Long & Aged	1.4	1.1	1.2
July 20, Long	1.8	1.0	1.7
July 20, Long & Aged	1.8	1.5	1.7
July 25, Long	1.3	0.9	1.3
July 25, Long & Aged	1.3	1.1	1.3
July 26, Long	2.2	0.7	2.3
July 26, Long & Aged	2.2	1.6	2.3

The “long” case for GPS + RS solution is

- worsened for July 19,
- stays the same for July 20,
- is made better for July 25 and
- stays the same for July 26

when compared to values in Table 7.1. There is no clear advantage or disadvantage to assimilating an RS measurement over eight hours versus one. This is probably due to the fact that in order for an RS measurement to improve vertical accuracy in the tomographic solution over a longer period of time, the RS measurement has to represent the atmosphere over most of the testing time. If the RS measurement is taken at a time when this is true, then it will help the adjustment, but if atmospheric conditions are such that the RS measurement is only representative for a short period of time, it is not advantageous to include it over a long period of time. It was hypothesized before this test was performed that keeping the RS measurement in the adjustment for a long time period would make the accuracy worse when compared to one-hour testing on storm days particularly, due to increased dynamics of water vapour on these days. However, this was not seen in these tests, indicating that there is enough dynamics on quiet days to affect the time over which the RS measurement should be deemed representative of the atmosphere.

In every case presented in Table 7.2, aging the RS measurement accuracy worsens the solution by anywhere from 0.1 – 0.9 cm. As it turns out for the case studied on July 26, 2003 over eight hours of processing, the accuracy degrades by aging the radiosonde measurement, and the difference from truth radiosonde measurements increases by 0.3 cm as compared to keeping the weight constant over the entire estimation period.

A sensitivity analysis was performed to determine the sensitivity of the adjustment to changes in the accuracies of the RS measurements of temperature and relative humidity. Temperature measurements were given degraded accuracies from 0.1 to 20 ºC/ºK, and relative humidity accuracy was degraded from 1 to 3 %. A summary of these results is presented in Table 7.3.

Table 7.3 Zenith Wet Delay Accuracies (GPS + RS only) from Tomography Model during Times when Radiosonde Observations are Available on July 19, 2003 for Sensitivity Analysis (Default Settings Shaded)

Case	Temp Meas. Accuracy (°C/°K)	RH Meas. Accuracy (%)	RMS (cm)
1	0.1	1	0.3
2	0.2	1	0.3
3	1	1	0.3
4	10	1	0.4
5	20	1	0.7
6	0.1	1.5	0.4
7	0.1	3	0.7

Degrading accuracies in temperature and relative humidity had the largest impact on the solutions for the lowest layers in the adjustment. These are the layers that in general see the highest temperatures and amounts of water vapour. It was found that the temperature had to have a large increase in measurement error to have a significant impact on the accuracy on the tomographic adjustment, but that relative humidity only needed slight increases in uncertainty to affect the adjustment significantly.

The climate data (i.e. the AveRS measurement) assimilated into the tomography model was given high measurement accuracy in order to determine if it was beneficial to tighten the constraint that this measurement put on the modelling (differing from the accuracy indicated by the monthly variation of this measurement). A typical magnitude of measurement accuracy derived for a RS observation was applied to the AveRS

measurement and tested over four test times. A summary of results for this testing is given in Table 7.4.

Table 7.4 Zenith Wet Delay Accuracies from Tomography Model over Increased Climate Model Measurement Accuracy Testing

Date	Original GPS + AveRS	GPS + AveRS
	RMS (cm)	
July 19	0.9	0.4
July 20	1.6	1.4
July 25	1.8	2.6
July 26	2.6	3.0

July 19 and 20 show improvement with the AveRS measurement weighted more heavily, and July 25 and 26 show a degradation in accuracy when the AveRS measurement is weighted more heavily in the tomographic adjustment. Once the AveRS integrated solution was plotted along with the other integrated solutions for these test times, it became evident that if the truth solution was in between the original GPS + AveRS solution and the AveRS solution, the heavier weighting on the AveRS solution would pull the GPS + AveRS solution towards the truth, thereby making the integrated solution accuracy better. However, for the case where the original GPS + AveRS solution was in between the truth and AveRS integrated solutions, the GPS + AveRS solution with the AveRS measurement more heavily weighted would become worse when compared to the truth solution. The danger in weighting a monthly profile heavily is that sometimes it may represent the atmosphere, but because it is an average, there will be periods of time where it doesn't.

Water vapour profiles can also be derived from radio occultations using low Earth orbiting (LEO) satellites. Since occultation data is likely to become more readily accessible and timely in the future, these measurements could be assimilated into the tomographic estimation routine. Occultations were assimilated and treated as an average

measurement across the SAN while doing so. This is because when the occultation measurements are made, they are from a signal that is traversing hundreds of kilometres of the atmosphere. Accuracies were found from removing one SAN station at a time from the adjustment, and comparing ZWD at each station from Bernese V 4.2 processing to model output with and without occultations assimilated. Occultations were assimilated for all eight layers of the model and then for the top three, which are considered to be most accurate. Two-hour test times and eight-hour test times were utilized, and aging the occultation measurement variance was tested as well. Results are summarized in Table 7.5.

Table 7.5 Zenith Wet Delay Accuracies for Occultation Assimilation

RMS (cm)				
Test	**Station**	**Without**	**8-Layer**	**3-Layer**
2 hour	BRKS	2.8	2.5	2.7
	CREM	0.7	0.7	0.8
	HANA	3.0	3.1	3.0
	SUND	0.5	0.5	0.6
	THIL	1.2	0.7	1.2
	VULC	0.9	1.2	1.0
Test	**Station**	**Without**	**8-Layer**	**3-Layer**
2 hour, with aging	BRKS	2.8	2.6	2.7
	CREM	0.7	0.8	0.8
	HANA	3.0	3.1	3.0
	SUND	0.5	0.6	0.6
	THIL	1.2	0.9	1.2
	VULC	0.9	1.1	1.0
Test	**Station**	**Without**	**8-Layer**	**3-Layer**
8 hour	BRKS	2.9	3.4	3.5
	CREM	0.9	1.4	1.4
	HANA	2.2	2.5	2.5
	SUND	1.3	1.5	1.5
	THIL	0.8	0.7	0.9
	VULC	1.7	2.2	2.5
Test	**Station**	**Without**	**8-Layer**	**3-Layer**
8 hour, with aging	BRKS	2.9	3.5	3.5
	CREM	0.9	1.4	1.4
	HANA	2.2	2.5	2.5
	SUND	1.3	1.6	1.5
	THIL	0.8	0.9	0.9
	VULC	1.7	2.5	2.5

The results are best for most stations when the eight-layer occultation measurements are assimilated for two hours, without aging the measurement accuracy. There are no significant differences in the results from the assimilation of eight or three layers. Stations showing the most improvement with occultations assimilated (during the best

run) are Brooks, which shows an improvement of 0.2 cm and Three Hills which shows an improvement of 0.5 cm.

In every case, the solutions with occultations assimilated worsen the solution at Vulcan versus the case without occultations assimilated. This could be due to the fact that removing Vulcan from the solution to compare it to the Bernese V 4.2 solution at this station weakens the tomographic solution due to low observability in the southeast corner of the network on this day; there are only two stations observing in this area (Vulcan and Brooks).

7.2 Recommendations for Future Work

If future work is to be done with the assimilation of radiosonde measurements, then it would be valuable to have the input radiosonde be a bit further from the truth comparison location; as it stands, they were ~50 km apart for these tests, but there were no other radiosonde observations available in the SAN. When radiosonde observations were being taken in the SAN during A-GAME 2003, cost was a factor in the launch timing, and site launches were purposely staggered to get the best temporal coverage. If cost were not a factor in the future it would be beneficial to release radiosondes from a truth location more often so that solutions formed with radiosonde observations assimilated could be compared to a truth which is relatively current.

Occultation data should be represented in the tomographic adjustment in a different way than that done here. Some investigation into the horizontal path lengths of the signal during the occultation could give additional information on the occultation which could help in its spatial representation during the estimation. *Aparicio and Deblonde* [2004] suggest that assimilating the bending angle could be more beneficial than assimilating refractivity profiles into a forecast model for weather prediction. The use of bending

angles versus refractivity profiles could be investigated in future work for accuracy differences.

The GEM model that was used to assimilate the occultation observations itself has errors associated with it, which were hard to quantify since the GEM was run for a specific region and time. If the GEM is used in the future to assimilate occultation measurements, then having accuracy measures for the run of GEM would ensure that these errors are characterized in the tomographic adjustment accordingly.

REFERENCES

Aguado, E. and J.E. Burt, *Understanding Weather & Climate*, Pearson Education Inc., Upper Saddle river, NJ, U.S.A., third edition, 2004.

Alves, P., Y.W. Ahn, J. Liu, G. Lachapelle, D. Wolfe and A. Cleveland, Improvements of USCG RTK positioning performance using external NOAA tropospheric corrections integrated with a multiple reference station approach, *Proceedings of the Institute of Navigation's National Technical Meeting*, 689, January, 2004.

Andrews, D.G., *An Introduction to Atmospheric Physics*, Cambridge University Press, Cambridge, UK, 2000.

Aparicio, J.M. and G. Deblonde, Assessment of Impact of the Assimilation of GPS Radio Occultation Observations, Proceedings of The Institute of Navigation's GNSS 2004, Long Beach, CA, Sept 21-24, in press, 2004.

Bar-Sever, Y.E. and P. M. Kroger, Estimating horizontal gradients of tropospheric path delay with a single GPS receiver, *Journal of Geophysical Research*, **103**, B3, 5019, 1998.

Bevington, P.R. and D.K. Robinson, *Data Reduction and Error Analysis for the Physical Sciences*, WCB/McGraw Hill Press, Boston, Massachusetts, U.S.A., 1992.

Bevis, M., S. Businger, T.A. Herring, C., Rocken, R.A. Anthes and R.H. Ware, GPS meteorology: remote sensing of atmospheric water vapor using the global positioning system, *Journal of Geophysical Research*, **97**, D14, 15787, 1992.

Braun, J.J. and C. Rocken, Water vapor tomography within the planetary boundary layer using GPS, *Proceedings of the International Workshop on GPS Meteorology, GPS Meteorology: Ground-Based and Space-Borne Applications*, Tsukuba, Japan, http://dbx.cr.chiba-u.jp/Gps_Met/gpsmet, January 14-17, 2003.

Brunner, F.K. and M. Gu, An improved model for the dual frequency ionospheric correction of GPS observations, *Manuscripta Geodaetica*, **16**, 205, 1991.

Businger, S., S.R. Chiswell, M. Bevis, J.Duan, R. Anthes, C. Rocken, R. Ware, M. Exner, T. VanHove, F. Solheim, The promise of GPS in atmospheric monitoring, *Bull. Amer. Met. Soc.*, **77**, 5, 1996.

Bust, G.S., T.W. Garner, T.L. Gaussiran II, Ionospheric data assimilation three dimensional (IDA3D): a new global, multi-sensor, three dimensional electron density specification algorithm, *Journal of Geophysical Research*, 2004, in press.

Cannon, M.E., "ENGO 561 Satellite Positioning", Winter term vu-graphs, Geomatics Engineering Department, University of Calgary, 2001.

Côté, J., S. Bélair, P. Vaillancourt, A. Erfani and U. Gramann, The Canadian global environmental multiscale model: development and applications, *Japan Meteorological Agency NWP Research and Development Platform Web Site*, http://pfi.kishou.go.jp/open/ ws0302/abstract/cote/cote_a4_bw.pdf, Accessed: November 2004.

El-Sheimy, N., "ENGO 361 Introduction to Least Squares", course notes, Spring, 2004.

Enge, P., Retooling the global positioning system, *Scientific American*, 90, May, 2004.

Fjeldbo, G., A.J. Kilore and V.R. Eshleman, The neutral atmosphere of Venus as studied with the Mariner V radio occultation experiments, *The Astronomical Journal*, **76**, no. 2, March, 1971.

Flores, A, G. Ruffini and A. Ruis, 4D Tropospheric tomography using GPS slant wet delays, *Ann. Geophysicae,* **18**, 223, 2000.

Fortes, L.P., personal communication, January 2004.

Gelb, A., *Applied Optimal Estimation*, M.I.T. Press, Massachusetts, U.S.A., 1974.

Gregorius, T. and G. Blewitt, The effect of weather fronts on GPS measurements, *GPS World*, May, 1998.

Jerrett, D. and J. Nash, Potential uses of surface based GPS water vapour measurements for meteorological purposes, *Phys. Chem. Earth (A)*, **26**, no. 6-8, 457, 2001.

Kalnay, E. *Atmospheric Modeling, Data Assimilation and Predictability*, Cambridge University Pres, Cambridge, United Kingdom, 2003.

Kaplan, E.D., *Understanding GPS Principles and Applications*, Artec House, Norwood, Massachusetts, 1996.

Krauss, T.W. and J.R. Santos, The effect of hail suppression operations on precipitation in Alberta, Canada, *Proceedings: 8th WMO Scientific Conference on Weather Modification*, Casablanca, Morocco, April 7-12, 2003.

Kuo, Y.-H., T.-K. Wee, S. Sokolovskiy, C. Rocken, W. Schreiner, D. Hunt and R.A. Anthes, Inverstion and error estimation of GPS radio occultation data, *Journal of the Meteorological Society of Japan*, **82**, no. 1B, 507, 2004.

Healy, S., personal communication, July 2004.

Hofmann-Wellenhof, B., H. Lichtenegger and J. Collins, *GPS Theory and Practice*, Springer-Verlag Wien, NewYork, NY, USA, fourth edition, 1997.

Hopfield, H.S., Two-quartic tropospheric refractivity profile for correction satellite data, *Journal of Geophysical Research*, **74**, no. 18, 4487, 1969.

Hoyle, V.A., *Tracking Severe Weather Using GPS-Derived Estimates of Precipitable Water Vapour*, ENGG 683 Summer 2003 Special Projects Course Report, 2003.

Hugentobler, U., S. Schaer and P. Fridez, *Bernese GPS Softare Version 4.2*, user manual, Astonomical Institute, University of Berne, Switzerland, February, 2001.

Institute of Information and Computing Science (ICS) Web Site, Temp, Humidity & Dew-Point ONA, http://www.cs.uu.nl/wais/html/na-dir/meteorology/temp-dewpoint.html, Accessed: August 10, 2004.

International GPS Service (IGS) Website, http://igscb.jpl.nasa.gov/index.html, Accessed: 2002-2004.

Jacob, D., The role of water vapour in the atmosphere. A short overview from a climate modeller's point of view, *Phys. Chem. Earth (A)*, **26**, no 6-8, 523, 2001.

Lachapelle, G., "ENGO 625 NAVSTAR GPS: Theory and Applications", Fall term vu-graphs, Geomatics Engineering Department, University of Calgary, 2002.

Langen, D. and L.P. Fortes, *Bernese GPS Software Version 4.2 Processing Guide*, Department of Geomatics Engineering internal document, June, 2002.

Langley, R.B., GPS receiver system noise, *GPS World*, **8**, no. 6, 40, 1997.

Liou, Y. and C. Huang, GPS observations of PW during the passage of a typhoon, *Earth Planets Space*, **52**, 709, 2000.

MacDonald, A.E., Y. Xie and R.H. Ware, Diagnosis of three-dimensional water vapor using a GPS network, *Monthly Weather Review*, **130**, 386, February, 2002.

McCarthy, J.J., O.F. Canziani, N.A. Leary, D.J. Dokken, and K.S. White, *Climate Change 2001: Impacts, Adaptation and Vulnerability*, Contribution of Working Group II to the Third Assessment Report of the Intergovernmental Panel on Climate Change, Cambridge University Press, Cambridge, UK, 2001.

Mendes, V.B., *Modeling the neutral-atmosphere propagation delay in radiometric space techniques*, Ph.D. Dissertation, University of New Brunswick, Fredericton, Canada, 1999.

Nash, J., *Introduction to performance of modern radiosondes based on WMO radiosonde comparison results, temperature*, PowerPoint presentation, World Meteorological Organization Commission for Instruments and Methods of Observation Joint Meeting, Geneva, Switzerland, http://www.wmo.ch/web/www/IMOP/meetings/Upper-Air/Systems-Intercomp/DocPlan.html, March 17-20, 2004a.

Nash, J., *Review of WMO test results on the accuracy of radiosonde relative humidity sensors*, PowerPoint presentation, World Meteorological Organization Commission for Instruments and Methods of Observation Joint Meeting, Geneva, Switzerland, http://www.wmo.ch/web/www/IMOP/meetings/Upper-Air/Systems-Intercomp/DocPlan.html, March 17-20, 2004b.

National Climate Data and Information Archive, Environment Canada Web Site, http://www.climate.weatheroffice.ec.gc.ca/Welcome_e.html, Accessed: November 2004.

Nicholson, N., V. Hoyle, S. Skone, M.E. Cannon and G. Lachapelle, 4-D troposphere modeling using a regional GPS network in southern Alberta, *Proceedings of the Institute of Navigation GNSS 2003*, Portland, OR, USA, 1718, September 9-12, 2003.

Niell, A.E., Global mapping functions for the atmosphere delay at radio wavelengths, *Journal of Geophycical Research*, **101**, no. B2, 3227, 1996.

Niell, A.E., A.J. Coster, F.S. Solheim, V.B. Mendes, P.C. Toor, R.B. Langley and C.A. Upham, Comparison of measurements of atmospheric wet delay by radiosonde, water vapor radiometer, GPS, and VLBI, *Journal of Atmospheric and Oceanic Technology*, **18**, 830, June, 2001.

NovAtel Website, http://www.novatel.ca, Accessed: August 2003.

Parkinson, B.W. and J.J. Spilker, *Global Positioning System: Theory and Applications Volume I,* American Institute of Aeronautics and Astronautics, Washington, D.C., 1996.

Paroscientific Web Site, MET3A Spec Sheet, http://www.paroscientific.com/met3a.htm, Accessed: November 2004.

Portland State Aerospace Society (PSAS) Web Site, http://psas.pdx.edu/RocketScience/PressureAltitude_Derived.pdf, Accessed: October 2004.

Reigber, C., G. Gendt, G. Dick and Maria Tomassini, Near-real-time water vapor monitoring for weather forecasts, *GPS World*, 18, January, 2002.

Rocken, C., T. Van Hove, and R. Ware, Near real-time GPS sensing of atmospheric water vapor, *Geophysical Research Letters,* **24**, no.24, 3221, 1997.

Rocken, C., J. Braun, T. Van Hove and R. Ware, GPS networks for atmospheric sensing, *Proceedings of the Institute of Navigation's National Technical Meeting*, 439, January, 2000.

Saastamoinen, J., Atmospheric correction for the troposphere and stratosphere in radio ranging of satellites, *Geophysical monograph*, American Geophysical Union, **15**, 247, 1972.

Shrestha, S. M., *Investigations into the Estimation of Tropospheric Delay and Wet Refractivity using GPS Measurements*, UCGE Reports Number 20180, M.Sc. Thesis, Department of Geomatics Engineering, University of Calgary, July, 2003.

Skone, S.H., "ENGO 633 Atmospheric Effects on Satellite Navigation Systems", Winter term course notes, Geomatics Engineering Department, University of Calgary, 2003.

Skone, S. and S. Shrestha, 4-D modeling of water vapour using a regional GPS network, *Proceedings of the Institute of Navigation's National Technical Meeting*, Anaheim, CA, USA, January, 2003.

Smith, C., personal e-mail communication, August 25, 2004a.

Smith, C., personal e-mail communication, October 27, 2004b.

Smith, E.K. and S. Weintraub, The constants in the equation for atmospheric refractive index at radio frequencies, *Proceedings of I.R.E.*, **41**, 1035, August, 1953.

Smith, T.L., S.G. Benjamin, B.E. Schwarta and S.I. Gutman, using GPS-IPW in a 4-D data assimilation system, *Earth Planets Space*, **52**, 921, 2000.

Strong, G.S., personal e-mail communication, August 25, 2003.

Strong, G.S., personal E-mail communication, October 27, 2004.

Strong, G.S. and C.D. Smith, *Assessment and Prediction of Prairie Severe Thunderstorm Weather Phenomena*, a report prepared for Public Safety and Emergency Preparedness Canada, Ottawa, ON, Canada, 2001.

Torge, W., *Geodesy*, Walter de Fruyter, Berlin, Germany, second edition, 1991.

Vaisala Web Page, RS80 Spec Sheet, http://www.vaisala.com/DynaGen_Attachments/Att2743/2743.pdf, Accessed: August 13, 2004.

Van Dierendonck, A.J., P. Fenton and T. Ford, Theory and performance of narrow correlator spacing in a GPS receiver, *Navigation: The Journal of the Institute of Navigation*, **39**, no. 3, 283, Fall, 1992, http://www.novatel.ca/Documents/Papers/File2.pdf.

Ware, R., C. Alber, C. Rocken and F. Solheim, Sensing integrated water vapour along GPS ray paths, *Geophysical Research Letters*, **24**, 417. 1997.

Ware, R., D. Fulker, S.Stein, D. Anderson, S. Avery, R. Clark, K. Droegemeier, J. Kuettner, J. Minster and S. Sorooshian, SuomiNet: A real-time national GPS network for atmospheric research and education, *Bulletin of the American Meteorological Society*, **81**, 677, 2000.

Ware, R., personal e-mail communication, September 2004.

Wells, D., *Guide to GPS Positioning*, Canadian GPS Associates, Ottawa, ON, Canada, second printing, 1987.

Wickert, J., C. Reigber, G. Beyerle, G. Beyerle, R. König, C. Marquardt, T. Schmidt, L. Grunwaldt, R. Galas, T. Meehan, W. Melbourne, K. Hocke, Atmosphere sounding by GPS radio occultation: first results from CHAMP, *Geophysical Research Letters*, **28**, 3263, 2001a.

Wickert, J., R. Galas, G. Beyerle, R. König and C. Reigber, GPS ground station data for CHAMP radio occultation measurements, *Phys. Chem. Earth*, **26**, no. 6-8, A, 503, 2001b.

Wickert, J., T. Schmidt, G. Beyerle, R. König, C. Reigber and N. Jakowski, The radio occultation experiment aboard CHAMP: operational data analysis and validation of vertical atmospheric profiles, *Journal of the Meteorological Society of Japan*, **82**, no. 1B, 381, 2004.

Wolfe, D.E. and S.I. Gutman, Developing an operational, surface-based, GPS, water vapor observing system for NOAA: Network design and results, *Journal of Atmospheric and Oceanic Technology*, **17**, 426, April, 2000.

APPENDIX A: RELATIVE VERSUS ABSOLUTE DELAY IN NETWORK GPS WATER VAPOUR RETRIEVAL

If simultaneous measurements are made from two receivers to two satellites, then a double difference measurement can be made from these observations (numbered 1-4 in Figure A.1).

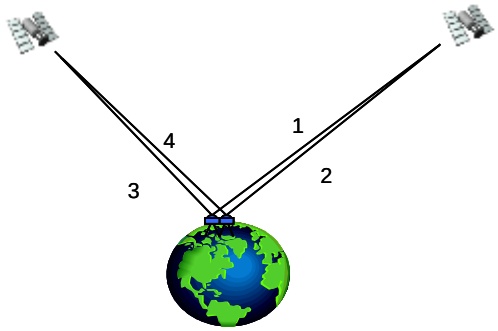

Figure A.1: Observations forming a single double difference measurement.

Observations 1-4 are denoted:

$$m_i ZD_i \tag{A.1}$$

where

m is the mapping function used to map down to the appropriate elevation angle

ZD is the zenith delay and

i denotes the observation number

and the full double difference (DD) observation equation is then

$$DD = m_1 ZD_1 - m_2 ZD_2 - (m_3 ZD_3 - m_4 ZD_4) \tag{A.2}$$

Since the receivers are viewing the satellites from essentially the same elevation angle because they are very close together,

$$m_1 \cong m_2 \cong m_3 \cong m_4 \tag{A.3}$$

In the least squares adjustment, the double difference observation will be broken down into

$$L = Ax \tag{A.4}$$

$$DD = [m_1 - m_2 \qquad - m_3 + m_4] \begin{bmatrix} ZD_1 \\ ZD_2 \\ ZD_3 \\ ZD_4 \end{bmatrix} \tag{A.5}$$

where

L is the observations

A is the design matrix

x is a matrix of the unknowns

If A.3 holds, then in A.5 there will be zeros in the design matrix which become a challenge when trying to invert it. In this situation, it is therefore then necessary to solve for relative difference so ZD between sites, i.e. ZD_1-ZD_2 and $-ZD_3$+ZD_4 in order to have a mathematically stable solution.

APPENDIX B: NIELL MAPPING FUNCTION LOOK-UP TABLES

The hydrostatic mapping function coefficients are found at latitude j_i at time t (UT days from January 0.0) from Table B.1 and the following expression (tables and equations are after *Shrestha* [2003])

$$a(j_i, t) = a_{avg}(j_i) + a_{amp}(j_i)\cos\left[2p\,\frac{t - T_0}{365.25}\right] \tag{B.1}$$

where

T_0 is the adopted phase, day of year (DOY) 28 as described by *Niell* [1996]

The 'a' coefficients are linearly interpolated from the values given in Table B.1 for the hydrostatic coefficients and Table B.2 is used if wet coefficients are desired. Similarly, 'b' and 'c' coefficients are found using the same procedure.

Table B.1 Neill Hydrostatic Mapping Function Coefficients

Hydrostatic Coefficient	Latitude (°)				
	15	**30**	**45**	**60**	**75**
	Average				
a_avg	1.2769934E-03	1.2683230E-03	1.2465397E-03	1.2196049E-03	1.2045996E-03
b_avg	2.9153695E-03	2.9152299E-03	2.9288445E-03	2.9022565E-03	2.9024912E-03
c_avg	6.2610505E-02	6.2837393E-02	6.3721774E-02	6.3824265E-02	6.4258455E-02
	Amplitude				
a_amp	0	1.2707963E-05	2.6523662E-05	3.4000452E-05	4.1202191E-05
b_amp	0	2.1414979E-05	3.0160779E-05	7.2562722E-05	1.1723375E-04
c_amp	0	9.0128400E-05	4.3497037E-05	8.4795348E-04	1.7037206E-03

Table B.2 Neill Wet Mapping Function Coefficients

Wet Coefficient	Latitude (º)				
	15	30	45	60	75
	Average				
a_avg	5.8021897E-04	5.6794847E-04	5.8118019E-04	5.9727542E-04	6.1641693E-04
b_avg	1.4275268E-03	1.5138625E-03	1.4572520E-03	1.5007418E-03	1.7599082E-03
c_avg	4.3472961E-02	4.6829510E-02	4.3908931E-02	4.4526982E-02	5.4736038E-02